UC Irvine
UC Irvine Electronic Theses and Dissertations

Title
Micron scale mechanical response of fibrin hydrogels

Permalink
https://escholarship.org/uc/item/4pm167g4

Author
Hu, Qingda

Publication Date
2022

Copyright Information
This work is made available under the terms of a Creative Commons Attribution License, availalbe at https://creativecommons.org/licenses/by/4.0/

Peer reviewed|Thesis/dissertation

eScholarship.org Powered by the California Digital Library
University of California

UNIVERSITY OF CALIFORNIA,
IRVINE

Micron scale mechanical response of fibrin hydrogels

DISSERTATION

submitted in partial satisfaction of the requirements
for the degree of

DOCTOR OF PHILOSOPHY

in Mathematical, Computational, and Systems Biology

by

Qingda Hu

Dissertation Committee:
Professor Elliot Botvinick, Chair
Associate Professor Jun Allard
Assistant Professor Albert Siryaporn
Assistant Professor Timothy L. Downing

2022

© 2022 Qingda Hu

DEDICATION

To those who believed in me when I didn't believe in myself.

TABLE OF CONTENTS

LIST OF FIGURES

LIST OF TABLES

ACKNOWLEDGMENTS

I would like to thank Dr. Elliot Botvinick for everything. A mentor, when I needed help. A fan, when I needed to be encouraged. A critic, when I needed to be pushed. A friend, when life was hard. Nothing, when I needed time for myself. I aspire to be like you one day, to make the life of those around me better.

There are many people who helped make this possible. First, I need to thank my closest friends: Dr. Tessa Morris, Alvaro Fletcher, Dr. Alicja Jagiełło, Dr. Dat Nguyen, Dr. Yara Mohajerani. Second, I need to thank my mentors and collaborators: Dr. Jun Allard, Dr. Anna Grosberg, Dr. Alex Levine, Dr. Wolfgang Wall, Dr. Valentin Slepukhin, Dr. Maximilian Grill, Dr. Fred Wan, Dr. Arthur Lander, Dr. Qing Nie, Dr. Zeba Wunderlich, Dr. Steve Allison, Dr. Albert Siryaporn, Dr. Enrico Gratton. Third, I need to thank everyone who has helped me academically and helped me grow as a person: Dr. Mark Keating, Micah Lim, Dr. Rachel Gurlin, Dr. Todd Thorson, Luciano Groisman, Toni Wilkinson, Dr. Sorena Rahmanian, Dr. Joe Nash, Dr. Matt Bovyn, Dr. Kerrigan Blake, Dr. Dianne Mendoza, Herman Ching. Lastly, this is an incomplete list so I would like to thank everyone I forgot.

I wish the best to Sarah Eldeen and Michelle Lanterman on their journey in continuing this work. I wish the best to Aryan Agarwal and Ulysses Castillo in whatever they pursue in the future. I have no doubt that they will all excel at everything they set their sights on.

I acknowledge financial support from the United States Air Force Office of Scientific Research FA9550-17-1-0193 and the United States National Science Foundation (US-NSF) under Award Number DMS-1953410.

VITA

Qingda Hu

EDUCATION

Doctor of Philosophy, MCSB **2022**
University of California, Irvine *Irvine, California*

Masters of Science, LMP **2016**
University of Toronto *Toronto, Canada*

Bachelor of Science, specialist Pathobiology **2014**
University of Toronto *Toronto, Canada*

RESEARCH EXPERIENCE

Graduate Research Assistant **2017–2022**
University of California, Irvine *Irvine, California*

Graduate Research Assistant **2014–2016**
University of Toronto, Irvine *Toronto, Canada*

TEACHING EXPERIENCE

Instructor of Record, BME60B **2021**
University of California, Irvine *Irvine, California*

Teaching Assistant, BIO **2019**
University of California, Irvine *Irvine, California*

Teaching Assistant, BIOD103 **2018-2019**
University of California, Irvine *Irvine, California*

Teaching Assistant, BME120 **2017**
University of California, Irvine *Irvine, California*

REFEREED JOURNAL PUBLICATIONS

Patterned photocrosslinking to establish stiffness anisotropies in fibrous 3D hydrogels **2021**
Acta biomaterialia

Actively driven fluctuations in a fibrin network **2021**
Frontiers in Physics

Topological defects produce kinks in biopolymer filament bundles **2021**
PNAS

Selective stiffening of fibrin hydrogels with micron resolution via photocrosslinking **2019**
Acta biomaterialia

Evolution of the Vertebrate Resistin Gene Family **2015**
PLOS ONE

Short-chain fatty acids affect cystic fibrosis airway inflammation and bacterial growth **2015**
European Respirology Journal

ABSTRACT OF THE DISSERTATION

Micron scale mechanical response of fibrin hydrogels

By

Qingda Hu

Doctor of Philosophy in Mathematical, Computational, and Systems Biology

University of California, Irvine, 2022

Professor Elliot Botvinick, Chair

How biological fibrous materials respond to forces and changes at the cellular scale is important for understanding what cells 'feel' from their extracellular environment. The local mechanical property within a fibrin fiber network is dependent on the local structure of the network. Elastic force transmission through hydrogel depends on the arrangement of the fiber. A novel method for visualizing force transmission through this network is measuring the pixel fluctuation of individual fibers in the presence of an actively applied oscillation using embedded microbeads and optical tweezers. Optical tweezers can also be used for measuring local stiffness through active microrheology. After micropatterned crosslinking, fibrin hydrogels were shown to produce local stiffening directly and indirectly through strain hardening. This stiffening resulted in stiffness anisotropy and fiber alignment which MDA-231 cells were shown to respond to. Finally, a model of elastically connected nodes recapitulates some of the experimental observations such as fiber force transmission, strain hardening, and stiffness anisotropy when strained. Manipulating, measuring, and modelling of local stiffness changes in response to applied forces offers further insight into how cells sense their surroundings.

Chapter 1

Introduction

Cells can respond to changes in their environment, including physical cues. This includes migration and proliferation of cancer [65, 98], differentiation into neuron or astrocyte [104] , alignment of smooth muscles and endothelial cells [84], angiogenic sprouting [10]. Understanding how cells are affected by their surroundings is important in understanding a wide variety of biological processes. It is often not as simple as how a cell will behave in a stiff or soft matrix. Altered stiffness is typical in cancer and is both seen as a result of cancer progression as well as a driver of progression [38]. MDA-MB-231 is an breast adenocarcionma derived epithelial cell line used as an model of aggressive breast cancer. MDA-MB-231 shows the greatest elongation on stiff PDMS but most motility on intermediate stiffness [3]. MDA-MB-231 shows positive durotaxis on fibronectin-functionalized polyacrylamide hydrogels [45, 27]. Contact guidance is also shown to modulate MDA-MB-231 morphology and motility in aligned collagen hydrogels [55, 96]. Cells can also change the stiffness and structure of their extracellular environment through remodelling. In turn, the changes in stiffness and structure can be felt by cells which can respond to the change. Understanding this crosstalk at the scale of the cells is important but difficult to measure.

Rheology is the study of flow behavior[103], which includes measurement of material properties in biological hydrogels. In elastic materials, rheology experiments can determine the stress-strain relation, while the stress rate to strain rate relation can be determined for viscous materials. Complex materials will both store and dissipate energy, described by the complex shear modulus G*, which is composed of G' the storage modulus and G" the loss modulus. One method for measuring stiffness is parallel plate rheometry, in which the material of interest is placed between two parallel plates and a shear force is applied to one of the plates. For stiffer material, the plate will move less for the same amount of force as compared to with a softer material. For materials such as collagen or fibrin, the stress-strain relationship will change depending on strain rate and magnitude [88]. When this is the case, a frequency sweep and a strain sweep can be used and the stiffness is presented as a function of the testing parameters. A limitation of parallel plate rheometry is that it measures the bulk property of the whole piece of material between the plates. This means that heterogeneity in the material would not be able to be measured by this method [64]. Another method to measure stiffness is indentation, where a probe is pushed down onto the material to measure the displacement-force relation. The harder the material, the less it will deform for a set amount of force applied. To account for material heterogeneity, atomic force microscopy (AFM) can be used, where the probe is small enough to indent an individual collagen or fibrin fiber. AFM has been used to pull on individual or small network of fibrin fibers suspended across a microtroughs [79, 42]. AFM is ultimately limited to where the probes can reach and can not measure inside 3D hydrogels.

To investigate heterogeneity inside of materials, microrehological techniques using embedded beads are one option. Passive microrheology measures the Brownian motion of particles to quantify the material properties. The diffusion of particles are dependent on the viscosity of the material, the temperature, and the size of the bead. The material property can also be tested by active microrheology (AMR), in which forces can be applied to the beads either with optical tweezers or magnetic tweezers. Optical tweezers use a focused laser beam which

will impart a force on a glass or polystrene bead towards the focus of the laser [110]. The trap stiffness of the optical tweezers is linear close to the focus of the laser and can be thought of as a simple spring. The trap stiffness can be measured by determining the corner frequency in the power spectral of the position of a bead trapped in the optical tweezers. To measure outside of the linear region other methods such as the drag method can be used, where a bead trapped in the optical tweezers experience drag either by moving the fluid around the bead or moving the optical tweezers at a constant velocity. The drag force is equal to the trapping force for a bead that stationary relative to the focus of the laser. The response of the bead to a known amount of force is used to measure the apparently material properties surrounding the bead. Oscillation of optical tweezers with a frequency sweep is typically used for complex materials.

Fibrin is a major fibrous component of blood clots. The fibrin network is formed when fibrinogen is activated through cleavage by thrombin [128]. Thrombin cleavage uncovers binding domains on fibrinogen molecules that can interacts with other fibrinogen molecules to form insoluable fibrin fibers. Cells are then recruited to the wound and healing takes place, eventually replacing the temporary fibrin matrix with the original environment before injury. This makes fibrin an interesting biomaterial as it forms a hydrogel quickly, is naturally derived, and is thus biodegradable [115]. There are fibrin glue on the market for used for surgery to stop bleed and promote healing. The maturation of fibrin through crosslinking by factor XIII occurs after a clot is formed, leading to a stiffer fibrin matrix [66]. Modification of stiffness properties of hydrogels is important for both research and biomedical applications. The stiffness of fibrin hydrogels is dependent on the fibrinogen and thrombin concentrations used [3]. Natural crosslinking process such as factor XIII can be used to modulate hydrogel stiffness [66, 50]. There are also many artificial methods for forming corsslinks, one such method is using tris-bipyridylruthenium(II) with ammonium persulfate. Light activation of the ruthenium crosslinking agent generates a tyrosine radical intermediate which can form a crosslink with another nearby tyrosine radical or a nearby by lysine or cysteine group

[30]. This process crosslinks any proteins present and nearby. Use of this ruthenium based crosslinker in fibrin hydrogels with cells showed that cells tolerated the crosslinking process [121]. The crosslinked fibrin was also shown to not induce additional inflammation when implanted subcutaneously [9]. This nonspecific crosslinking method seems compatible with hydrogels embedded with cells.

Fibrin is not linear elastic at the macroscale. Measurements with parallel plate rheometer shows strain stiffening where as polyacrylamide, which has linear elastic behavior, does not [50, 49]. At the microscale, individual fibrin fibers also show non linear elastic behaviour. This behaviour is due to the coiled nature of the fibrinogen monomer [79]. Comparison of parallel plate rheometry and microrheology with optical tweezers shows that heterogeneity is present around cells which cannot be detected at the macroscale [52]. Bead based microrheology is not able to fully quantify this heterogeneity as interpolation between measurements at the beads does not work due to the fibrous nature of the hydrogel, requiring measurements at a even finer spatial scale [53, 54]. The fibrous nature of fibrin and other fibrous protein networks play a major role in the material response at the cellular scale, and so measurements at the fiber scale are required to understand what signals cells receive through the network of fibers [42, 107, 81].

Tracking the displacement of small embedded fluorescent microbeads has shown the non-linear, anisotropic nature of deformations in biological fibrous networks [95, 69, 60]. Although the displacement can be measured, the heterogeneity of material properties makes calculating the forces that would lead to the observed deformation challenging. Even with approaches like AMR, the stiffness landscape map does not have the necessary spatial resolution for this calculation. Additionally, the continuum assumption that model synthetic materials with smaller pores and homogeneous, linear elastic properties fail when used with fibrous biological networks [81]. Modelling was used to gain insight into the observed non-linear, anisotropic behaviours, such as the importance of fiber tension, fiber buckling, and fiber alignment due

to preloaded stresses greatly impact the material response [95, 69, 60]. Forces applied with in fibrous networks are transmitted through fiber, which make up a small volume inside hydrogels, and simulations show that forces are only transmitted through a subset of these fibers, which Dr. Alex Levine has termed 'force highways' [34]. Work in this dissertation demonstrate novel methods for observing and manipulating the mechanical response of fibrin fiber networks.

Chapter 2

Detection of fiber motion in response to optical tweezers oscillations of embedded microbeads

The text of this thesis/dissertation includes reprint of the material as it appears in "Actively Driven Fluctuations in a Fibrin Network" [41]. The co-author listed in this publication were involved in the data analysis and writing which forms the basis for the first aim of my dissertation.

2.1 Background

The extracellular matrix (ECM) interacts with and provides a variety of mechanical and biochemical cues to cells [50, 49]. Experimental systems using naturally derived ECMs more closely mimic *in vivo* cell-ECM interactions than, for example, plastic [28]. Common naturally derived ECMs such as collagen and fibrin hydrogels exhibit important characteristics such

as micron-scale pores and cell adhesion sites [15]. The fibrous nature of these ECMs plays potentially critical roles in cell-cell communication through the ECM, especially in 3-D culture systems [99, 14]. For example, cells respond to forces an order-of-magnitude farther away in naturally derived fibrous materials than materials with sub-micron pores, often treated as a continuum at the cellular scale [118, 107, 81, 106]. Therefore, understanding force propagation through naturally derived fibrous materials at the cellular scale is of great interest. Fibrin, a major component of hemostasis, is well suited for studying force propagation through fiber networks. Fibrin forms the provisional ECM of a blood clot, is used as tissue glue, and is a substrate for the study of wound healing and in tissue engineering [22, 89, 26, 129]. Fibrin hydrogels can be formed by activating soluble fibrinogen with thrombin, which forms a randomly arranged 3-D network of fibrin fibers.

At the fiber scale, experimental observations using optical tweezers and atomic force microscopy (AFM) as well as computational simulations show that individual fibers act as strain stiffening elastic beams [23, 79, 57, 42, 133, 74]. While force transmission at the scale of single fibers is well understood, force transmission in assembled networks has not been fully elucidated [34]. At scales much larger than the average pore size, the material can be treated as a continuum, but at the scale of pores, and even cells, it is necessary to consider that forces cannot elastically transmit through the liquid region and are confined to the fibers [126, 81]. At this mesoscale, the existence of a preferred pathway for force transmission or a 'force transmission highway' has been observed in simulations and inferred in experimental observations [118, 81, 95, 82, 93, 34]. Simulations that take into account the fibrous structure of the ECM show that when the matrix is extended, subsets of fibers within the network carry higher tension than would be expected from a continuum model of the material, while other fibers carry less tension or are buckled under compression [126, 95]. How and where these high tension pathways form and change may play a role in cell orientation [125], cell migration or invasion [56, 112], and capillary sprouting [63]. A method for directly assessing which fibers in a network carry tension can provide insight into force transmission at this

mesoscale.

Here, we describe an approach to detect which fibers within a 3-D fibrin hydrogel are involved in force transmission. Optical tweezers are used to apply a low frequency oscillatory force to a bead embedded in a fibrin network. We measure the response of the fibers within the network using confocal microscopy by analyzing the fluctuation of the fluorescence intensity. Both confocal microscopy and optical tweezers are able to access regions deep within a hydrogel without invasive disruption of the structure, unlike AFM. Future studies will aim to extend this method for identifying force transmission pathways around cells and to study how naturally derived ECMs participate in cell-cell and cell-ECM communication.

2.2 Materials and Methods

2.2.1 Fibrin gel

Bovine fibrinogen (Sigma-Aldrich, F8630) was dissolved in Phosphate buffered saline (PBS; ThermoFisher, 14040117) and sterile filtered 0.22 µm. 2 µm beads (Bang Laboratories, SC05000) were added to the fibrin solution (final concentration 1.5 mg/mL clottable protein) and thrombin (final concentration 4 U/mL; Sigma-Aldrich, 605157) was added immediately before casting the hydrogel in glass bottom dishes (MatTek, P35G-1.5-10-C). After at least 12 hour incubation at 37°C, the fibrin hydrogel was fluorescently labelled using Atto 488 NHS-ester (Sigma-Aldrich, 41698) fluorophore and imaged after washing out excess dye with PBS.

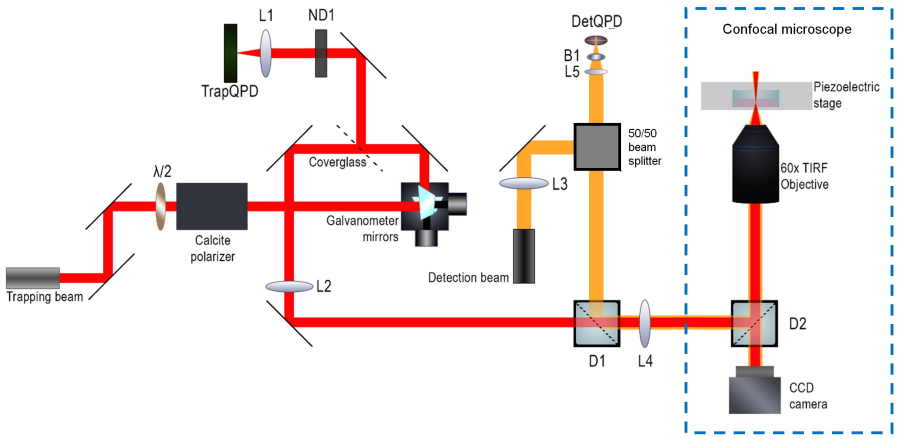

Figure 2.1: Schematic of optical tweezers and confocal microscope. Optical components: λ/2 (half-wave plate), L (lens), D (dichroic mirror), ND (neutral density filter), and B (band pass filter). TrapQPD and DetQPD are quadrant photodiodes recoding the position of the trapping and detection beams, respectively.

2.2.2 Bead Oscillation

A 1064nm continuous wave laser (IPG, YLR-5-1064-LP) was used to optically trap a 2 µm diameter silica bead embedded approximately 35 µm above the glass in a fibrin network with a 60X 1.45 NA oil immersion microscope objective (Olympus). The focused laser beam was steered as a sine wave in the image plane using galvanometer mirrors (Thorlabs, GVS102). Bead displacement was detected by a co-aligned 785 nm (Thorlabs, LP785-SF100) laser-diode beam. The beam was back scattered from the bead and directed onto a quadrant photodetector (Newport, 2901 and 2903). Trap stiffness was determined by trapping a bead without oscillation of the trap and measuring the corner frequency of the displacement power spectrum in water [53]. Laser power was adjusted to achieve a trap stiffness of 34 pN/µm for all experiments. Schematic of the optical tweezer system can be found in Figure 2.1. Optical tweezers were used to oscillate the bead in the x (horizontal in the image) or y (vertical in the image) directions at the desired frequency (driving frequency, F_d). The position of the optical tweezers oscillated as a sine wave with 1 µm peak-to-peak amplitude unless otherwise stated.

2.2.3 Fluorescence microscopy

Fluorescence microscopy images were recorded using an Olympus Fluoview 1200 laser scanning confocal microscope. The Atto 488 NHS-ester fluorophore was excited using the 488 nm laser line operating at 0.7% of maximum power as indicated in the Olympus Fluoview software. Images of fibrin were acquired using the rapid-scanning imaging mode to achieved maximum frame rates of 15.4 frames / second. This imaging mode limits image resolution to 256 by 256 pixels to cover a field of view of 21.1 µm by 21.1 µm unless otherwise stated. 400 consecutive images were recorded over 26 seconds. Z-stacks of at least 10 µm thickness (5 µm above and below the bead) were acquired prior to bead oscillation in order to identify the local fiber network around each bead.

2.2.4 Image analysis

Images in the Olympus OIF format were converted to TIFF files using ImageJ [108]. Pixel-by-pixel 1-D Fourier transforms were performed in MATLAB (MathWorks). Figures were generated with MATLAB. Binary image masks were generated by setting a threshold of mean intensity (in time) of each pixel that is 20% greater than mean intensity (in space and time) of all pixels. Pseudo-color 3-D image stacks were generated using the 'temporal-color code' function in ImageJ and all figures were arranged in Microsoft PowerPoint. Our custom MATLAB code is made available in Supplementary Materials along with all TIFF images. One must first execute *pixelflucatuation.m* for image input and fast Fourier transform computation. Next, *pixelflucatuationfigures.m* should be executed. It operates on the output from *pixelflucatuation.m* to generate all figures. The code as provided assumes all files are placed in the same folder.

2.2.5 Quantification of local phase variance

The Orientational Order Parameter (OOP), also known as the nematic order parameter [85, 18], was used to determine local organization in phase (θ) images. For OOP, the variance in the orientation of n unit pseudovectors ($\vec{r}$, which has components $r_x = cos\theta$ and $r_y = sin\theta$) can be quantified [124, 35, 90]. Pseudovectors are vector-like objects, which are invariant under inversion ($\vec{r} = -\vec{r}$), and are also called "axial vectors" [91]. The OOP ranges from 0 to 1, and will be 0 when the data is uniformly distributed (perfectly isotropic) and will increase as the data becomes more anisotropic towards a value of 1 for perfectly aligned data.

In order to calculate the OOP, the tensor, $\widehat{\mathbb{T}}_i$ in Eq 2.1, is constructed for each $\vec{r_i}$ ($i = 1, \cdots, n$)

$$\widehat{\mathbb{T}}_i = \begin{bmatrix} r_{i,x}r_{i,x} & r_{i,x}r_{i,y} \\ r_{i,x}r_{i,y} & r_{i,y}r_{i,y} \end{bmatrix}. \tag{2.1}$$

The orientational order tensor, $\mathbb{T}$ in Eq 2.2, is constructed by normalizing each tensor $\widehat{\mathbb{T}}_i$ (Eq 2.1), and averaging the normalized tensors. The OOP is the maximum eigenvalue of the orientational order tensor $\mathbb{T}$, shown in Eq 2.2

$$\mathbb{T} = \left\langle 2 \begin{bmatrix} r_{i,x}r_{i,x} & r_{i,x}r_{i,y} \\ r_{i,x}r_{i,y} & r_{i,y}r_{i,y} \end{bmatrix} - \begin{bmatrix} 1 & 0 \\ 0 & 1 \end{bmatrix} \right\rangle. \tag{2.2}$$

In order to quantify local phase organization, the OOP was calculated at each pixel in a 7 x 7 pixel neighborhood. The MATLAB functions *calculate_OOP.m* and *hoodOOP.m*, found in the Supplementary Materials, were used for the OOP calculations.

2.3 Results

Fluorescence confocal microscopy videos were recorded while optical tweezers applied an oscillatory force on a 2 µm bead entangled in a fibrous fibrin network. Supplementary Video 1 shows a bead with no applied oscillation. Supplementary Video 2 shows the same bead oscillated in the horizontal x-direction. The bead and some of the surrounding fibers move noticeably in response to the oscillation of the optical tweezers. For many fibers, motion is difficult to track precisely from frame to frame due to noise. However, a subset of pixels show increased intensity fluctuations at the optical tweezers' drive frequency (F_d) (Figure 2.2). Intensity, denoted as I, is plotted for several representative pixels overlaying the bead, fibers, or liquid region (Figure 2.2A,B). Figure 2.2A shows the mean intensity image, where each pixel is the mean fluorescence intensity over time, denoted by $< I >$. The spectral magnitudes of the 1-D Fourier transform of I in time, denoted by $|\widehat{I}|$, for the representative pixels are plotted in Figure 2.2C. $|\widehat{I}|$ does not show prominent peaks without applied oscillations (Figure 2.2C orange). However, with applied oscillations, some of the representative pixels show a peak at the driving frequency, denoted by F_d (Figure 2.2C blue). Pixel i lies on the bead and a strong peak in $|\widehat{I}|$ occurs at F_d. A similar but less prominent peak is present for pixel ii, which lies on a fiber directly attached to the bead. Pixel v does not lie on a fiber and is instead in the liquid region or pore of the fiber network. We found that $|\widehat{I}|$ in these regions are insensitive to the applied bead oscillation and pixels in these regions also have lower I as well as lower $|\widehat{I}|$ at all frequencies. Pixels iii and iv lie on fibers farther away from the bead, which are not directly connected to the bead by the in-focus portion of the fiber network (Figure 2.2A). Determining if these fibers are oscillating with the bead can be difficult based on the spectral plot of individual pixels as presented in Figure 2.2C, when $|\widehat{I}|$ at F_d is near to the mean $|\widehat{I}|$ across all frequencies. We can improve identification of fibers which are mechanically coupled to the bead by taking into account the intensity fluctuations of all the pixels over each fiber. We can visualize these spatial relationships in $|\widehat{I}|$ images

(Figure 2.3, Supplementary Video 3 bottom). As an example, Supplementary Video 3 shows the $|\widehat{I}|$ images series for the same bead as in Figure 2.2 with (bottom right) and without (bottom left) applied oscillation. Even without applied oscillations, fibers are visible in these $|\widehat{I}|$ images (example: Figure 2.3A) as regions of increased $|\widehat{I}|$ relative to the liquid regions that form the pores within the fibrin network. When an oscillation is applied, $|\widehat{I}|$ images are similar to the no-oscillation condition, except at F_d (Supplementary Video 3 bottom, Figure 2.3A-D) where regions of elevated $|\widehat{I}|$ are evident and lie on a subset of fiber pixels. To remove the portion of $|\widehat{I}|$ which is independent of applied oscillations, we first define a background image $< |\widehat{I}| >$ to be the mean value of $|\widehat{I}|$ across all frequencies, excluding 0 and F_d (Figure 2.3E) and then $< |\widehat{I}| >$ is subtracted from each $|\widehat{I}|$ image (example: Figures 2.3F-H). For the remainder of this paper we redefine $|\widehat{I}|$ as $|\widehat{I}|$-$< |\widehat{I}| >$ to simplify notation, unless otherwise noted. The $|\widehat{I}|$ image at F_d (Figure 2.3G) highlights oscillating pixels, but cannot identify the fibers that do not oscillate, since fibers not oscillating in Figure 2.3G are indistinguishable from the liquid region. To identify both oscillating and non-oscillating fibers, image masks can be generated from $< I >$ images (example: Figure 2.2A) and applied to $|\widehat{I}|$ images (example: Figure 2.3I-K). Reexamination of pixels *iii* and *iv* from Figure 2.2 shows that the fiber containing pixel *iii* is oscillating in response to the bead while pixel *iv* is not (Figure 2.3G,K). In summary, an increase in pixel intensity fluctuations can be detected for subsets of pixels when oscillatory forces are applied to the fiber network. Such pixel intensity oscillations preserve the frequency of the applied force and are identifiable after mean-magnitude subtraction.

In addition to $|\widehat{I}|$, we investigated the corresponding phase of pixel fluctuations, $\angle\widehat{I}$ (Supplementary Video 3 top). In the absence of applied oscillations, $\angle\widehat{I}$ is random and uniformly distributed (Figure 2.4A,B). When an oscillation is applied to the bead, the $\angle\widehat{I}$ at F_d displays local organization along some of the fibers. These fibers appear as two joined parallel lines shifted in phase by π radians (Figure 2.4D). The phase distribution of all pixels becomes non-uniform exhibiting modes separated by π (Figure 2.4D,E). This π shift is an artifact of

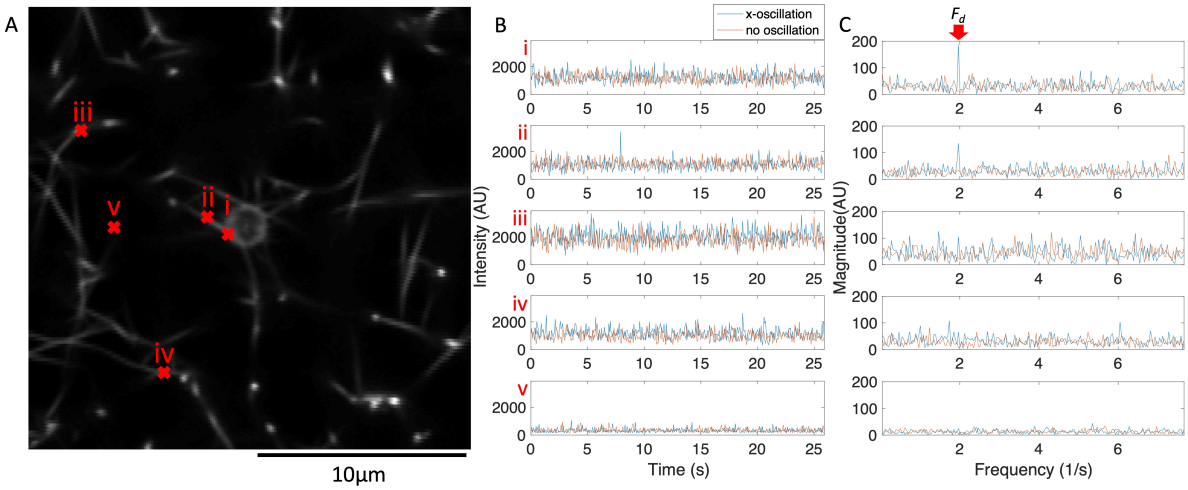

Figure 2.2: The frequency components of pixel intensity fluctuations for a subset of pixels respond to the physical oscillations of the bead. For this subset of pixels, peak intensity fluctuations occur at the same frequency as the optical tweezers oscillation (F_d). (**A**) Time averaged fluorescence intensity image. White regions are fibers labelled with fluorescent dye. The bead is in the center of the image. Red X symbols indicate the position of representative pixels shown in panels B and C. Point *i* is on the edge of the bead. Point *ii*, *iii*, *iv* are on fibers. Point *v* is in the liquid region. (**B**) Fluorescence intensity of pixels over time with optical tweezers either oscillating in the x-direction (blue) or not oscillating (orange). (**C**) Magnitude spectra of the 1-D Fourier transformed fluorescence intensity in time with optical tweezers either oscillating in the x-direction (blue) or not oscillating (orange). A red arrow highlights F_d.

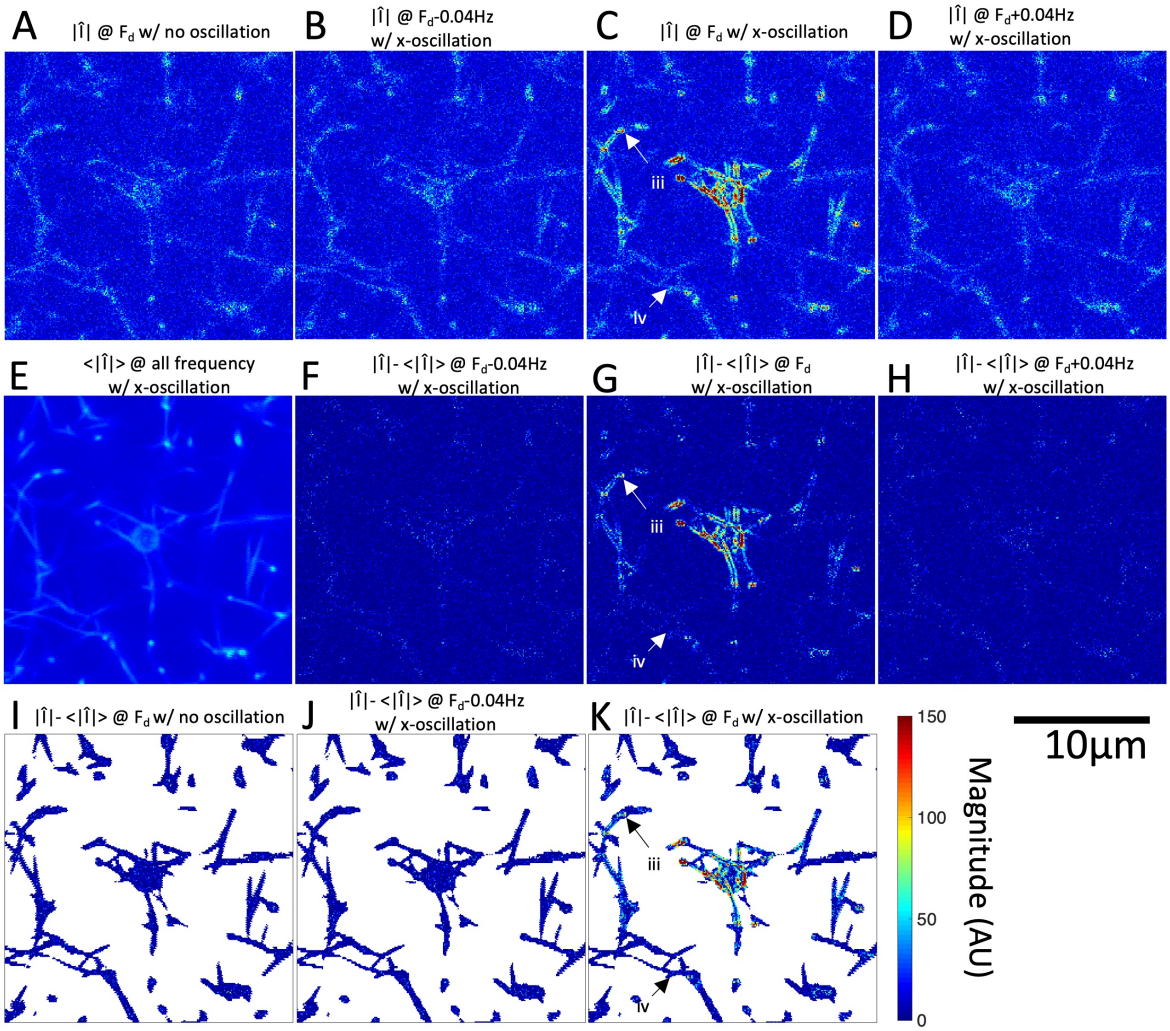

Figure 2.3: Fourier magnitude image at F_d identifies subsets of fibers which oscillate with the optically trapped bead. Identification of these fibers can be improved by mean-magnitude background subtraction and masking of the liquid regions. (**A**) Fourier magnitude at F_d with no applied bead oscillations. Fourier magnitude at (**B**) $F_d - 0.04$ Hz, (**C**) F_d, and (**D**) $F_d + 0.04$ Hz while the bead is oscillated in the x-direction. (**E**) Mean magnitude image over all frequencies excluding 0 Hz and F_d. Mean-magnitude subtracted images at (**F**) $F_d - 0.04$ Hz, (**G**) F_d, and (**H**) $F_d + 0.04$ Hz while the bead is oscillated in the x-direction. (**I**) Mean-magnitude subtracted image at F_d while bead is not oscillated displaying only pixels covering the fiber network. (**J**) Mean-magnitude subtracted image at $F_d - 0.04$ Hz displaying only pixels covering the fiber network. (**K**) Mean-magnitude subtracted image at F_d displaying only pixels covering the fiber network. Arrows in panel C, G, and K indicate locations of pixels *iii* and *iv* in Figure 2.2.

imaging due to the motion of the fibers relative to the fixed position of pixels, such that as a fiber moves rightwards, the pixels on the right side of the fiber get brighter. At the same time, pixels on the left side of the fiber get dimmer. The relationship reverses as the fiber moves leftwards. This distinct pattern allows for easy identification of the oscillating fibers by eye. We can distinguish the background liquid region and non-oscillating fibers which both have random $\angle\widehat{I}$ distributions by applying the $< I >$ mask to exclude the liquid regions just like we did with the $|\widehat{I}|$ image (Figure 2.4G). Notably, the fibers which have increased $\angle\widehat{I}$ organization in Figure 2.4G match the fibers which show increased $|\widehat{I}|$ in Figure 2.3K (Figure 2.4C,F). The organization of the phase of the pixel intensity fluctuations at F_d can be quantified using the Orientational Order Parameter (OOP), which treat the phase vectors as pseudovectors with components equal to $cos(\angle\widehat{I})$ and $sin(\angle\widehat{I})$ (Figure 2.4H) [124, 35, 90]. A locally disordered system will have a local OOP of 0 while a locally ordered (i.e. aligned) system will have a local OOP of 1. In this work, we define "local" to be pixels in a 7 by 7 pixel neighborhood. In summary, fiber fluctuations resulting from forced bead oscillations are detectable by $\angle\widehat{I}$ and $|\widehat{I}|$, while local organization of $\angle\widehat{I}$ can be quantified using OOP.

We have shown that oscillation of the optical tweezers with an amplitude of 1 µm results in a response from the bead and a subset of the fiber network detectable by the $\angle\widehat{I}$, $|\widehat{I}|$, and OOP. Next, we investigate how $\angle\widehat{I}$, $|\widehat{I}|$, and OOP change with oscillation amplitude or direction (Figure 2.5). There is a subtle increase in the $|\widehat{I}|$ as the amplitude of oscillation was increased from 1 µm to 1.2 µm (Figure 2.5A). While it is difficult to directly identify differences in the $\angle\widehat{I}$ in response to increasing the amplitude of oscillation, the increased fiber recruitment and phase organization of already oscillating fibers is apparent when looking at the OOP image (Figure 2.5B,C). Conversely, decreasing the amplitude of oscillation results in decreasing $|\widehat{I}|$ and OOP (Figure 2.5). At an oscillation amplitude of 0.2 µm, the $\angle\widehat{I}$, $|\widehat{I}|$, and OOP are indistinguishable from the no-oscillation control (Figure 2.5). Subtle differences appear in the $\angle\widehat{I}$ and OOP images with oscillations at or above 0.5 µm, but not the $|\widehat{I}|$ image (Figure 2.5). This indicates that the $\angle\widehat{I}$ is more sensitive to small oscillations in the

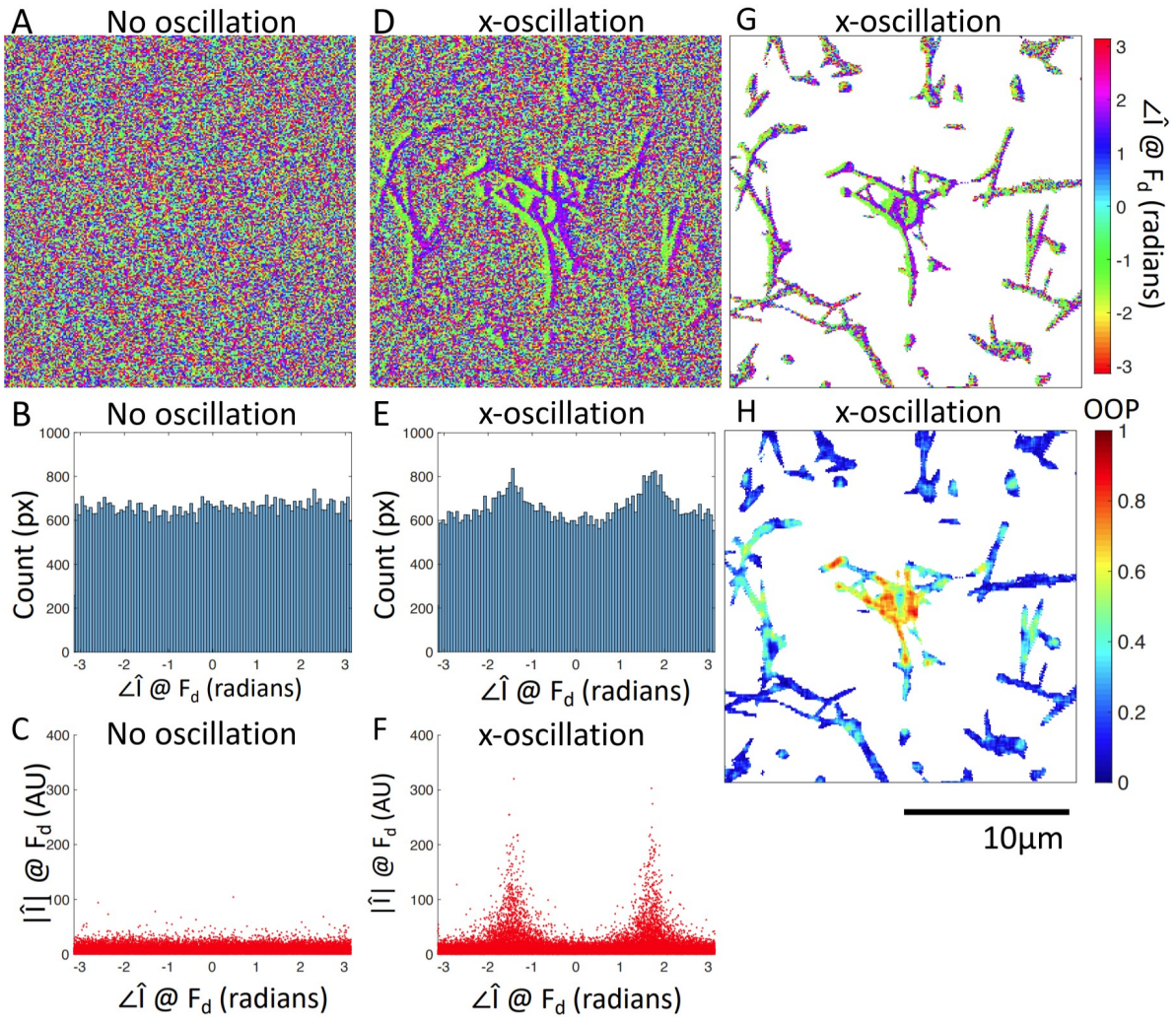

Figure 2.4: Fourier phase images at F_d identify subsets of fibers which oscillate with the bead. (**A**) Phase image at F_d with no applied oscillation. (**B**) Histogram of the phase image in panel A showing uniformly distributed phase. (**C**) Comparison of phase and magnitude for each pixel with no applied oscillation. (**D**) Phase image at F_d with oscillation applied in the x-direction. The two sides of the bead and some fibers show a distinct pattern. (**E**) Histogram of the phase image in panel D showing 2 peaks in the distribution of the phase. (**F**) Comparison of phase and magnitude for each pixel with oscillation applied in the x-direction. Pixels with increased magnitude tend toward one of the peaks in the phase distribution. (**G**) Phase image at F_d from panel D displaying only pixels covering the fiber network. (**H**) Local OOP of the phase image from panel D displaying only pixels covering the fiber network. Local OOP is computed for each 7 by 7 pixel region. The organized regions have high OOP and the unorganized regions have low OOP.

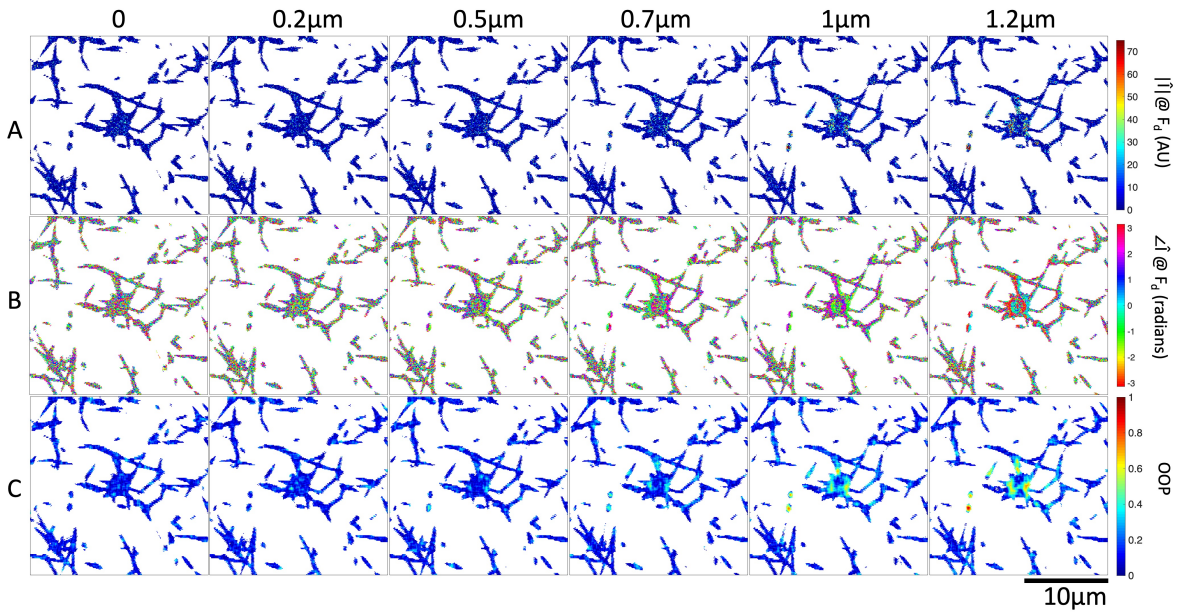

Figure 2.5: Increasing optical tweezers oscillation amplitude results in increased Fourier magnitude and more organized Fourier phase at F_d. The amplitude of optical tweezers oscillation is indicated at the top of each column. (**A**) Fourier magnitude at F_d for a bead within a fibrin fiber network. Corresponding (**B**) Fourier phase and (**C**) local OOP at F_d are shown.

fiber network than the $|\widehat{I}|$. Now that we have shown pixel fluctuations are dependent on the optical tweezers oscillation amplitude, we next investigated if the subset of image pixels that are phase coupled (i.e. on fibers) changes with bead oscillation direction. Experiments are repeated with forced oscillations in the y-direction after oscillations in the x-direction, both with 1 µm oscillation of the optical tweezers. The in-focus fiber network structure can be seen in the $< I >$ image for each bead (Figure 2.6A). It is observed that some subset of the fiber network responds to the oscillation of the bead and this response can been seen in the $|\widehat{I}|$, $\angle\widehat{I}$, and OOP images (Figure 2.6B-G). The subset of engaged fibers is dependent on the direction of the bead oscillation (Figure 2.6 arrows). We can compare the response of the fiber network to the direction of oscillation by looking at the differences in $|\widehat{I}|$ images between applying oscillation in the x-direction or y-direction. It is apparent that some regions of the fiber network are more responsive to oscillation in the x-direction (blue) or oscillation in the y-direction (red) (Figure 2.7A). This preference in response suggests fluctuations travel

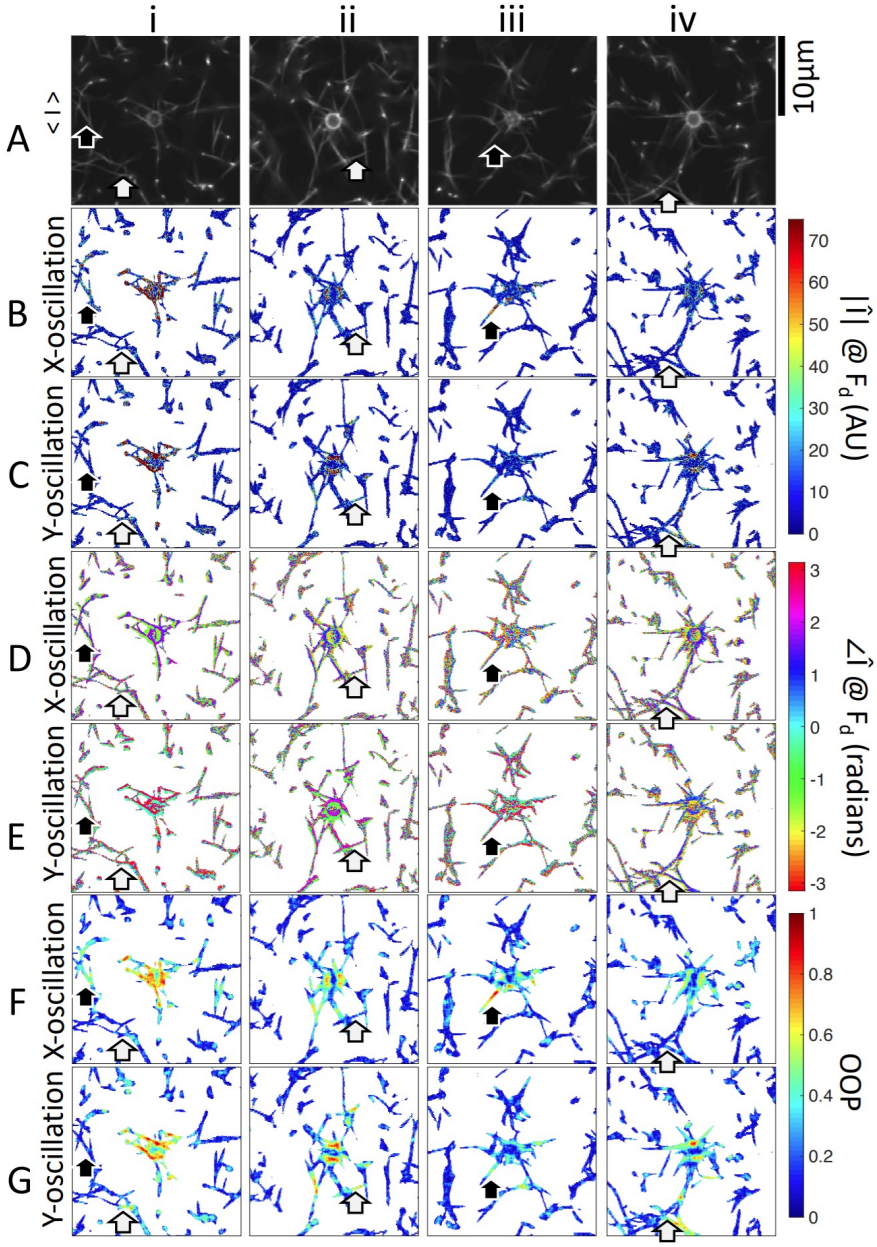

Figure 2.6: Fourier magnitude, phase, and OOP images of four beads embedded in fibrin networks oscillated in the x-direction or y-direction. *i*, *ii*, *iii*, and *iv* are different beads.(**A**) Fluorescence microscopy images showing the bead and fibers. Mean-magnitude subtracted images at F_d for oscillation in either the (**B**) x-direction or (**C**) y-direction. Phase images at F_d with oscillation in either the (**D**) x-direction or (**E**) y-direction. OOP images at F_d in either the (**F**) x-direction or (**G**) y-direction. Black arrows indicate regions where the network responds more to oscillations in the y-direction while white arrows indicate the opposite.

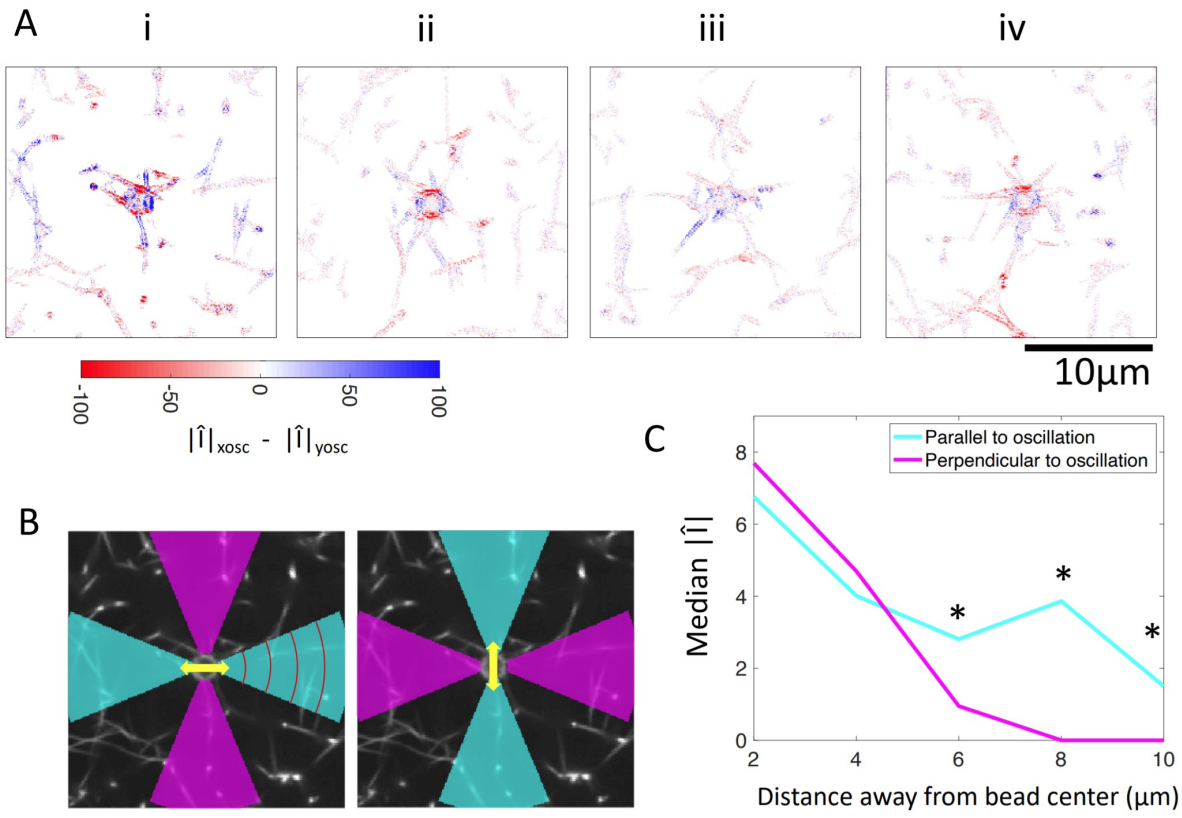

Figure 2.7: Comparison of Fourier magnitudes in response to applied oscillations in the x-direction and y-direction. (**A**) Difference between Fourier magnitude at F_d in response to x-oscillation and y-oscillation. Blue indicates greater response to x-oscillation while red indicates greater response to y-oscillation. *i*, *ii*, *iii*, and *iv* match the beads shown in Figure 2.6. (**B**) Image illustrating binning for panel C. Yellow arrow indicates the axis of oscillation. $\pi/4$ radian wide regions parallel (cyan) or perpendicular (magenta) to the axis of oscillation are binned according to their distance from the center of the bead with a bin width of 2 µm, indicated by the red arcs. (**C**) The median of the Fourier magnitude for each bin is plotted (Figure 2.10 presents the distribution of the data as violin plots with quartile ranges). *indicates medians are statistically different as determined by Wilcoxon rank sum test ($p < 10^{-5}$).

farther through the network along the axis of oscillation. This trend can be visualized by comparing $|\widehat{I}|$ of pixels located along the oscillation direction of the bead to the pixels located perpendicular to the oscillation direction (Figure 2.7B). Four regions of the $|\widehat{I}|$ image from Figure 2.6B,C, each $\pi/4$ radians wide, are denoted as either parallel (cyan) or perpendicular (magenta) to the axis of oscillation (Figure 2.7B). Figure 2.7C shows that $|\widehat{I}|$ of the fibers decreases with distance from the bead, but to a lesser extent in the direction parallel to the oscillation. The force transmission observed in individual experiments is complex and not easily predicted from the $< I >$ image. For example, when bead *iv* in Figure 2.6C is oscillated vertically, fibers below the bead exhibit elevated $|\widehat{I}|$ while fibers above the bead do not. In summary, the response of the fiber network to the oscillation of an embedded bead depends on the fiber network and the direction of oscillation.

2.4 Discussion

We have shown a method to identify which fibers within a 3-D fiber network carry tension in response to the application of a localized force. Specifically, the method determines which fibers are oscillating in phase with an actively driven bead embedded within a pore of the network and assumes that pure elastic forces are driving these fiber motions. Here, fiber oscillation is measured by quantifying intensity fluctuations of all pixels in a plane confocal to the bead. As expected, Fourier magnitudes of pixel intensity fluctuations ($|\widehat{I}|$) at the drive frequency (F_d) are sensitive to even sub-pixel fiber oscillations (Figure 2.2C). By looking at the $|\widehat{I}|$, we find that displacements are larger along the direction of the bead's oscillatory displacement (Figure 2.7), which is also the expected behavior in continuum viscoelastic materials [71]. In our system, however, we do not find quantitative agreement between the continuum-based theory and our data. Unlike in a continuum, we observe displacement propagation along complex paths at the scale of the mesh, likely dependent on

the architecture of the local fiber network (Figure 2.6B,C). In addition to $|\widehat{I}|$, we find that pixels intensity fluctuations along fibers either have random phase ($\angle\widehat{I}$) or exhibit local pixel neighborhoods of similar $\angle\widehat{I}$ occurring on fibers that $|\widehat{I}|$ indicate are under tension. In order to quantify and aid in the detection of such neighborhoods we compute the Orientational Order Parameter, or OOP. By use of the OOP, we identified distinctive sets of fibers that are engaged as the direction and amplitude of oscillation of applied force varied (Figure 2.5C, 2.6F,G). Importantly, while we are interested in the static, or zero-frequency force map, we opt to use low-frequency oscillation of the bead in order to take advantage of lock-in detection and further to provide resilience to forces beyond those applied by the optical tweezers (e.g cell-generated forces). The choice of a low frequency ensures our findings are not complicated by nonlinear material properties of the system that emerge at higher frequency oscillations or viscoelastic properties of the local mesh. Our choice of applying small displacements relative to the scale of the pores also ensures that we are measuring the current state of the system and not further complicate the measurement with additional network rearrangement and fiber alignment that emerge with larger applied deformations [37, 126, 34]. As compared to methods such as fiber tracing and application of static forces, our method may be more suitable for use in the presence of cells or other force centers, which can induce fiber displacements in addition to the actively driven displacements. Also, the lower frequencies and displacements are well within the technical capabilities of our optical tweezers-confocal microscope apparatus.

Force transmission pathways as detected by fiber fluctuation analysis is highly variable from bead to bead due to the different network structure. One consistent observation is that fibers not appearing to be connected to the bead in the confocal $< I >$ image still oscillated in phase with that bead (Figure 2.5, 2.6). This coordination is most likely due to the fact that not all force transmission pathways are in the plane containing the midpoint of the trapped bead. In order to identify potential out-of-plane force transmitting fibers, we overlay the OOP image on top of confocal z-stacks of the fiber network (Figure 2.8). We find that there are

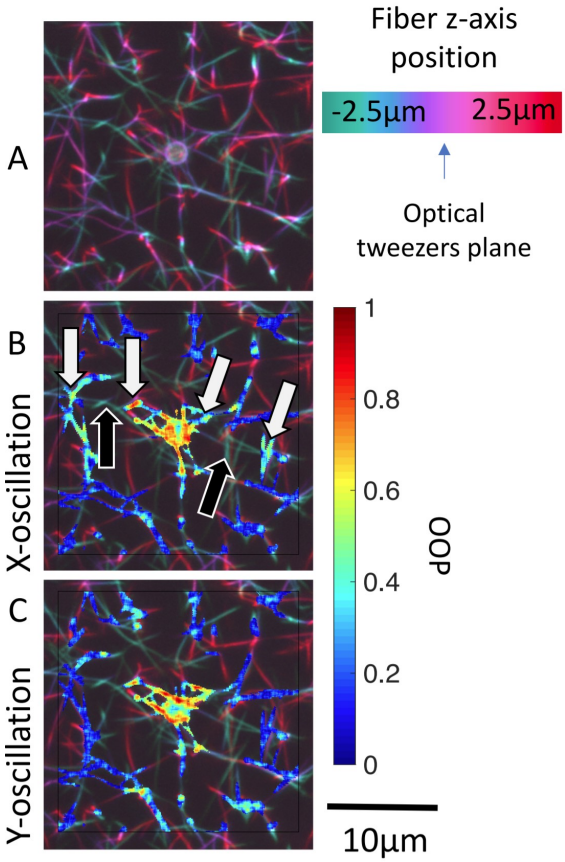

Figure 2.8: Identification of potential out-of-plane force transmission pathways. (**A**) Pseudo color projection is used to encode depth within a 3-D confocal image stack for bead *i* (Figure 2.6). Masked local OOP images are superposed onto the depth images for oscillations in the (**B**) x-direction and (**C**) y-direction. Black arrows indicate out-of-plane fibers which may be transmitting forces. White arrows indicate the oscillating fiber network regions on either side of the out-of-plane fiber. Figure 2.11 shows OOP overlaid on 3-D confocal image stack for beads *i-iv*.

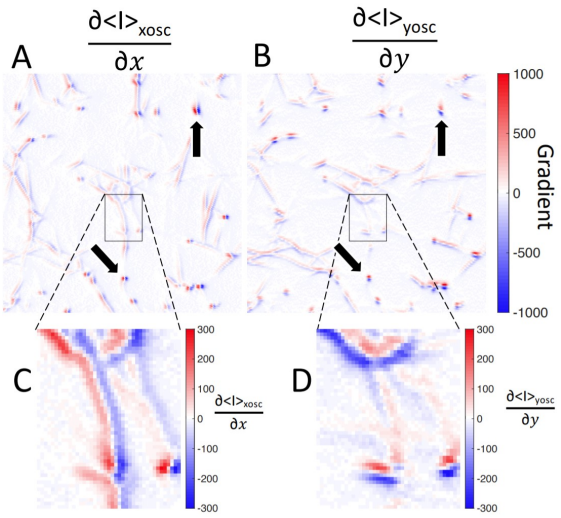

Figure 2.9: Fluorescence image intensity gradients are steep across fibers but not along fibers. Spatial gradients in the (**A**) x-direction or (**B**) y-direction of the mean-intensity image while the bead is oscillated in the (**A**) x-direction ($< I >_x$) or (**B**) y-direction ($< I >_y$). Black arrows indicate some of the brightly fluorescent points in the fibers network which have steep intensity gradients in both directions. (**C,D**) Magnified area showing a vertically aligned fiber which has a distinct gradient across in the x-direction but a shallow gradient in the y-direction.

fibers or a network of fibers which connect all the isolated in-plane high OOP and $|\widehat{I}|$ regions to the bead. Black arrows in Figure 2.8 identify local sets of out-of-plane fibers connected on both sides to fibers exhibiting oscillations as detected by the local OOP (Figure 2.8). It is evident from the data that some fiber chains transmit forces while others do not. Extension of pixel fluctuation intensity analysis to include these out-of-plane fibers is a goal for future method development.

Lastly, we discuss a caveat of this intensity fluctuation analysis. $|\widehat{I}|$, $\angle\widehat{I}$, and OOP should not be directly compared between fibers, especially fibers of different fluorescence brightness $< I >$. More precisely, a major factor determining the $|\widehat{I}|$ is the gradient of fluorescence brightness along the direction of oscillation. For example, the gradients of $< I >$ the along x (Figure 2.9A) and y (Figure 2.9B) axes for bead i in Figure 2.6 are shown. Magnified regions of Figure 2.9A,B show that a fiber aligned with the y axis has steep intensity gradients across the fiber in the x-direction and shallow gradient along the fiber in the y-direction (Figure

2.9C,D). Consequently, detection of oscillation in the y-direction will not be as sensitive as in the x-direction. Of note, punctate bright regions (Figure 2.9A,B black arrows) have steep intensity gradients along all directions and consequently our method should be equally sensitive to oscillations along any axis at such regions. We show that there are parts of the fiber network which have very shallow or non-existent gradient intensity. This lack of gradient is especially evident along a uniformly fluorescently labeled fiber, which makes it difficult to detect the displacement of that fiber. This observation motivates future work in which texture in fiber fluorescence intensity could be introduced to every fluorescent fiber thus mitigating anisotropic sensitivity to displacement. Such texture could be achieved either through a labeling strategy or the use of structured light illumination. A labeling strategy that introduces bright and high contrast images would enable the use of well-established tracking methods such as optical flow analysis, digital image correlation, or erosion-and-reconstruction methods [40, 7, 86, 21, 132, 97, 116, 36, 72, 54].

In conclusion, we developed a straightforward approach to quantitatively determine which fibers are participants in force transmission highways. The use of local variations in the phase of intensity fluctuations provides sensitivity to even small displacements in the fiber network, where magnitude of intensity fluctuations were not distinguishable from noise. Ultimately, we aim to observe changes to the force transmission characteristics of biologically derived fiber networks and how these characteristics change as cells interact with the ECM. While we have shown the response of a fiber network in its relaxed state, future application of this technique lies in exploring how the response changes when the network contains cells. For example, cell contractile forces will apply a tensile preload that may change the subset of tensed fibers thus altering the scope of cell-cell force communication. Such observations of how force transmission pathways change in response to cellular contraction and ECM remodelling offers potentially new insights into processes such as growth, wound healing, cancer growth and metastasis.

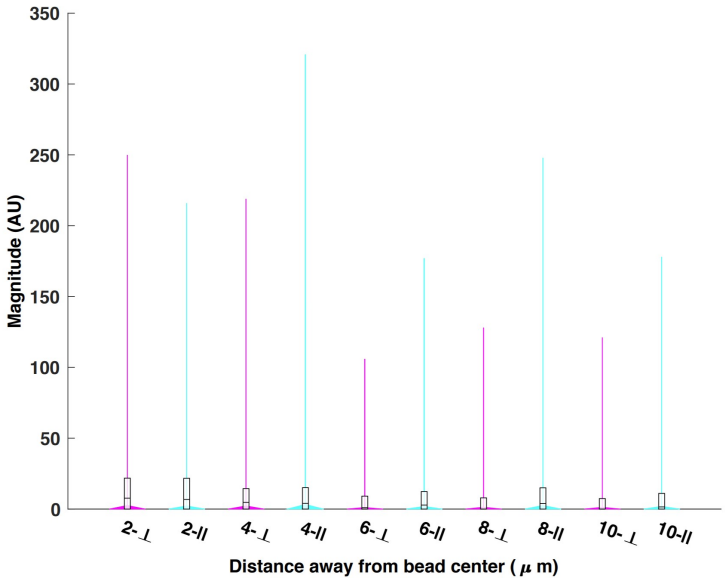

Figure 2.10: Fourier magnitudes of intensity fluctuations for pixels located either along the axis of oscillation or the perpendicular axis. Data is identiacal to that used in Figure 2.7C. Pixels located along the axis parallel ($\parallel$) to oscillation are shown in cyan, and those located along the perpendicular ($\perp$) axis in magenta. The violin plot illustrate the kernel probability density, the median, the first quartiles, and third quartiles for Fourier magnitude of the pixels.

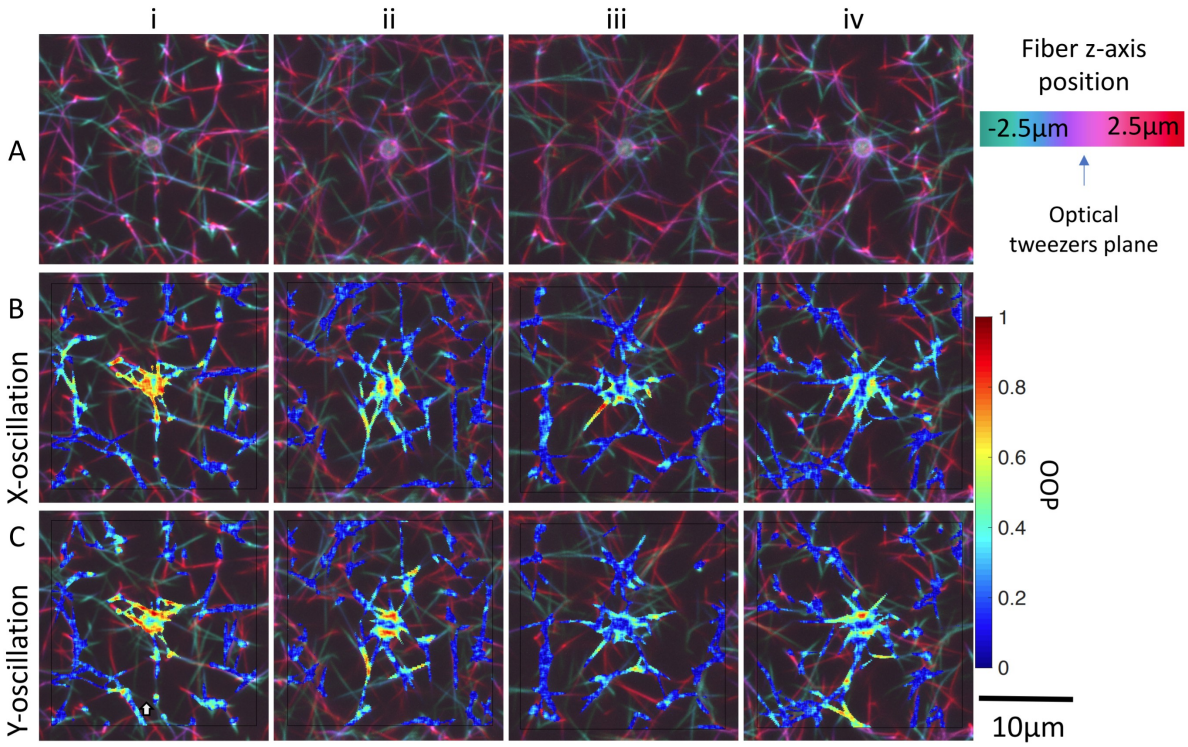

Figure 2.11: OOP images overlaid on 3-D confocal image stacks of the local fibrin network surround beads *i-iv* in Figure 2.6. (**A**) Color is used to encode depth within each 3-D confocal image stack. Superposition of Masked OOP images and confocal image stacks for bead oscillations in the (**B**) x-direction and (**C**) y-direction.

Chapter 3

Micropatterning of fibrin hydrogels using photocrosslinking

The text of this thesis/dissertation includes reprint of the material as it appears in "Selective Stiffening of Fibrin Hydrogels with Micron Resolution Via Photocrosslinking" and "Patterned photocrosslinking to establish stiffness anisotropies in fibrous 3D hydrogels" [54, 47]. The co-authors listed in these publication were involved in the planning, data collection, data analysis, and writing which forms the basis for the second aim of my dissertation.

3.1 Background

Responding to their environment is pivotal for the proper functioning of cells. These stimuli can range from thermal, optical, electrical, or chemical stimuli [75, 127, 117, 114, 70]. Here, I aim to explore how cells respond to the mechanical forces caused by the structure of local extracellular matrix (ECM). Substrate stiffness has been shown to be important for cell migration, proliferation, morphology, and differentiation in 2D experimental setups

[120, 6, 130]. Fibrin is a major component of blood clots and the provisional ECM during wound healing [129]. Fibronogen monomers are enzymatically cleaved by thrombin leading to rapid assembly of monomers into a fibrous network. *In vitro* fibrin hydrogels have been used as a model ECM for studying angiogenesis, stem cells, macrophages, and cancer cell lines [92, 61, 4, 24, 78]. As a hydrogel, fibrin forms a fibrous, viscoelastic, randomly interconnected matrix with pores on the length scale of one micron. Compared to cell-free systems, fibrin stiffness proximal to cells and sprouting endothelial vessels is elevated and more heterogeneous, spanning orders-of-magnitude at the subcellular spatial scale [64, 52]. This phenomenon is possible because fibrin is permissive to cell mediated remodeling by enzymatic breakdown, deposition of new matrix, and other modalities of ECM modification [80, 44].

The mechanical properties of hydrogel can be controlled through the composition, porosity, density, chemical modification [130, 73, 58, 123, 33]. There are also a wide variety of dynamic modifications. Some controllable methods for tuning stiffness in other hydrogels include DNA linkers or mechanical stretching allow for studying of temporally specific stiffness variations [104, 109, 13]. Specifically for fibrin, magnetic aligned hydrogels does utilize strain but still shows stiffness anistropy to which cells respond to [122]. Methods for increasing the stiffness of fibrin hydrogels have been described in literature, including chemical crosslinking via incubation in glutaraldehyde or exposure to UV [20, 25].

The method we used was adapted Bjork *et al.*, who demonstrated crosslinking of fibrin via ruthenium-catalyzed photocrosslinking (RCP) and showed RCP did not reduce cell viability [30, 121]. For RCP, a light activated ruthenium compound (Tris(bipyridine)ruthenium(II) chloride) and sodium persulfate (SPS) oxidizes tyrosine residues in the fibrin forming tyrosine radicals, which can react with other tyrosine residues to form dityrosine in the presence of persulfate [30]. Figure 3.1 shows a schematic for micropatterned photocroslinking using scanning confocal microscope compared to bulk crosslinking using blue LEDs. The degree of crosslinking can be controlled by modifying the concentration of the crosslinker solution, the

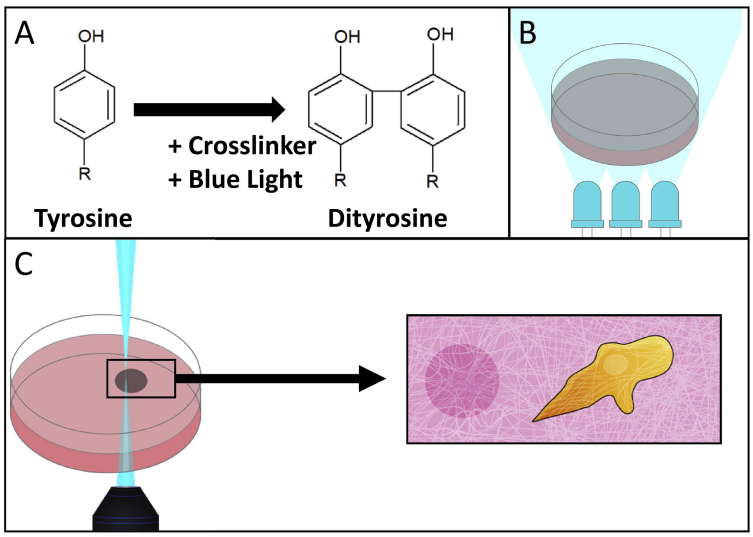

Figure 3.1: Schematic of two crosslinking modalities: laser scanning confocal microscopy and bulk LED illumination. (A) Tyrosine residues are crosslinked to form dityrosine by blue light activated crosslinker. (B) An entire hydrogel can be crosslinked by illumination with 460 nm LEDs. (C) Illustration depicting the intended usage of selective photocrosslinking, where regions proximal to cells could be selectively stiffened by a laser scanning confocal microscope.

wavelength, intensity, and duration of the scanned micropatterning, and the media used to hydrate the hydrogel. For the purposes of micropatterning it was found that by diluting the crosslinker solution in DMEM with FBS, the response of the crosslinker to 559nm light was greatly reduced. The addition of DMEM and FBS was beneficial both for keeping cells viable, as well as allowing for reflection confocal microscopy to monitor the fiber displacement.

Here we present and evaluate an extension of this technique, where we selectively pattern crosslinking within the volume of 3D fibrin hydrogels using a laser scanning confocal microscope and measure induced stiffness changes via AMR. With our method, we have achieved selective stiffening within fibrin hydrogels at scales as small as a few microns, which may be beneficial for future studies on cell-ECM interactions.

3.2 Results from Keating 2019

To demonstrate the selectivity in crosslinking, fibrin constructs were imaged before and after 488 nm laser treatment, which is absorbed by the ruthenium compound to initiate the crosslinking reaction. Circular treatment regions having diameter of either 10 µm or 100 µm are referred to as T10 and T100, respectively. Larger fields of view containing a treated region were imaged by CRM using the 559 nm laser line. Representative fields of view are shown in Figure 3.2A,B in both transmitted light ((i,,ii, iii) and CRM imaging modalities ((iv,v,vi).

Following T100 treatment, embedded microbeads within and beyond the region of treatment were displaced in the transverse plane by several microns (Fig. 3.2A ii–iii). CRM images show elevated pixel intensities in the treated region as compared to non-treated (Fig. 3.2A iv,v). Pseudo-colored composite images of the mesh before and following treatment show that fibers were displaced, notably outside of the treated region (Fig. 3.2A vi, vii). To capture full frame videos of mesh dynamics during the crosslinking process, we implemented a CRM imaging strategy during which full field-of-view imaging at 559 nm was recorded in between every 100 sequential circular scans at 488 nm. Optical flow analysis confirms displacements were predominantly directed radially toward the center of the treated area in T100 treated samples (Fig. 3.2A viii). Peak displacement was located just outside the treatment region and decreased radially in either direction.

We next investigated such displacements for a T10 treated region (10-micron diameter treatment). As compared to T100 treatment, microbeads within and beyond the treatment region were displaced by no more than 500 nm in the transverse plane (Fig. 3.2B i,ii,iii). CRM imagery confirms the effect on the matrix is highly localized to the region of treatment (Fig. 3.2B iv,v,vi,vii). Outside the treated area, displacement was confined to a region immediately proximal boundary as detected by optical flow analysis (Fig. 3.2B viii).

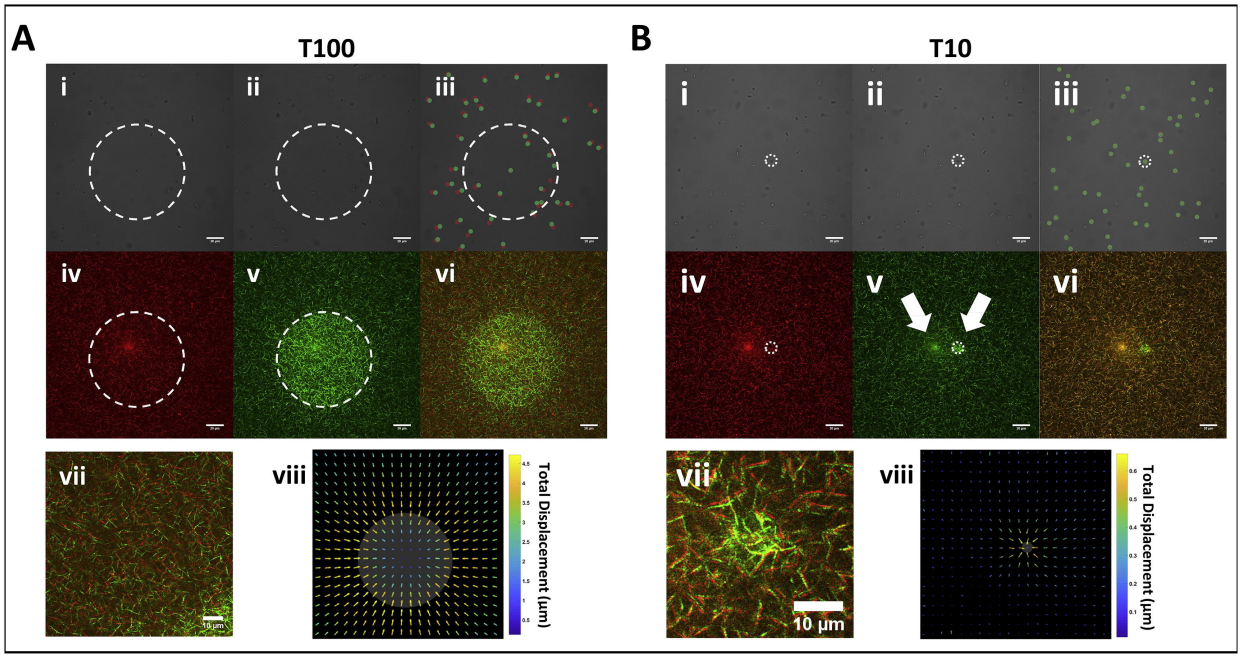

Figure 3.2: Transmitted light and CRM imagery of 100 and 10 µm (referred to as T100 and T10, respectively) diameter treatment spot sizes within fibrin hydrogels before and after photoactivation by 488 nm illumination. (A) Transmitted light images of T100 treatment spot (i) before, (ii) after, and (iii) composite. Probe bead locations in the composite are marked red and green for before and after, respectively. CRM images (iv) before, (v) after, and (vi) composite. (vii) Zoomed inset of the composite image suggests contraction toward treated area, confirmed by (viii) optical flow analysis. Gray area denotes the treated region. Note: Arrow length was scaled for visualization, and color indicates displacement magnitude. (B) Corresponding images and analysis for T10 treatments. Note that the leftmost arrow in (v) points to an imaging artifact common to CRM while the rightmost points to the treated spot. Boundaries of treatment spots are marked with white dashed lines. Scale bars = 20 µm.

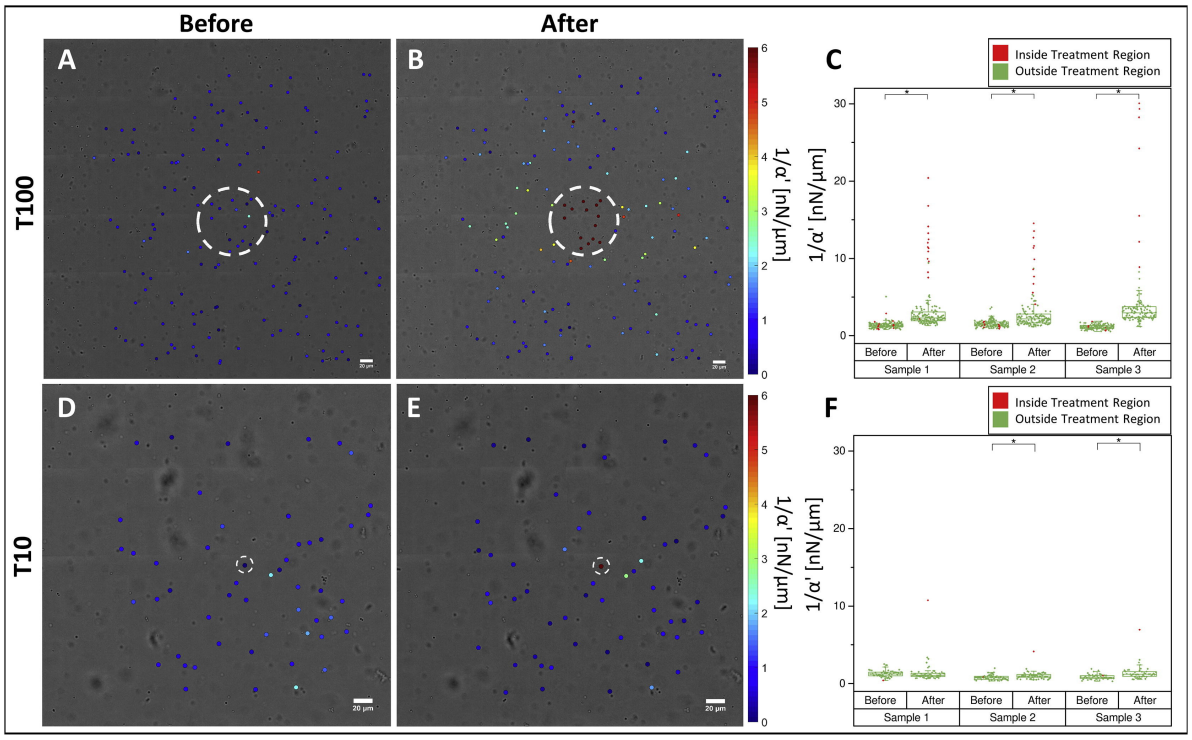

Figure 3.3: Distribution of stiffness within a fibrin hydrogel probed by AMR before and after T100 and T10 treatments. Stiffness maps (A) before and (B) after T100 treatment. (C) Scatter plot of all T100 samples before and after treatment. Stiffness maps (D) before and (E) after T10 treatment. (F) Scatter plot of all T10 samples before and after treatment. (*) denotes significance at 0.05 level via a Mann-Whitney U-Test. Color maps in (A, B, D, E) saturate at 6 nN/µm. Scale bars = 20 µm.

Significant stiffening occurred outside T100, but not T10 treated regions (Fig. 3.3), a result consistent with the displacement fields (Fig. 3.2A). Representative stiffness maps are shown in Figure 3.3. Prior to crosslinking, stiffness is low and heterogeneous throughout the field of view (Figure 3.3A,D). Following treatment, stiffness is notably increased within the treated areas and, for the case of T100 only, outside the treatment area as well (Figure 3.3B,E). The complete set of measurements is shown in Fig. 3.3C,F. On average, increases in stiffness within the treated region were 11.6 ± 7.0 nN/µm and 6.5 ± 3.6 nN/µm for T100 and T10, respectively. Outside of the treated regions, stiffness changes were substantially lower: 1.3 ± 1.3 nN/µm and 0.2 ± 0.4 nN/µm, for T100 and T10, respectively. For all treatments, stiffness increases were statistically significant ($p < 0.05$, Mann-Whitney test, with Bonferroni Correction), except for T10 Sample 1.

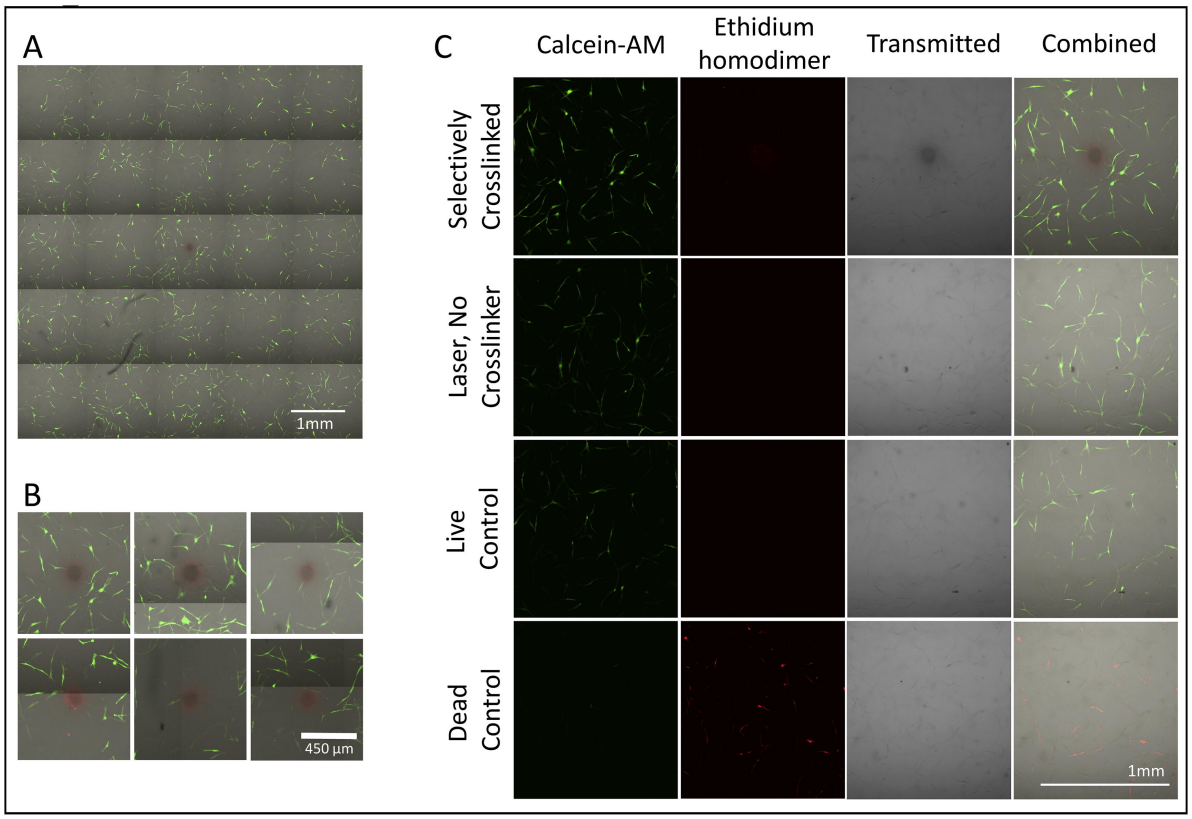

Figure 3.4: Live-dead assay of fibrin hydrogel containing NHDF cells 4 hours after T100 treatment. Calcein-AM (green) stains live cells and ethidium homodimer (red) stains dead cells. (A) Representative 5 by 5 field-of-view montage. (B) Zoomed in view around the crosslinked region for 6 replicates. (C) Areas surrounding (1) a T100 crosslinked region, (2) a control T100 without crosslinker, and (3) live and (4) dead controls. Note: The crosslinked region shows signal in the red channel even in cell-free systems with no ethidium homodimer.

Local hydrogel stiffness was measured by active microrheology (Fig. 3.3). Inside the crosslinked region, stiffness was higher than in the uncrosslinked regions and compared to before crosslinking. However, outside the crosslinked regions, we observed increased stiffness for a subset of the beads. This effect of stiffening outside the crosslinked region is more noticeable when a larger region is crosslinked. Visually, the stiffening seems to be preferential to the right and left of the crosslinked region compared to the top and bottom, as imaged (Fig. 3.3B).

Ruthenium micropatterning crosslinking as we had done so was safe for NHDF (fibroblasts) cells as long as the cells were not in the crosslinked region. I quantified cell viability 4 hours

after crosslinnking with calcien-AM (live) and ethidium homodimer (dead) stains (Fig. 3.4). Zoomed in views of replicate experiments (n = 6) are shown in Figure 3.4B. Figure 3.4C shows results for areas surrounding (1) a T100 crosslinked region, (2) a control T100 without crosslinker, and for (3) live and (4) dead controls.

3.3 Discussion from Keating 2019

In this study we used a photocrosslinking method coupled with a laser scanning confocal microscope to generate patterns of crosslinked areas within a fibrin hydrogel. Crosslinking was indicated by increased pixel brightness and effects on local stiffness were investigated via AMR. Degree of stiffening in the treated region was observed to be as much as 25-fold, which may be significant in the study of roles for stiffness in cell-ECM physical interactions. In fact, we have previously observed cells stiffening their pericellular matrix by as much as 35-fold [53, 52]. For example, in one system, the stiffness proximal to a cell ranged from 16.9 $\pm$ 8.0 nN/µm as compared to its cell-free control 0.8 $\pm$ 0.5 nN/µm [53]. Our laser-mediated crosslinking method can produce a similar range of stiffness at the sub-cellular spatial scale, allowing for exogenous control of local stiffness in a biologically meaningful way.

Interestingly, stiffening was also observed beyond the treatment region where photo-activated crosslinking was not conducted. We examined changes to fibrin mesh architecture outside the T100 treated region to understand the nature of this stiffness change. One possibility is that activated crosslinker diffuses beyond the treated region to generate a gradient of crosslinking. However, crosslinked fibrin is brighter in CRM and regions of increased brightness exclusively overlap the region of 488 nm illumination (Fig. 3.2) indicating that the crosslinking stays confined. Our group has previously shown that fibrin stiffness, as assessed by AMR, increases with fibrin density, which could explain the stiffening [64]. Fibrin density decreased, or remained unchanged, in the stiffened area beyond the treated region. By contrast within

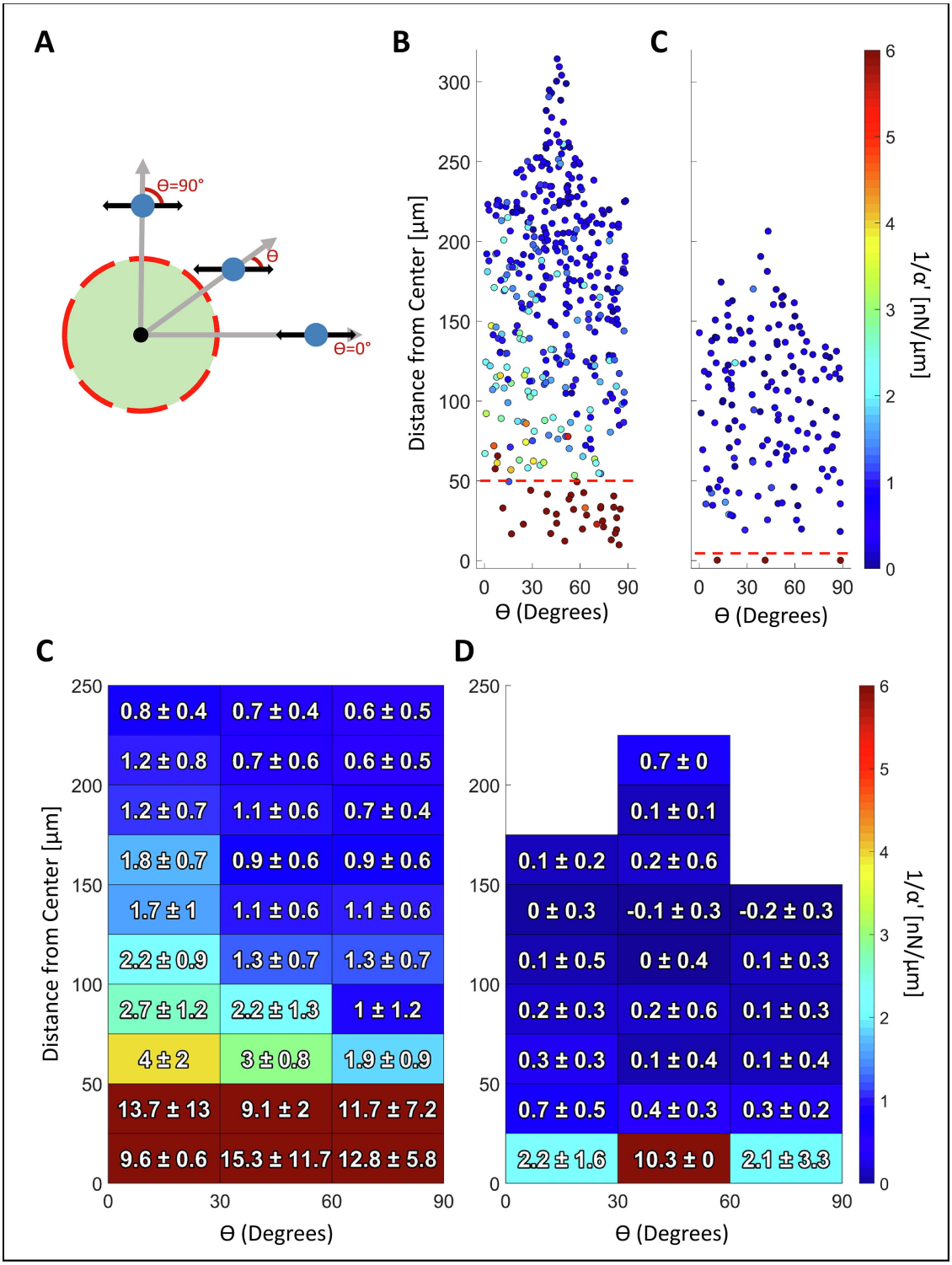

Figure 3.5: Stiffening decreases with radial distance from treated region center. Stiffening for (A) T100 and (B) T10 samples as a function of distance from the treatment area center. Treatment region shaded in green. Fold change presented in (C) and (D) for T100 and T10, respectively. Dotted lines mark the outer radius of the treatment area. (nsamples= 3, per treatment type).

the treated region, both fibrin density and stiffness increased near the treatment boundary. These results suggest other mechanisms are at play, notably stretch-mediated hardening which is supported by the radial inward bead displacement shown in Figure 3.2Aiii. Such a displacement could stiffen the surrounding material through strain hardening, an important characteristic of fibrin and other natural ECMs [77, 111]. Both cell-mediated and exogenous strain have been shown to stiffen these matrices as measured by ourselves and others [53, 64, 51, 131]. In support of strain hardening, the stiffened region (beyond the treatment area) is co-located with the largest displacements of the fibrin mesh (Figure 3.2A, viii). Also, because displacements are overwhelmingly radial, it would be expected that stretch-mediated stiffening should be anisotropic with lesser stiffening in the circumferential direction. While for each bead AMR was exclusively performed along the x-axis, the population of probed beads indicates anisotropy. Specifically, probe beads located near the x-axis are oscillated radially with respect to the treated region, whereas beads located at $\pm$ 90° are oscillated circumferentially. To investigate potential anisotropy, the position of each bead was cast into a coordinate system with the origin at the center of the treated region, and a horizontal x-axis passing through the centroid of that region. The first coordinate is the distance to the origin and the second is the absolute value of angular deviation from the x-axis, defined here as θ (Fig. 3.5A). This angular deviation is important because our AMR system exclusively oscillates beads in the horizontal axis (x-axis). Thus, anisotropy would present as a dependency of stiffness on θ, as was observed (Fig. 3.5B,C). This trend is highlighted when data is binned by θ and distance, as shown for T100 (Fig. 3.5D) and T10 (Fig. 3.5E) Consistent with anisotropy, the radial oscillations reported greater stiffness with an apparent decrease in stiffness with an angular deviation from the x-axis (Fig. 3.5A). Taken together, these results imply that crosslinking a large area can induce stretch mediated hardening in regions not directly affected by the photo crosslinking chemistry, a phenomenon that may be useful in the study of cellular mechanobiology. We also observed matrix remodeling surrounding the treated region for T10 samples, as assessed by confocal imaging (Figure 3.2B,

vii) and optical flow analysis (Figure 3.2B, viii). However, we did not detect stretch-mediated stiffening where fiber displacement was detected, in part due to limitations of the AMR method. Specifically, beads were spaced too far from one another to provide sufficient spatial resolution to allow characterization of local changes in stiffness relative to the treatment spot size. In our experience, the bead density required to achieve bead proximity on the order of several microns alters the structural characteristics of a fibrin gel thus precluding stretch-hardening analysis.

Here we present a method for tuning ECM stiffness within a fibrin hydrogel in select regions. Important to the study of mechanobiology, our method can stiffen local regions at the resolution and dynamic range observed around single cells and cell colonies [53, 67]. In many cell-ECM biophysical studies, the initial stiffness of an ECM has been linked to phenotypical changes including stem cell fate [29, 43]. However, within a permissive environment (such as fibrin), stiffness, architecture, and composition can be modified by cells over time [8, 68], such that the system no longer reflects initial conditions. This holds true for synthetic hydrogels, engineered to be degradable or otherwise, which are also subject to deposition of new matrix by cells [94, 16]. These studies motivated the need for the tool presented in this manuscript, which can make stiffness modifications to fibrin systems on the same order of magnitude that cells can. We verified the exact conditions used in the AMR study did not appear to affect viability of NHDFs, even those adjacent to the treatment zone. It is important to note that methods here will likely require fine tuning to be extended to other cell-ECM experimental systems. There are many factors to consider including: hydrogel composition and density, cell type, cell-ECM ligand interactions and accessibility, culture media, range of stiffness, and required stiffness resolution. To account for these one will likely need to optimize the shape of the crosslinked region, crosslinker concentration, and light dose.

Based on the feedback, we obtained from the work above, we set out to directly measure the stiffness anisotropy from applied micropatterened photocrosslinking in fibrin hydrogels. To

achieve this it was necessary to modify the optical tweezers system. A change was made to measure the location of the bead using the back reflected signal rather than the transmitted interference pattern. This eliminated the effect of the light path above the bead, which included the thickness of the gel, the amount of liquid above the hydrogel, the plastic lid of the dish, glass cover of the incubator unit, and microscope condenser unit. Additional variability in the system was minimized by rebuilding the system in a cage rod system such that optics do not drift relative to each other, reducing the adjustment required before using the system each day. An *in situ* calibration step was added using the piezo stage to account for bead to bead variability in the detection signal response. Taken all together, modification of this system allowed for exploration of stiffness anistropy in many different contexts. This system was also used for several other papers from our lab [122, 46, 48]. Specifically, Thrivikraman *et al.* showed that aligned fibrin fibers led to stiffness anisotropy and a change in cellular behaviour. A strong magnetic field was used to generate hydrogels that have fiber alignment in one direction [122]. This also encouraged us to use a crosslinking scheme which produced a local region which have fiber alignment all in the same direction, which we would expect for rectangular regions of crosslinking due to effective translational symmetry if the rectangle is much longer than it is wide. The following work sets out to answer these questions.

3.4 Results from Jagiełło 2021

In the first set of experiments, a crosslinking solution of ruthenium compound and sodium persulfate was added to 2.3 mg/ml fibrin hydrogels (Fig. 3.6A) and allowed to diffuse for 30 min. Stiffness (κ) of the fibrin network was measured by oscillating embedded microbeads at 0°, 30°, 60°, 90°, 120° and 150° with respect to the horizontal axis of the camera (FOV). These measurements verified that κ of the local fibrin network was isotropic (Friedman test, $p = 0.22$, Fig. 3.6B, C). Afterwards, a crosslinking reaction was initiated by exposing a 50 µm diameter

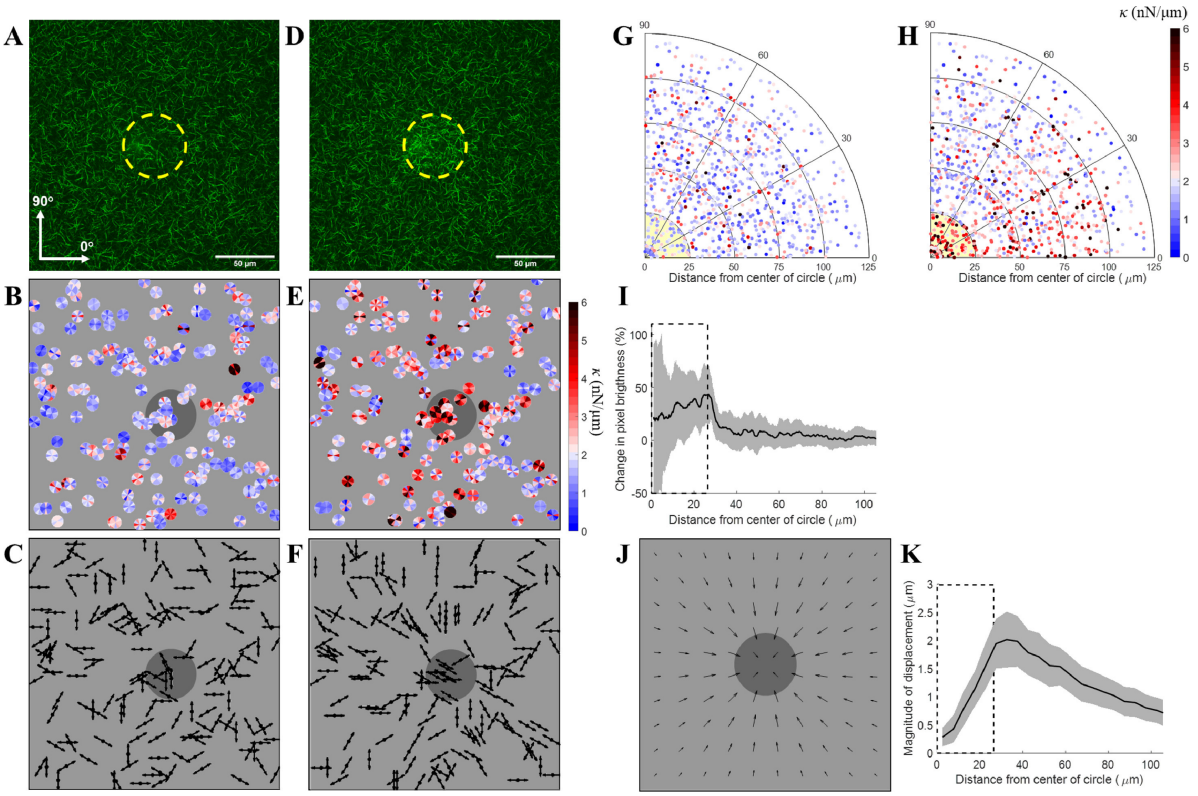

Figure 3.6: The effect of crosslinking a circular region. (A, D) Reflection confocal images before (A) and after (D) crosslinking a circular region marked by the yellow dashed line. Stiffness was probed in 6 directions using multi-axes AMR before (B) and after (E) crosslinking. Stiffness is color-coded separately for each direction of bead oscillation. Crosslinked region is marked by a dark gray background. (C, F) Direction of the highest stiffness is represented by arrows before (C) and after (F) crosslinking. (G, H) Change in stiffness with the distance away from the crosslinked circle center (yellow background) and angle of deviation of probed bead position from the radial direction before (G) and after (H) crosslinking. (I) Change in pixel brightness with distance from the crosslinked circle center. Crosslinked region is denoted by dashed rectangle. Median ± IQR. (J, K) Optical flow detects matrix deformation during crosslinking.

circular region to the 488 nm laser light for the duration of 500 scans (Fig. 3.6D). The effect of crosslinking on stiffness gradients is represented by Fig. 3.6E, F (nbeads = 163, nsample = 4). In Figure 3.6E, κ at each bead is measured in all 6 directions and represented by a segmented circle with segments that align with the axes of oscillation, and are color-coded for stiffness. For each bead, the axis of largest stiffness is plotted in Figure 3.6F. Results indicate that after crosslinking, κ within the circular region increased by a factor of 2.11, when comparing median values across all 6 directions. Stiffness within the circular crosslinked region was also found to be isotropic, based on probing 15 beads ($p = 0.15$). Outside of the crosslinked region, κ also increased, although predominantly in the radial direction. Figure 3.6G, H represent measured κ as a function of distance away from the center of the crosslinked region and the angle by which the axis of AMR oscillation deviates from the radial direction. Stiffness measured along the radial direction is plotted at 0°, while stiffness measured along the tangential direction is plotted at 90°. Before crosslinking, κ was found to be independent of distance from the circle center or deviation angle ($p = 0.52$, Fig. 3.6G). After crosslinking, stiffness probed up to 30° from the radial direction and as far as 75 µm from the crosslinked region was found to be significantly higher than control stiffness (Fig. 3.6H). In fact, within this ±30° bin, stiffness of the crosslinked region did not differ significantly from that of regions located up to 25 µm ($p = 0.55$), 25–50 µm ($p = 0.33$) or even 50–75 µm ($p = 0.22$) away from the crosslinked region. During crosslinking, pixel brightness increased for up to 2000 scans, predominantly inside the crosslinked region (Fig. 3.6I). The displacement of fibers during crosslinking was tracked from reflection confocal images (acquired once per 25 crosslinking scans) using optical flow analysis. During crosslinking, fibers moved radially towards the center of the crosslinked region. The displacement of the fibers was most prominent just outside of the crosslinked region and diminished with distance away from the boundary of the crosslinked region (Fig. 3.6J, K).

Thin rectangular crosslinked regions were also studied due to their intuitive one-dimensional Cartesian symmetry, which was particularly useful when examining the volume between two

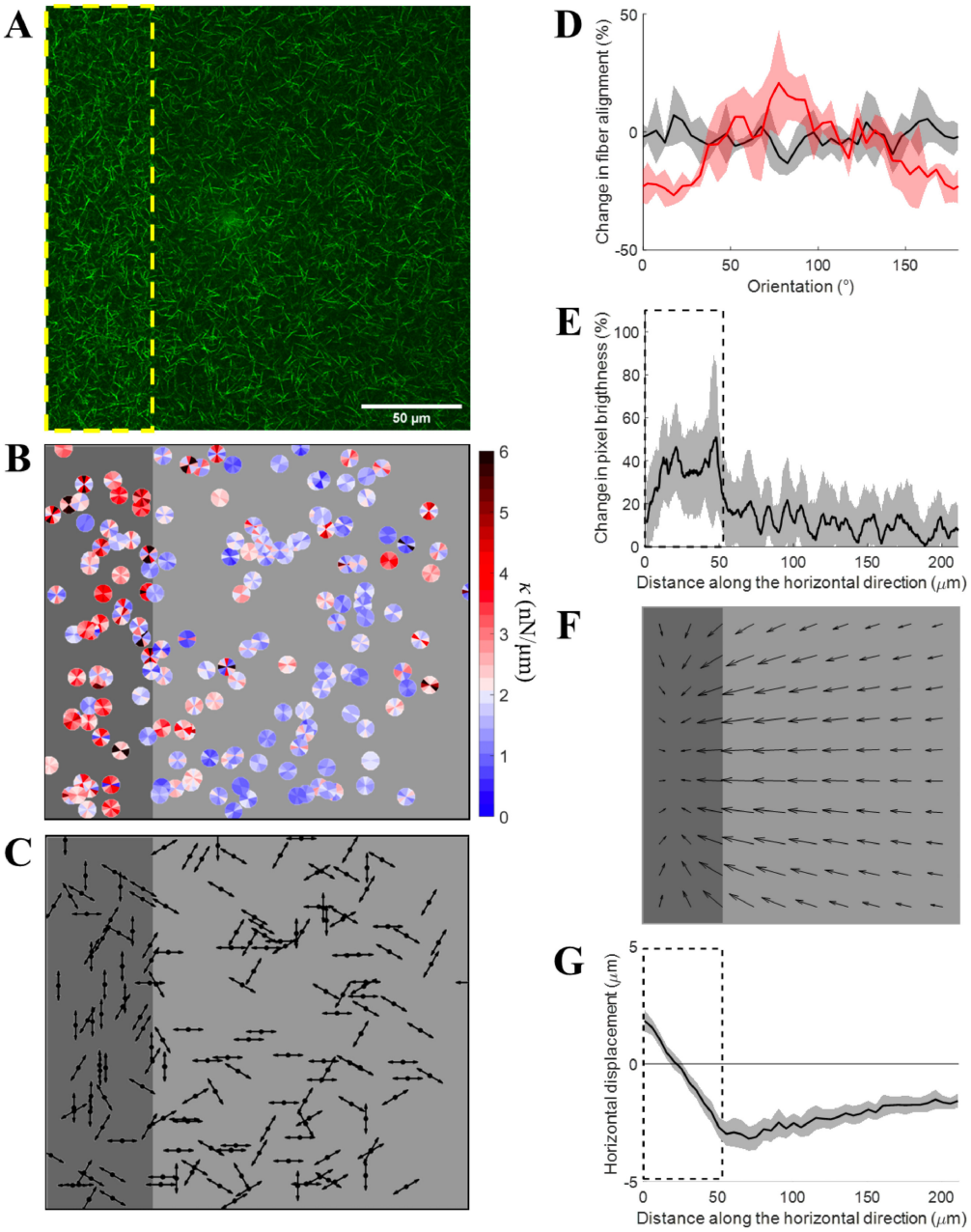

Figure 3.7: The effect of crosslinking a rectangular region. (A) Reflection confocal image after crosslinking a region marked by the yellow dashed line. (B) Stiffness was probed in 6 directions using multi-axes AMR Stiffness is color-coded separately for each direction of bead oscillation. Crosslinked region is marked by a dark gray background. (C) Direction of the highest stiffness is represented by arrows. (D) Fiber alignment within (red) and beyond (black) the crosslinked region. (E) Change in pixel brightness with distance from the crosslinked region (denoted by dashed rectangle). Median ± IQR. (F, G) Optical flow detects matrix deformation.

neighboring crosslinked regions. At first, a single 50 µm by 200 µm rectangular region was crosslinked using the same scanning duration and laser power settings as used for circular regions (Fig. 3.7A). After crosslinking, κ was probed inside and outside of the crosslinked region (Fig. 3.7B, nbeads = 165, nsample= 4). Control stiffness measurements were conducted before crosslinking, but not necessarily in the same FOV. Inside the crosslinked region, κ was found to be higher than control stiffness in all directions, except along the short axis of the rectangle (0°, p = 0.71). Stiffness anisotropy in the crosslinked region was observed and κ probed along the long axis of the rectangle (90°) was significantly higher than κ probed along 0° (p <0.01, nbeads = 52). Outside of the crosslinked region, κ measured at 0° was significantly higher than both control stiffness (p = 0.02) and stiffness probed at 90° (p <0.01), but not different from κ probed at 0° inside the crosslinked region (p textgreater 0.99). Direction of the highest stiffness is visualized by arrows in Fig. 3.7C, indicating diverse anisotropies both inside and outside of the crosslinked region. While stiffness probed at 0° did not show distance-dependency, stiffness probed at 90° decreased with the distance away from the crosslinked region.

These findings are corroborated by image analysis of fiber architecture before and after crosslinking. Orientation distribution of fibers was measured by processing reflection confocal images in GTFiber software for automated analysis of fibrillar morphologies [100]. After crosslinking, the crosslinked region showed a bias towards 90° fiber orientation (Fig. 3.7D). Change in fiber alignment was not detected outside of the crosslinked region when considering that region as a whole, or binning it into regions located 0–50, 50–100, and 100–150 µm away from the crosslinked region (repeated measures ANOVA; p = 0.70). Pixel brightness increased notably inside the crosslinked region (Fig. 3.7E). An increase in pixel brightness was also observed outside of the crosslinked region, although to a lesser extent. Pixel brightness decreased significantly with distance away from the crosslinked region (Spearman's rank correlation coefficient, rs = -0.62, p <0.01). Fiber displacements outside of the crosslinked region were primarily towards the crosslinked region (Fig. 3.7F) and predominantly in

the horizontal direction. Similar to trends observed after crosslinking the circular region, maximum displacement of fibers was detected at the edge of the crosslinked rectangular region.

In order to establish more pronounced stiffness anisotropies, two 50 µm by 200 µm rectangles were crosslinked parallel to one another (Fig. 3.8A). Rectangles were separated by either 50 µm (defined as R50) or 100 µm (defined as R100). After each treatment, κ was significantly higher than control stiffness in all directions, both inside and outside of the crosslinked regions ($p < 0.01$, Table S2). Stiffness in crosslinked regions was comparable between R50 and R100 treatments (Fig. 3.8B, C), as is also true for the non-crosslinked regions. For both R50 and R100, stiffness anisotropy was biased towards 90° inside the crosslinked regions, but towards 0° between the crosslinked regions. Interestingly, stiffness measured along the 0° direction did not change with the horizontal coordinate of probed beads. This holds true within and between the crosslinked regions. This result is in agreement with that observed up to 110 µm away from a single crosslinked rectangle (Fig. 3.7B). However, κ within each crosslinked region was higher in the case of two crosslinked rectangles as compared to a single rectangle (with the exception of κ probed at 90°). Similarly, when comparing regions equidistant from a crosslinked rectangle and probed at 0°, R50 and R100 treatments resulted in higher stiffness between the crosslinked rectangles than stiffness measured in regions adjacent to a single crosslinked rectangle.

Fiber alignment after crosslinking either one or two rectangles was subtle and not evident without computational image analysis. Analysis in GTFiber software indicated that crosslinking two rectangles instead of one resulted in similar alignment inside the crosslinked region, but more prominent horizontal alignment outside of crosslinked regions (Fig. 3.8D). In all cases fiber alignment was biased towards the 90° orientation inside the crosslinked region and towards the 0° orientation outside of the crosslinked region. After both R50 and R100 treatments, pixel brightness was higher inside the crosslinked regions, than between them (Fig.

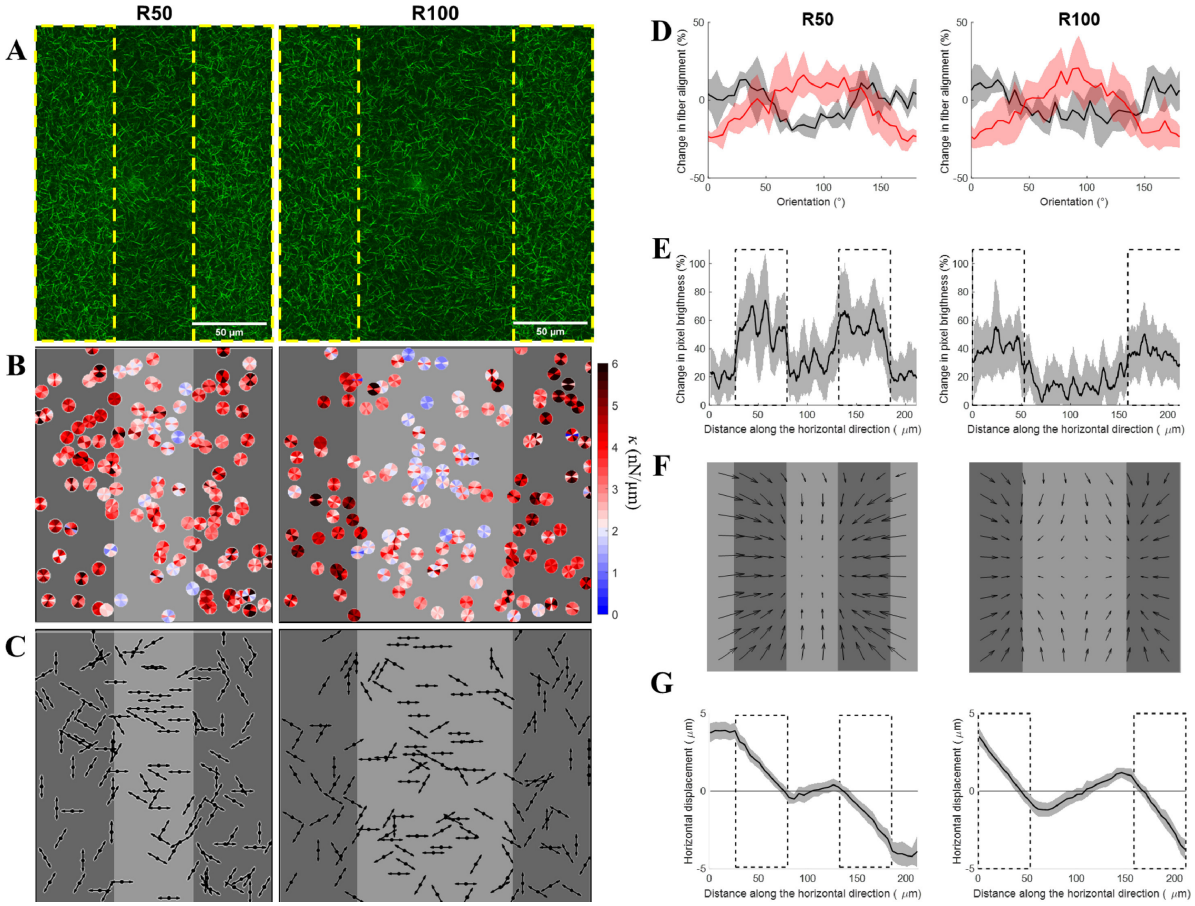

Figure 3.8: The effect of crosslinking two rectangular regions. (A) Reflection confocal images after crosslinking rectangles separated by 50 µm (R50) or 100 µm (R100) - marked by the yellow dashed lines. (B) Stiffness was probed in 6 directions using multi-axes AMR. Stiffness is color-coded separately for each direction of bead oscillation. Crosslinked region is marked by a dark gray background. (C) Direction of the highest stiffness is represented by arrows. (D) Fiber alignment within (red) and beyond (black) the crosslinked region. (E) Change in pixel brightness with distance from the crosslinked region (denoted by dashed rectangle). Median ± IQR. (F, G) Optical flow detects matrix deformation.

3.8E). Fiber displacement during crosslinking varied in time. During the first 50 crosslinking scans fibers moved towards the center of the crosslinked region. With further crosslinking, fiber displacement was observed towards the center of the region between the crosslinked rectangles (Fig. 3.8F, G).

Lastly, the effect of patterned photocrosslinking on direction of cell migration was evaluated in fibrin hydrogels containing MDA-MB-231 cells. MDA-MB-231 human breast cancer cells are known to respond to stiffness gradients in 2D and 3D cultures and were previously shown to display positive durotaxis [27, 3, 105]. Here, two 1000 × 50 µm rectangles spaced by 100 µm were crosslinked for 2000 scans using the 488 nm laser line of a Fluoview3000 microscope. Rectangles were oriented vertically with respect to the field of view (Fig. 3.9A). Unlike the Fluoview1200 system used for AMR measurements, the Fluoview3000 is equipped with a stage top incubator for multi-day studies. Cells were observed every hour for up to 100 h following crosslinking (ncells = 15, Fig. 3.9A). Control cells were imaged similarly (ncells = 25, Fig. 3.9A). Cells between the crosslinked regions were found to migrate at lower speeds than control cells ($p < 0.01$, Fig. 3.9B). Cells located centrally between the crosslinked regions were more likely to move in the horizontal direction (directional bias <0, Fig. 3.9C) than in the vertical direction. However, as cells moved closer to the crosslinked region, they exhibited a vertical directional bias (directional bias textgreater 0). Similarly, cells located in the central region exhibit horizontal-dominant direction of cell orientation (Fig. 3.9D) and cell migration (Fig. 3.9E). These trends transition to vertical near to the crosslinked rectangles. Forward migration indices (FMI) did not differ from 0 for control cells in either horizontal (FMI_X; $p = 0.72$, Fig. 3.9G) or vertical (FMI_Y;$p = 0.26$) direction. In contrast, cells between the crosslinked regions had higher FMI_X than control cells ($FMI_X = 0.23$, $p < 0.01$), while FMI_Y in the vertical direction ($FMI_Y = 0.12$) did not differ from control FMI_Y ($p = 0.29$).

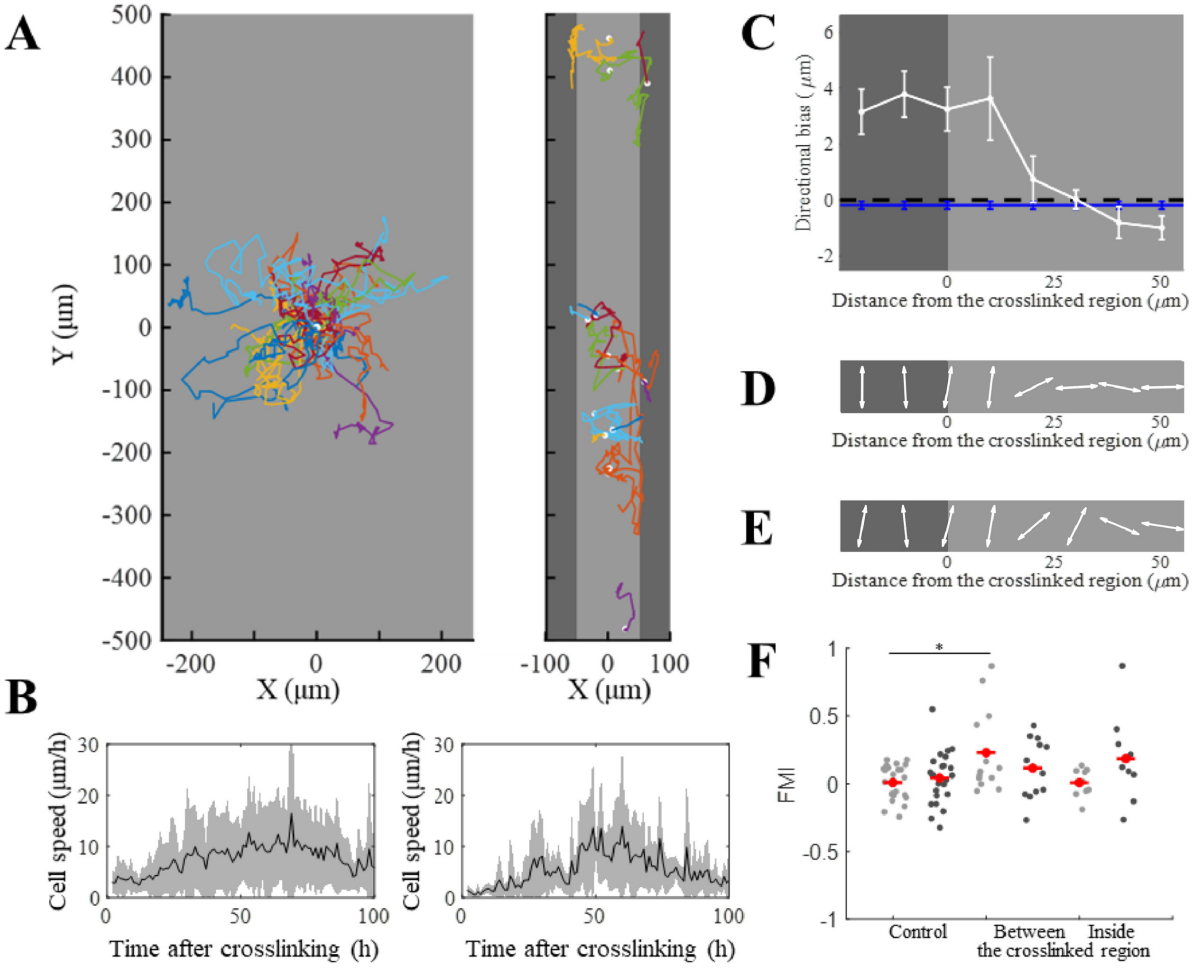

Figure 3.9: RCP induces changes in migratory behavior of MDA-MB-231 cells. (A) Trajectories of control cells (left) and cells between (right) the crosslinked rectangular regions (dark gray). (B) Change in average cell speed with time after crosslinking, calculated between every 1 h for control cells (left) and cells between the crosslinked regions (right). (C) Directional bias defined as a difference in absolute displacement in the vertical and horizontal direction for control cells (blue line) and cells between the crosslinked regions (white line). (D) Dominant cell orientation and (E) dominant direction of cell migration, represented with respect to the distance away from the crosslinked region and binned for every 10 µm (F) FMI index values for each cell in the direction perpendicular (light grey background) and parallel (dark grey background) to the crosslinked region. Mean FMI values are denoted by red markers; * denotes statistical significance.

3.5 Discussion from Jagiełło 2021

In this follow up study, multi-axes AMR allowed us to assay the stiffness anistropy within and surrounding crosslinked regions. Crosslinking a circular region resulted in radial stiffening towards the center of the crosslinked region. The pattern of high stiffness on the sides and lower above and below the crosslinked circular region that was seen with Keating *et al.* was indeed due to stiffness anisotropy which was maximum radially (Fig. 3.4, 3.6). Stiffness inside the crosslinked region was found to be isotropic and 2.1-fold higher than before crosslinking. Fold-increase in stiffness after RCP was comparable with the effect of magnetic alignment of fibers [122] and with other methods of creating stiffness gradients in natural hydrogels [19]. The method of optical flow analysis was used to calculate the displacement field within and surrounding crosslinked regions. The direction of greatest displacement corresponded to the axis of highest stiffness. Optical flow analysis of fiber displacement indicates that the circular crosslinked region approached maximal contraction by 500 scans. While additional fiber displacement within the crosslinked region was not detected beyond 500 crosslinking scans, displacement outside of the crosslinked region was still changing after 2000 scans. This trend is in contrast with stiffness measurements by AMR, which found no significant difference in stiffness after 500, 1000 and 2000 crosslinking scans. Given that the stiffness values are well within the limit of AMR measurement, we are likely observing a low-strain effect that does not significantly contribute to further strain hardening.

In an attempt to generate anistropy which in a single direction, rectangular regions were crosslinked. Unfortunatly the geometry of this crosslinked regions were limited by the AMR system which required high numerical aperture and magnitfication objective which limited the field of view. Rectangular crosslinking promoted stiffening and fiber alignment inside the crosslinked region biased along the long axis of the rectangle. Outside of the crosslinked region, the reverse bias was observed up to 110 µm away from the crosslinked rectangle, suggesting that the region is under tension and RCP may induce strain hardening. Interestingly, stiffness

measured in the horizontal direction (0°) did not change with probed bead location indicating lack of measurable spatial gradients. The lack of distance-dependent stiffness gradients probed at 0° is consistent with strain hardening where as seen in Figure 3.8G, the fiber displacement gradient along the horizontal axis is fairly constant throughout the region, indicating constant strain level. In contrast, stiffness gradients with respect to the horizontal axis of the image were detected when stiffness was measured along 60°, 90° and 120° direction. Optical flow analysis during crosslinking rectangles found that the derivative of horizontal displacement with horizontal position is positive in the non-crosslinked regions (Figs. 3.7G, 3.8G), indicating that the material is being stretched, which is consistent with the observed increase in stiffness following crosslinking, and suggestive of strain hardening in that region. Crosslinking two rectangles instead of one resulted in higher stiffness and a greater change in fiber alignment. Surprisingly, we found pixels in between the crosslinked regions to be brighter for R50 as compared to R100. Such differences in pixel brightness could be indicative of diffusion of the crosslinking radicals from the laser-scanned region. However, crosslinking results in a detectable autofluorescence (Ex: 561 nm, Em: 570–670 nm) and only fibers in the selected laser-scanned region had detectable signal, suggesting that chemical alterations were highly localized.

To produce the most locally uniform region in terms of stiffness anisotropy and fiber alignment, the crosslinking was done instead with a much lower magnification (10x compared to 60x) objective to achieve a larger field of view. With such a setup, MDA-MB-231 cells exhibited behavior consistent with contact guidance along a network of fibers aligned by micropatterned RCP. The cells favored horizontal migration between the crosslinked rectangles where fibers were biased towards the horizontal direction (Fig. 3.9C). As cells approached the crosslinked regions with fibers exhibiting more vertical orientation, they orientated themselves accordingly. Similarly, cell orientation was shown to correspond with the axis of the highest stiffness (Fig. 3.10). Our experiments show that not only were fibers aligned, but stiffness was anisotropic. In consideration of biophysical cues, it is possible that effects of contact guidance

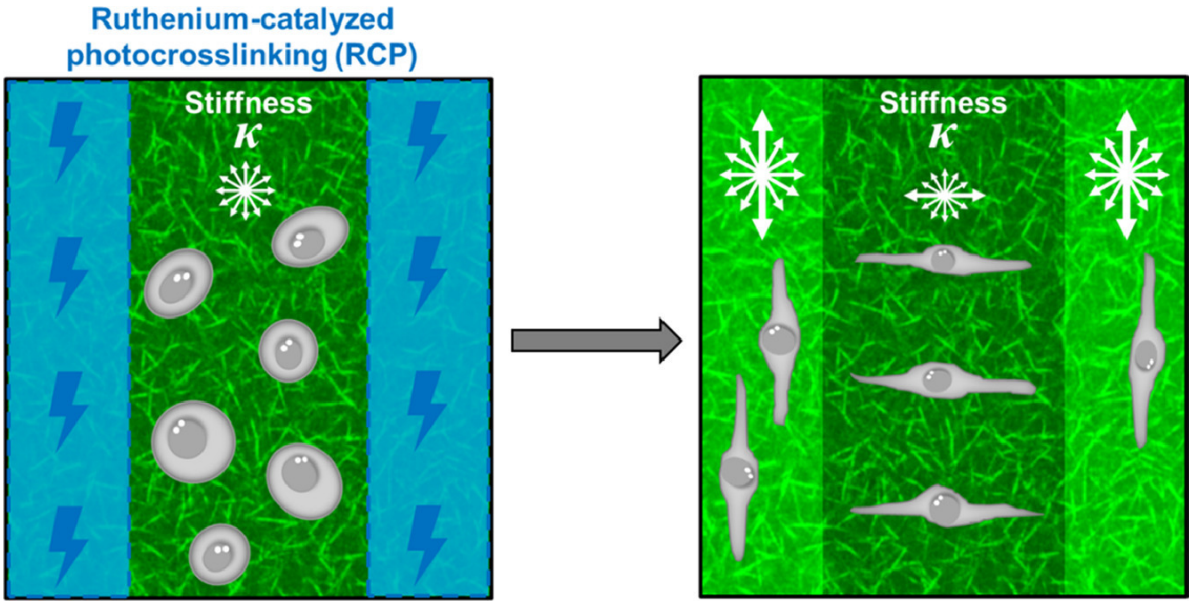

Figure 3.10: Summary of observed effect of crosslinking on stiffness anisotropy and cell behaviour.

were supplemented the stiffness anisotropy. Observed changes in migratory behavior and alignment of MDA-MB-231 cells indicate that the effect of RCP on fiber alignment and stiffness landscape is strong enough to promote directed cell migration. Moreover, unlike other existing methods, RCP can alter stiffness landscape and anisotropy around individual cells embedded inside 3D fibrous hydrogels and allows for observation of a single cell's response to changes in local ECM physical properties. While we were focused on creating fiber alignment and stiffness anisotropy to all be in the same direction around the cell for simpler analysis, RCP is not limited to this. Future studies can vary the extent and arrangment of stiffness anisotropy and fiber alignment by crosslinking duration, delivered light dose, photoinitiator concentration, and by modifying the geometry of the crosslinked region.

3.6 Materials and Methods

3.6.1 Fibrin gel

Fibrin hydrogels were prepared with 2.0 µm carboxylated silica microbeads (Bangs Laboratories) dispersed within the hydrogels prior to gelation. Bovine fibrinogen stock (Sigma) was dissolved in phosphate buffered saline (PBS, Gibco) and sterile filtered (0.22 µm, Olympus) before use. Gelation was conducted by mixing fibrinogen/microbead/PBS solution with bovine thrombin (Sigma), to achieve a 1 mL hydrogel with final concentrations of 2.5 mg/mL fibrin, 0.8% (w/v) microbeads, and 4 U/mL thrombin (Sigma). Hydrogels were cast into 35 mm glass bottom dishes (MatTek), resulting in a hydrogel approximately 500 µm thick at the center, where experiments were conducted. Hydrogels were kept in an incubator (37° C, 5% CO2) for 25 minutes after which they were hydrated with culture medium: 2 mL of DMEM (Gibco) + 10% FBS (Gibco) + 1% Penicillin-Streptomycin (Gibco). Fibrin hydrogels were then stored for 24 hours in the incubator before use. 25mM HEPES(Gibco) was added for hydrogels prepared for Jagiełło *et al.*

3.6.2 Photo-Crosslinking

200 µl of culture media was substituted with 200 µl of crosslinker solution prepared by mixing 1.5 mg/mL tris(2,20-bipyridyl) dichlororuthenium (II) hexahydrate (Sigma) and 2.4 mg/mL sodium persulfate (Sigma). Photocrosslinking was conducted at least 30 min after the addition of the crosslinker solution, but no later than 6 h. The region of interest (ROI) chosen for crosslinking was selected using built-in functionality of our Fluoview1200 inverted laser scanning confocal microscope (Olympus) into which the optical tweezers active microrheology optics are integrated. The photocrosslinking was induced by illumination of the selected ROI with the 488 nm laser line (0.1 mW) focused by a high numerical aperture microscope

objective lens (60x-oil PlanApo TIRFM 1.45NA, Olympus). A selected ROI was crosslinked at a height of 35 µm from the cover glass at a scanning speed of 2 µs/pixel and a total scan resolution of 1600 pixels x1600 pixels across the 211.2 µm by 211.2 µm field-of-view (FOV).

3.6.3 Imaging and image processing

Confocal reflection microscopy (CRM) was performed to assess structural differences within the fibrin mesh. Imaging was performed using the 559 nm laser line of the FV1200 operating at 0.72 mW. 559nm imaging was confirmed to not significantly cause crosslinking if the crosslinker solution is diluted in culture media as described. Image contrast was normalized before fiber alignment was measured using the GTFiber software [100]. An optical flow algorithm based on the Farneback method [31] was utilized to analyze successive frames of these images and capture deformation dynamics across the entire crosslinking process by summing deformations throughout the time series. Summed optical flow results were down sampled via bilinear interpolation by a factor of 80, resulting in nodes being spaced 10.6 µm apart. Additionally, fiber density was analyzed in the CRM images. Images were binarized using the Matlab built-in adaptive binarize function and objects smaller than 10 pixels were removed. Bright pixels were then counted in annular areas emanating from the center of the crosslinked region.

3.6.4 Active microrheology

Two different active microrheology systems were used for this study.

For the first system: AMR was conducted within the volume of the fibrin hydrogels. Our AMR instrument has been described previously [64, 53]. Briefly, probe beads within the hydrogel are oscillated via a 1064 nm laser trap, steered by oscillating galvanometer mirrors. The bead

acts as a lens to deflect a second, stationary laser beam (785 nm), which is focused onto a quadrant photodiode. The complex-valued material response (α^*) is calculated from the phase-amplitude relationship between trapping forces and probe bead displacement [87, 12]. Here we report $1/\alpha$', which is the inverse of the real component of α^* and can be considered a metric of stiffness. Beads were probed at 50 Hz and were located approximately 35 µm from the bottom cover glass. Potential effects of cover glass proximity on measurements were controlled by performing all measurements for different treatments at the same approximate height.

For the second system: Stiffness was measured using our optical tweezers active microrheology system. Stiffness of the ECM is probed by oscillating individual microbeads using optical forces applied by a continuous-wave fiber laser with an emission at 1064 nm (YLR-5–1064-LP, IPG Photonics). Trapping beam oscillations are caused by the movement of a pair of galvanometer mirrors (GVS012, ThorLabs), located conjugate to the back focal plane of the microscope objective lens (60x-oil PlanApo TIRFM 1.45NA, Olympus). A detection laser beam of wavelength 785 nm is generated by a single mode fiber-pigtailed laser diode (LP785-SF100, ThorLabs) and co-aligned with the trapping beam at the center of the bead. Change in bead position and trapping beam position are recorded by two quadrant photodiodes (detQPD and trapQPD, 2901 and 2903, respectively, Newport) and used to calculate a complex material response (α^*) by the relationship X= α^*F, where X and F are the Fourier components of bead displacement and optical force, respectively. α^* is computed once for each oscillation direction under the assumption that α^* oscillates purely along that axis. Reported stiffness κ represents the real component of inverse α^*. Each probed bead was located approximately 35 µm from the cover glass and oscillated along 6 different directions (0, 30, 60, 90, 120 and 150° with respect to the horizontal axis of the camera image FOV). The trapping beam was oscillated with an amplitude of 60 nm and frequency of 50 Hz, unless specified otherwise. The proportionality parameter relating detQPD signals to bead displacements was measured in situ per bead and per angle of oscillation. Specifically, the

sample is mounted in a stage-top nanopositioning piezoelectric stage (P-545.xR8S PInano® XYPiezoSystem,PI). After centering the stage on each bead, the stage is moved 200 nm across the bead with a constant velocity of 100 nm/s. Recorded detQPD voltages are used to quantify the voltage-to-µm conversion factor which is later used to calculate bead displacement during AMR measurements. Prior to AMR measurements in fibrin hydrogels, the AMR system is calibrated in water.

3.6.5 Cell culture

Normal human dermal fibroblasts (NHDF, Lonza) were cultured in culture medium (described above) in an incubator (37° C, 5% CO2). 2.5 mg/mL fibrinogen with 150K/mL NHDF cells in PBS and 4 U/mL thrombin were cast in 35 mm glass bottom dishes and hydrated with culture medium. After 24 hours incubation, crosslinking solution was added and crosslinked via 1000 scans of the 488 nm laser in a 100µm diameter circular region of interest. The crosslinking solution was washed out with 3 washes of culture medium and then fibrin hydrogels were placed back into the incubator for 4 hours. "No crosslinker controls" received the same treatment (including the washout) as the crosslinked samples except 200 µL PBS was added rather than crosslinker solution. Live (positive) controls were not treated. Finally, dead (negative) controls were treated with 70% ethanol to verify ethidium homodimer stain was detectable in dead cells. Medium was aspirated and replaced with 2 µM Calcein-AM (Invitrogen) and 4 µM ethidium homodimers (Invitrogen) in PBS. Cells were placed back into the incubator for 10 minutes before being imaged in Fluoview with a 10X 0.3 NA air objective. Calcein-AM was excited with 488 nm laser and 505–540 nm emission was collected. Ethidium homodimer was excited with 559 nm laser and 655–755 nm emission was collected. 5 by 5 tiled images were taken for all assays with Fluoview multiarea controller and tiled with ImageJ.

Highly invasive and triple-negative human breast cancer cells, MDA-MB-231 (ATCC), were cultured in Dulbecco's Modified Eagle's Medium (DMEM) with low glucose, L-glutamate, and sodium pyruvate (Gibco) supplemented with 10% Fetal Bovine Serum (FBS, Gibco) and 1% penicillin streptomycin (Gibco).

The effect of micropatterned photocrosslinking on migration and orientation of MDA-MB-231 cells was assessed using a Fluoview3000 laser scanning microscope equipped with a 10x-air 0.3 NA microscope objective lens (Olympus). Hydrogels were incubated in a ThermoBox environmental chamber (Tokai Hit) and a stage top incubator (Tokai Hit) with 15% oxygen and 5% CO2. Photocrosslinking was initiated at least 30 min after the addition of the crosslinking solution to allow for diffusion of the crosslinker solution evenly throughout the hydrogel. Two 1000 µm by 50 µm rectangles separated by 100 µm were selected using built-in functionality of the Fluoview3000 system and crosslinked for 2000 scans using the 488 nm laser line (0.1 mW). A selected ROI was crosslinked 100 µm from the cover glass at a scanning speed of 2 µs/pixel and a total scan resolution of 4096 pixels x 4096 pixels across a 1088 $\times$ 1088 µm FOV. Crosslinking settings were chosen to match the total light energy used in cell-free studies and the Fluoview1200 microscope. Importantly, net fiber displacement as measured by optical flow was shown to be similar in cell and cell-free studies.

Afterwards, the crosslinking solution was washed out three times with fresh media. The fibrin hydrogels were incubated at 37 °C and 5% CO2 for at least 15 min between the washes to allow for crosslinker diffusion. Next, hydrogels were hydrated with fresh media and returned to the stage top incubator for imaging. Cells between the crosslinked rectangles, and control cells at least 2 mm away from any crosslinked region were then imaged every hour for up to 100 h using the Fluoview3000 with a 4x-air 0.16NA objective lens (Olympus). Cell viability after crosslinking a single 1000 µm by 50 µm rectangle was confirmed with live-dead staining.

Analysis of cell migration was conducted by first hand-tracing cells in each FOV using Fiji. Afterwards, cell directional bias, cell speed, orientation and direction of cell migration were

quantified using a custom MATLAB script. Forward migration index (FMI) was calculated in MATLAB as the average of the ratio of cell displacement in either horizontal (FMI_X) or vertical (FMI_Y) direction to total distance traveled by each cell.

To describe the average orientation of cell migration and alignment, the nematic order parameter and principle orientation were calculated for these vectors. The principal orientation direction (director) is calculated as the direction of the principal eigenvector of the mean of the orientation tensors, where the orientation tensor is calculated as the tensor product of a vector with itself. The maximum eigenvalue is rescaled between 0 and 1 and reported as the orientation order parameter (OOP). The director is a measure of the average orientation while OOP describes how well the set of orientations aligns to the director, with 1 meaning a perfect alignment and 0 meaning random orientation.

3.6.6 Statistical Analysis

For Keating 2019: Statistical analysis was conducted in Origin Pro. Sample sets were tested using non-parametric statistical methods. Mann-Whitney U-tests ($\alpha = 0.05$) with a Bonferroni correction was conducted for all statistical comparisons presented in this paper. Data in the manuscript are presented as mean ± standard deviation.

For Jagiełło 2021:Non-parametric statistical analyses at a significance level of 0.05 were conducted to compare non-normally distributed stiffness values ($p < 0.01$, Kolmogorov-Smirnov test). The Friedman test was used to compare stiffness measurements between each oscillation axes. The Kruskal–Wallis test was performed for comparison of multiple groups. The post-hoc Tukey–Kramer test was used to compare specific groups. Distance-dependance of stiffness was described using Spearman's rank correlation coefficient, while change in fiber alignment with distance was compared using ANOVA. The Pearson correlation coefficient was used to quantify the correlation between stiffness and frequency or amplitude of bead

oscillation and to assess the time-dependency of cell migration speed. FMI values were compared using Student's t test. All statistical tests were performed in MATLAB.

a

Chapter 4

Simulation of force transmission through fibrin hydrogels at the fiber network scale

4.1 Background

Simple models of complex systems can often be very useful. The mechanical response of fibrous biological material work is a well studied topic [83, 119]. At the macroscopic scale, continuum models of varying complexity can be used to capture the material response of each materials. Additional parameters such as fiber anisotropy are often necessary to explain the long range force transmission that is observed [119, 2, 17, 81, 118]. However, at the scale of the fibers the material is clear not continuous as shown in figure 2.3. To account for the effect of discrete fibers, discrete network models are often used where fibers linked together at nodes is a typical method of representing fibrous materials [119, 2, 17, 95]. When forced are applied to a discrete network, the transmission occurs through a sub set of the fibers

which is dependent on the arrangement of the fibers. The use of regular lattice network allows for reproducible and symmetrical response. Triangular lattices are simple but the connectivity at each node is poorly representative of biological fibrous materials. Partially disconnected triangular lattices, hexagons, Kagome, Delaunay, or Voronoi lattices can be used instead to achieve the correct connectivity. Random network can be generated with properties such as fiber density, connectivity, fiber length, connectivity per node chosen directly or indirectly to match experimental observations. Using generated networks allows for easier set up of simulation, as the size and number of initial states is arbitrary while introducing local heterogeneity. Random isotropic discrete models show that when strained, the fibers are align and stiffen [126, 1]. Discrete network models can naturally capture nonaffine deformations of fibrous materials, which create additional heterogeneity at the fiber scale. These behaviors can also be parameterized to a certain extent into continuum models when looking at larger length scales [102, 126]. Choosing how to represent the fiber network is important in producing a useful model.

Beside the network, individual fiber properties also have to be modelled. In the simplest mode, we have fibers represented by elastic beams which are linked together at nodes with free rotation. The elastic beams can be views as linear springs. more computation intensive approach can be to model the fibers as semi-flexible [39], worm like chains [5], or using FEM [81]. Some models create a fiber network within a FEM model [95]. However, solving for these models can be difficult and require the additional of very soft elements which minimally interact with forces but are required to provide a solution. Many of suggested that a model where the fibers quickly buckle under compress is more representative of materials like fibrin [95]. It is possible to take constitutive models and prescribe it the anistropic and nonlinear behaviours observed in experiment [102, 126]. But what I want to do here is to see how these properties can emerge from a simple model not designed to generate these behaviours. Existing models range from simple all the way to much more complicated mesoscale or atomistic modelling [34, 5, 133, 11]. Direct measurements of fibrin fibers responding to

pulling are also available from studies using atomic force microscopy [133, 23, 42]. Fibrin fibers can stretch 200% and has two distinct modes of stretching. This is attributed to the unfolding of different protein domains within fibrin monomers [133]. Fiber to fiber variability exist but is difficult to quantify [42]. It is also difficult to measure how much a fiber has already stretched from it's initial length. It is my intention to create a simple model which can have additional complexity added to it as experimental capabilities improve.

Here, we use a simple model with room for additional complexity to observe how changing parameters of the model would affect the characteristics of the fiber network model. This model sets the ground work for designing future experimental and computation work in a feasible manner. On the experimental side, it is important to consider both what is physically possible to observe and manipulate as well as the tools and funding that are accessible. On the computational side, models have to be small and simple enough to be run within reasonable time given the computational available to us but still capture enough of reality to offer some further insight.

I chose to model the fibers as linear springs connected at nodes where 3 or more fibers come together. The nodes are treated as freely rotating. The cross-sectional area of each fiber is assumed to be uniform through out the network and the elastic modulus of the material is assumed to be uniform in all fibers. This means that the spring constant of the fibers is proportional to the inverse of the length of the fiber. The approach I chose for finding the equilibrium position of the model is by calculating the net applied force on each node and shifting the position of the nodes in the network until the net applied forces are minimized.

	0.001	0.005	0.01	0.05	0.1	0.5
x	0.3535	0.3535	0.3535	0.3538	0.3546	0.3914
y	0.3535	0.3535	0.3535	0.3538	0.3546	0.3914
z	9.985	9.667	8.870	4.267	2.764	1.081

Table 4.1: Displacement per force unit (compliance) shows anisotropy as well as stiffening behaviour in z and softening behaviour in x and y directions.

4.2 Toy model example

For a simple system where a node is linked stationary points, the geometry of these fibers affects the response of node to applied forces. In the example shown in figure 4.1, the 4 fibers are symmetrically arranged in the x-y plane (Fig. 4.1A). The result is that pulling in the x or y axis results in in the same magnitude of displacement (Fig. 4.1B,C, Table 4.1). The displacement of the node is much larger when pulled in the z direction as there are no component of the fibers orientated in the z direction, until the node is displayed (Fig. 4.1D,Table 4.1). Interesting in this system, pulling harder on x or y results in a displayed network that is now easier to pull on while pulling in z results in a network that is harder to pull on showing both strain softening and strain hardening behaviour (Table 4.1, Fig. 4.1E). The metric being visualized is displacement per force which I will refer to as compliance. These results demonstrates anisotropy in compliance that is also dependent on the magnitude of the applied forces. The compliance normalized to the minimal applied force simulated is graphed to visual the stiffening and softening behaviour.

In this system, while pulling along the axes in this toy model results in response along the same direction, pulling in most other directions result in a displacement vector that does not point in the same direction of the force vector (Fig. 4.1 F). In this specific case pulling equally along the x and z axis with 0.5 unit of force, the direction of the force and displacement vectors differed by 15.3°. Investigating the displacement direction shift is much easier to do in simulation compared to experimentally, we can probe the response of the system in random directions and look at the aggregated results (Fig. 4.2). A random arrow of force

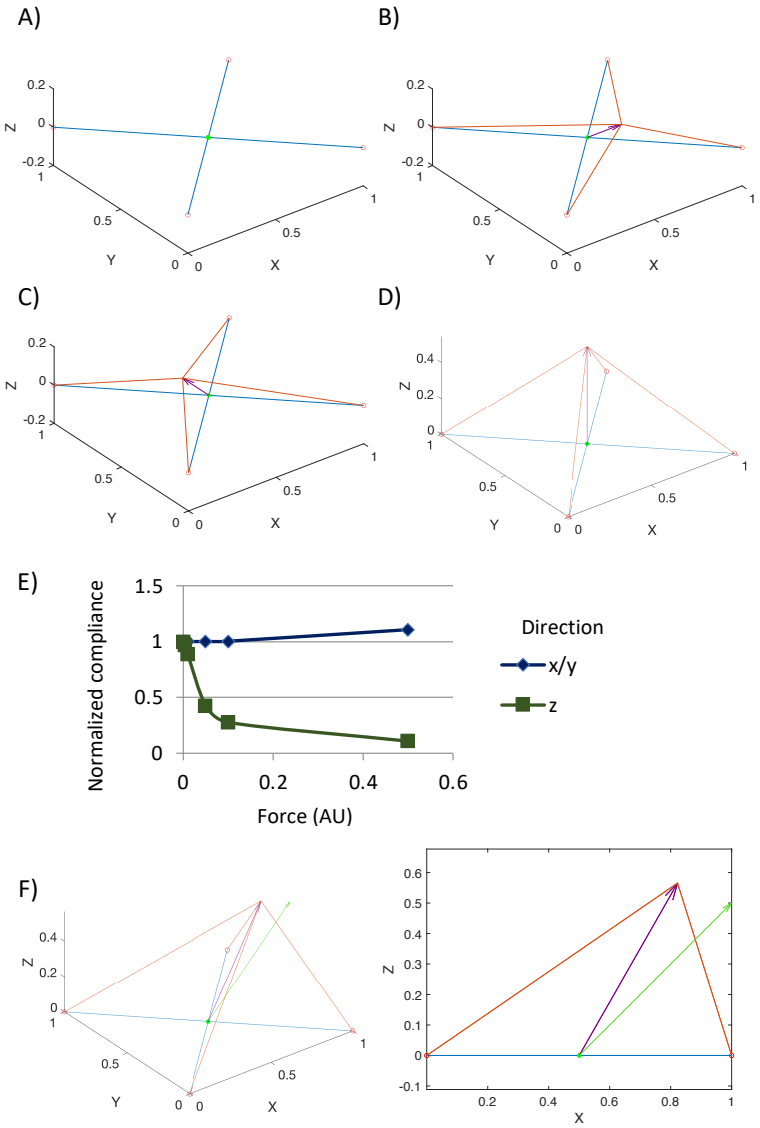

Figure 4.1: Simple toy model showing a node connected by 4 fibers responding to applied forces. A) The initial arrangement of fibers and nodes. The 4 nodes (red) are stationary while the node in the center (green) can move and is where the force is applied. Displacement of the node to 0.5 units of forces applied in the x (B), y (C), and z (D) directions with purple arrow indicating displacement.The blue lines indicate the initial arrangement of the network and the orange lines represent the network after the force is applied. E) Normalized displacement per force (compliance) for the system in response to in-plane (x,y) or out-of-plane (z) force visualized in the graph. Displacements can be found in table 4.1. F) The node is pulled equally by 0.5 units of force in the x and z direction at the same time. Force direction is shown in green while the displacement vector shown in purple. The same plot is displayed at 2 different angles to help convey three dimensional information.

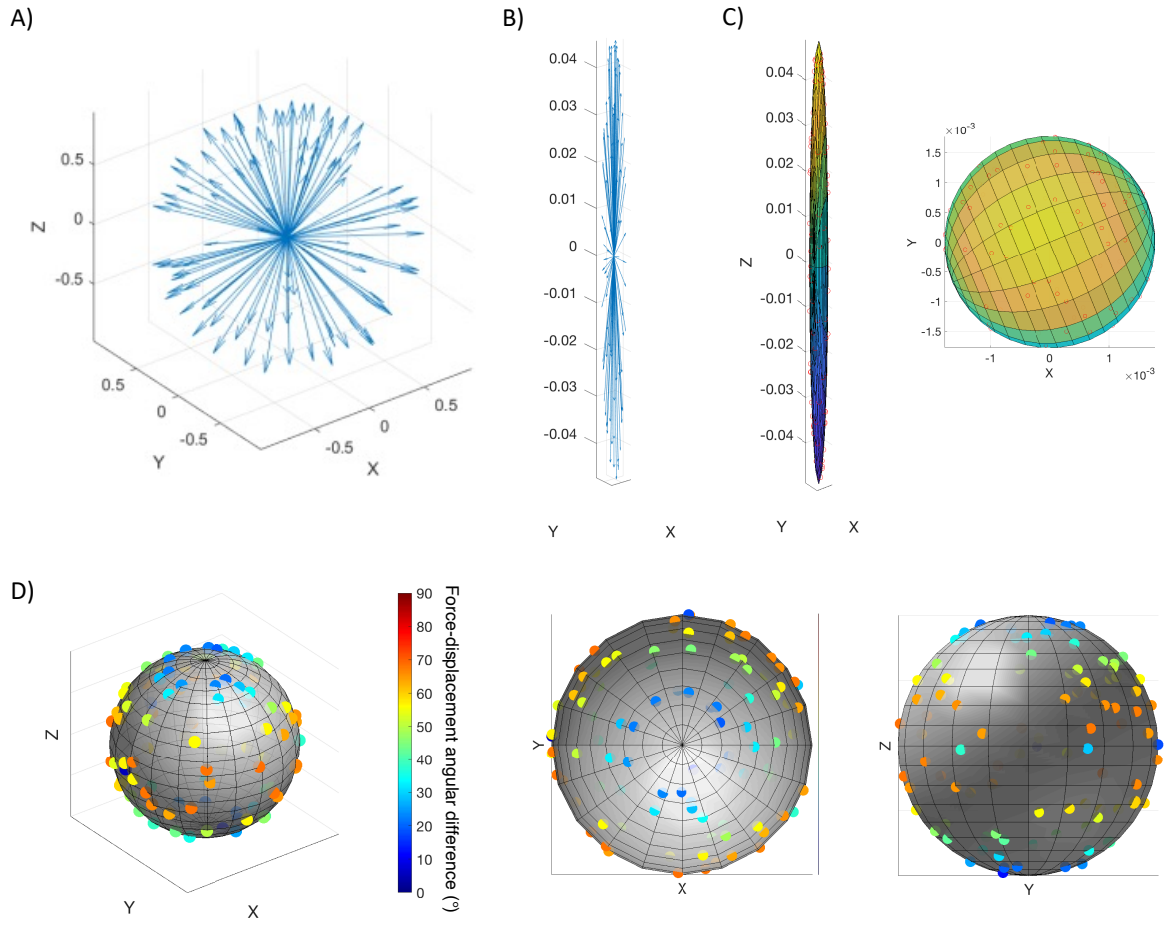

Figure 4.2: Simple toy model is probed by 0.005 unit of applied force in all directions to observe responding displacements. A) The 100 random force directions used to probe the response of the node. B) Displacements of the node in response to the force vectors are plotted as arrows. Each arrow corresponds to a force arrow in (A). The axis are equally scaled to allow for the anisotropy to become visually apparent. C) Fitted ellipsoid to the node displacement in response. The axis are equal to allow for the anisotropy to be visually apparent. Red circles are the displacements to which the ellipsoid is fitted to. 2 views of the same plot is provided. D) 3D scatter plot on unit sphere showing force-displacement angular difference. The nodes represent the direction of the force on a unit sphere. The color represents the angular difference between the force and displacement vectors. 3 views of the same plot is provided.

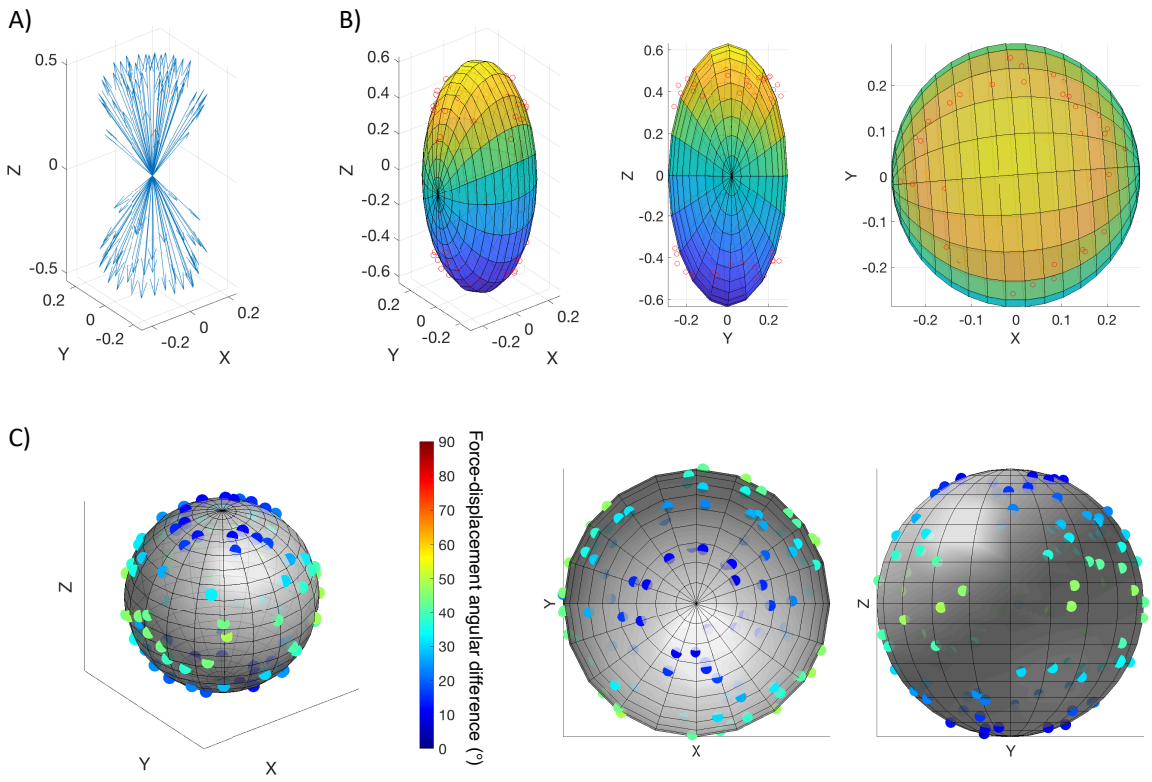

Figure 4.3: Simple toy model is probed by 0.5 unit of applied force in all directions to observe responding displacements. A) Displacements of the node in response to the force vectors are plotted as arrows. Each arrow corresponds to a force arrow in figure 4.2 A. The axis are equally scaled to allow for the anisotropy to become visually apparent. B) Fitted ellipsoid to the node displacement in response. The axis are equal to allow for the anisotropy to be visually apparent. Red circles are the displacements to which the ellipsoid is fitted to. 2 views of the same plot is provided. C) 3D scatter plot on unit sphere showing force-displacement angular difference. The nodes represent the direction of the force on a unit sphere. The color represents the angular difference between the force and displacement vectors. 3 views of the same plot is provided.

directions are generated to probe the system [59]. The seed for this random arrangement is set so that all instances are identical in this dissertation to ensure results are repeatable (Fig. 4.2 A). The resulting displacement from each randomly chosen uniformed distributed equal magnitude force vectors applied to the node is visualized for 0.005 unit (Fig. 4.2 B) and 0.5 unit (Fig. 4.3 A) of force. To make it easier to understand, we can visualize the anisotropy and force-displacement angular difference separately. The displacement can be fitted to an ellipsoid which can be described by its 3 radii parameters, [x = 0.0018, y = 0.0018, z = 0.048] for force = 0.005 and [x = 0.28, y = 0.28, z = 0.63] for force = 0.5 (Fig. 4.2 C, 4.3 B). The compliance of the system is [x = 0.35, y = 0.35, z = 9.8] for force = 0.005 and [x = 0.56, y = 0.56, z = 1.3] for force = 0.5, which is consistent with the trend of strain hardening and softening seen in figure 4.1 E. The ellipsoid fit is much better for smaller applied forces. In this toy model, the difference between the x-y and z axes is more apparently with smaller applied forces. The ellipsoid fit function was written by Yury Petrov [101]. The force-displacement angular difference can be plotted on the surface of a unit sphere. A dot is plotted on a unit sphere representing the direction of the applied force and the color of the dot represents the difference in angle between the force and displacement. We can see that forces on the x-y plane or close to the z axis shows small difference angle while force close to x-y plane shows the largest differences (Fig. 4.2 D, 4.3 C). Smaller applied forces which show greater anisotropy by the ellipsoid fit as well as greater angular difference. The displacement vector anisotropy and force-displacement angle difference is strongly dependent on the magnitude of the applied force.

If the whole system is stretched, akin to magnetically aligned or strain aligned systems [122, 46], the links now have a y alignment preference over x (Fig. 4.4 A). We see that stretching the system in y did not affect response in z but the system is more stiff in the y direction and less stiff in the x direction. For response to 0.005 unit of force, the ellipsoid radii parameters are [x = 0.0035, y = 0.0012, z = 0.048] as compared to [x = 0.0018, y = 0.0018, z = 0.048] in the unstretched system (Fig. 4.4 B). For response to 0.5 unit of

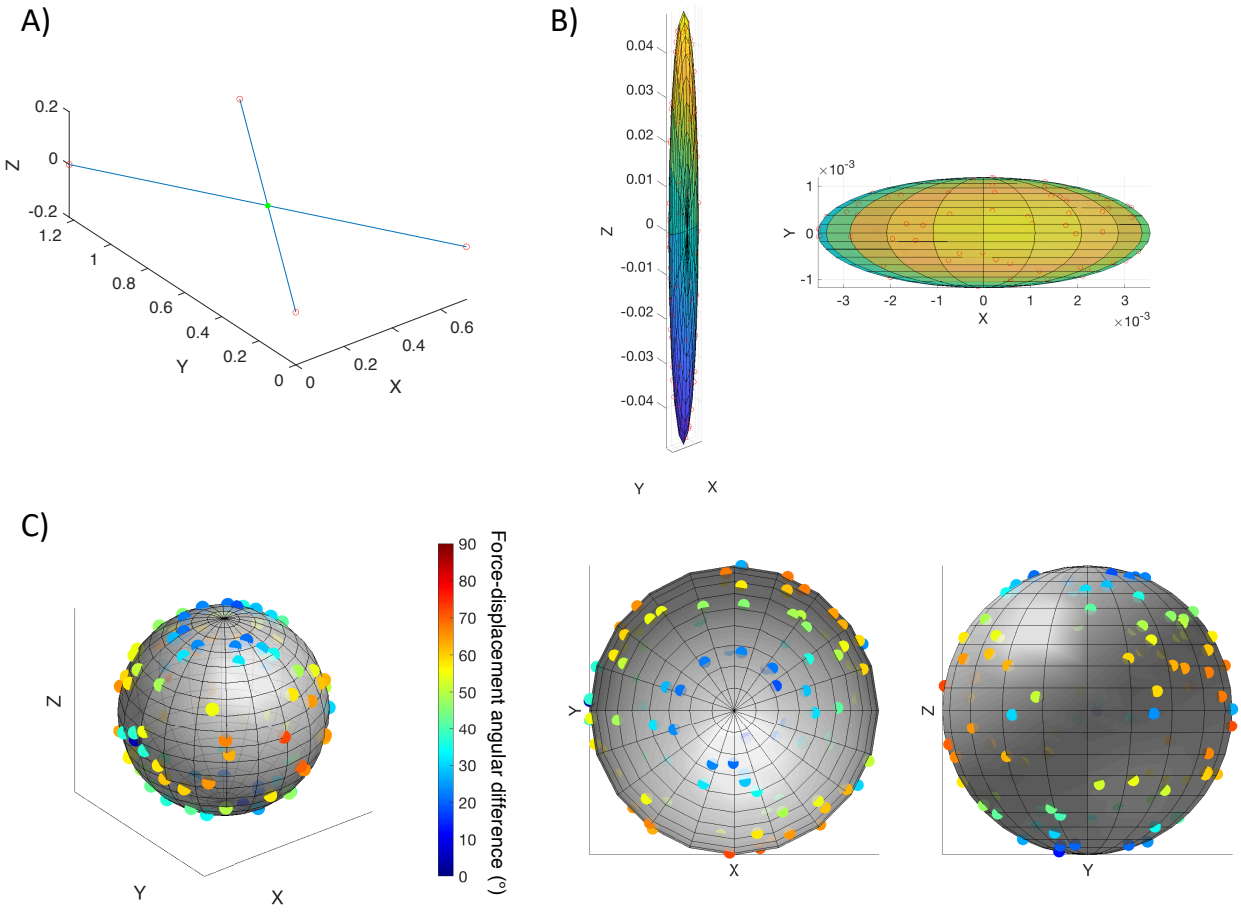

Figure 4.4: Stretched simple toy model responds to 0.005 unit of applied force with less displacement along the axis of stretch. A) The system has been stretched by 50% along the y direction. B) Fitted ellipsoid showing displacement in response to applied force. 2 views of the same plot is provided. C) The force-displacement direction difference. The nodes represent the direction of the force on a unit sphere. The color represents the angular difference between the force and displacement vectors. 3 views of the same plot is provided.

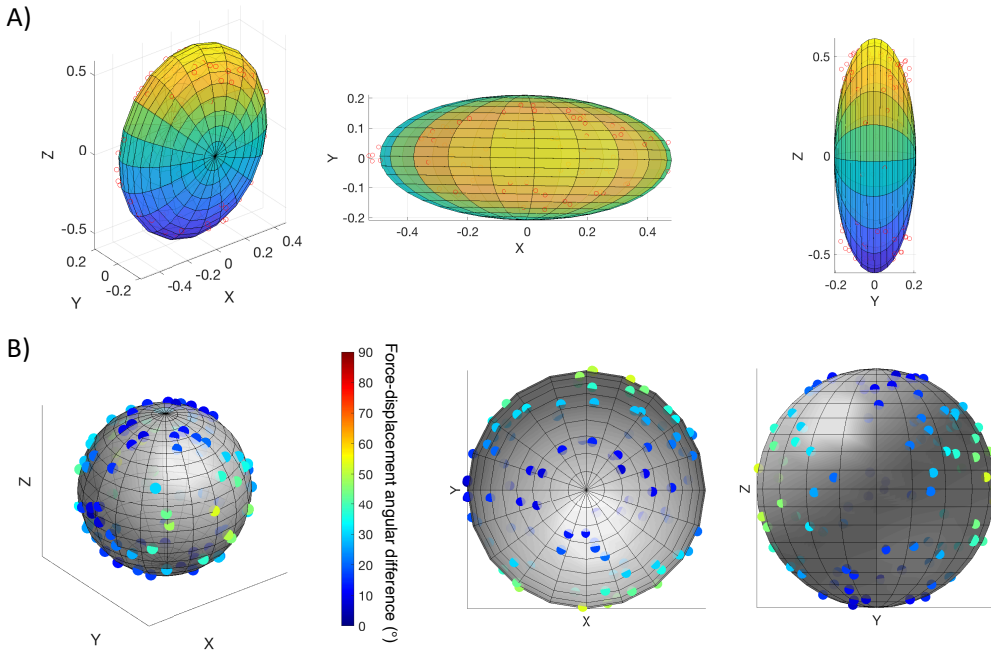

Figure 4.5: Stretched simple toy model responds to 0.5 unit of applied force. A) Fitted ellipsoid showing displacement in response to applied force. B) The force-displacement direction difference. The nodes represent the direction of the force on a unit sphere. The color represents the angular difference between the force and displacement vectors.

force, the ellipsoid radii parameters are [x = 0.48, y = 0.21, z = 0.63] as compared to [x = 0.28, y = 0.28, z = 0.63] in the unstretched system (Fig. 4.5 A). Angular difference between the force and displacement vectors also decreased for forces applied along the y direction (Fig. 4.4 C,4.5 B). As with the original system, the response greatly differs depending on how much force is applied. Force-displacement angle difference shows less difference in the y direction, especially for 0.5 unit of force. With stretching along the y direction, stiffness was increased along the y direction, decreased along the x direction, and remained the same in the z direction. This is expected as fibers are more aligned in the y direction, less aligned to the x direction and alignment in the z direction was unchanged.

4.3 Model from confocal image stacks

Networks with few fibers that are all in plane is not common unless we are working in experimental systems with troughs [42]. In 3D hydrogels there are fibers orientated in all directions [41]. Reflection confocal microscopy is better at identifying fibers which are horizontally orientated and thus gives the impression that the fibers are generally orientated in the imaging plane, however by fluorescently labelling the fibers all fibers become visible [41, 54, 47, 64]. 3D stacks of fluorescently labelled fibrin were used to generate graph and node representation of the fiber networks (Fig. 4.6). 3D confocal stacks were skeletonized and turned into nodes and connection using the skeleton3D and Skel2graph3D tools on Mathworks [62]. Interestingly, the orientation of the links in 3D was very close to isotropic. It is important to take note that node locations are accurate to 1 pixel length at best due to skeletonization method. Visual comparison of the confocal images to the final node network shows satisfactory results. Difficulty in processing non-fiber elements such as clumps,embedded beads, or cells remain an unsolved challenge.

A 10um by 10um by 10um subset of the image stack was used to generate a small network for the following simulation (Fig. 4.7). Nodes that were close to the edge (0.5 µm) were held stationary. The node that the force is applied to is no longer the only node that is free to move around so the whole network shifts in response to the applied force (Fig. 4.7 B). I will refer to this node to which the force is applied as the target node. In this example, the target node, denoted in green in figure 4.7 A, is connected by 4 links which are not in the same plane. The displacement of the target node and the nearby nodes from 0.0002 magnitude force is clearly visible when plotted (Fig. 4.7 B,C). Unlike the simple toy model case, the response at this node is not extremely, anisotropic as force and displacement is spread over a large region of the network rather than immediate to the target node. This system is anisotropic and the eigenvectors of the ellipse do not align to the primary axes (Fig. 4.7 D,F). The force-displacement angular difference is largest near the least compliant axis of

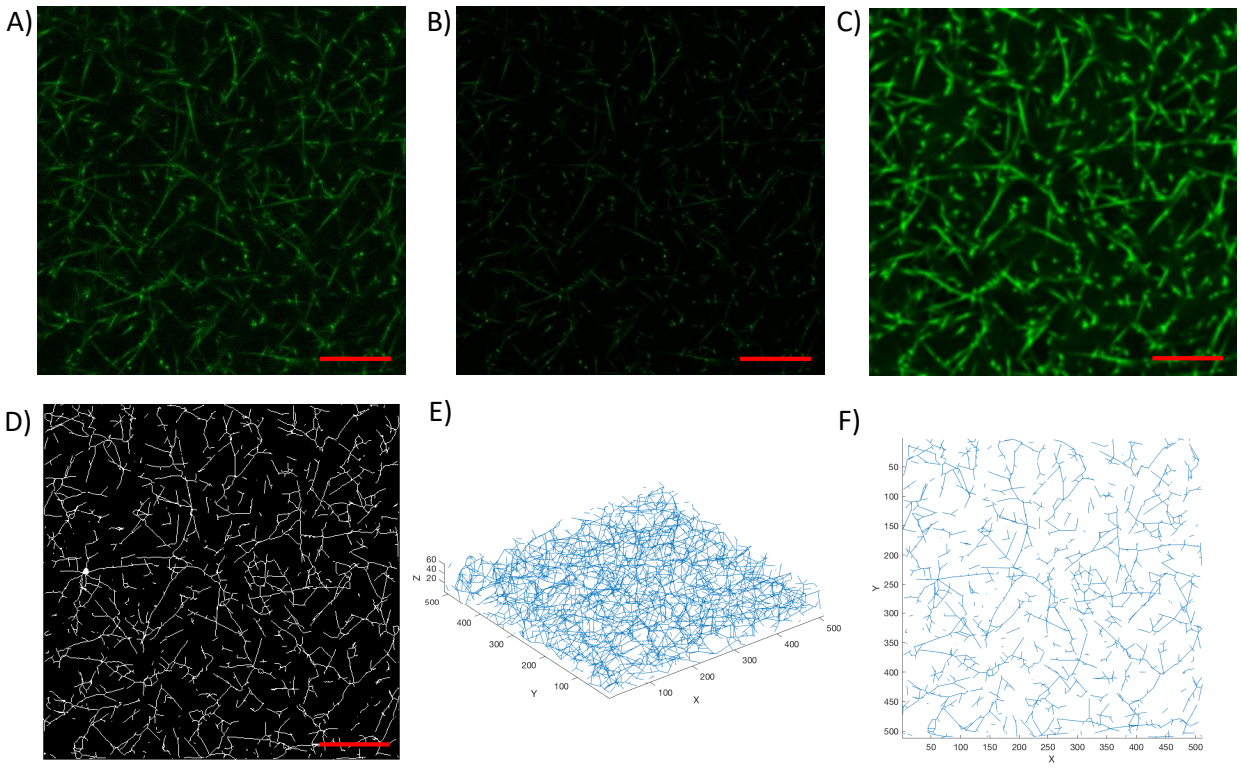

Figure 4.6: Skeletonization and graph generation workflow. Scale bar in red indicates 10µm. A) Single image from a z stack taken of fluorescently labelled 1.5mg/mL fibrin hydrogel. B) The same image after deconvolution is applied. C) The same image after deconvolution is normalized using ImageJ. D) The image stack is skeletonized using Skeleton3D. Only 10µm above and below the imaging plane is displayed. E) Graph-node network generated using Skel2Graph. Only 30µm above and below the image plane is displayed. F) Graph-node network x-y view. Only 10µm above and below the imaging plane is displayed. Axes are in units of pixels which are 0.1µm per pixel.

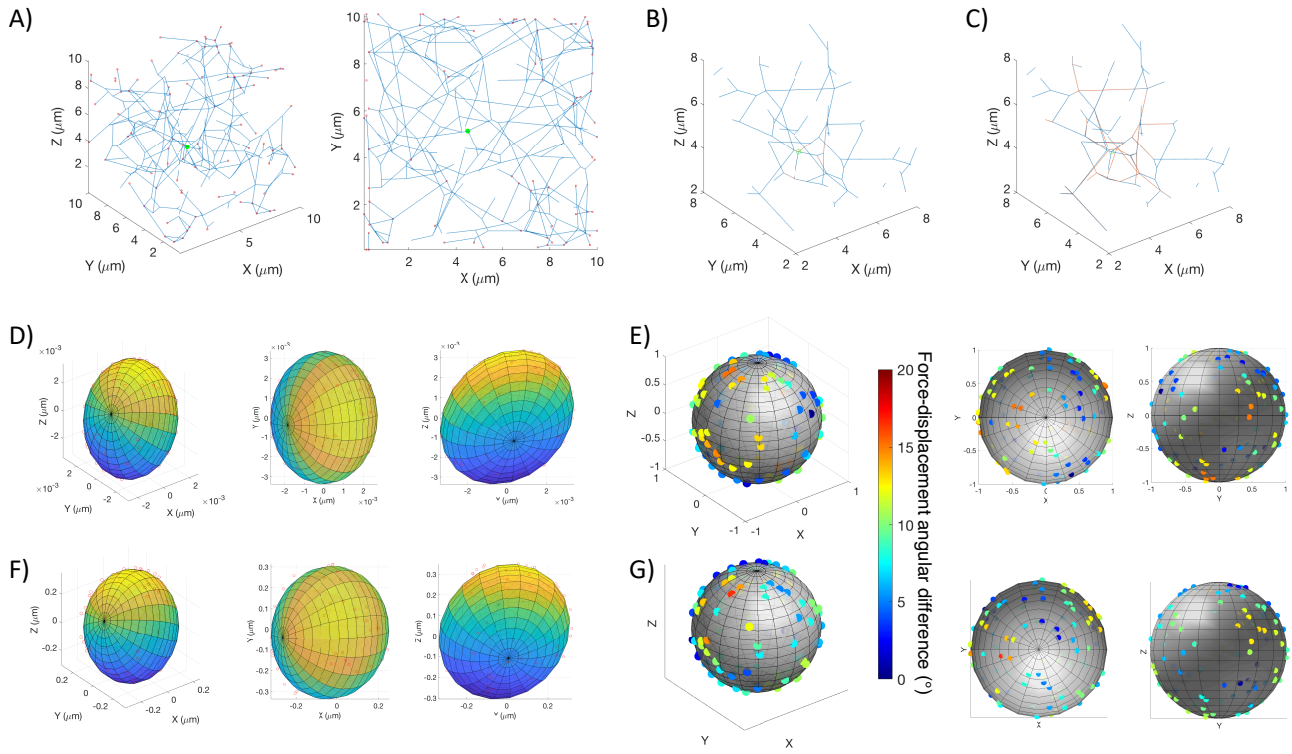

Figure 4.7: A subset of the skeletonized network is used for simulations. Forces are applied to a single node within a 10µm by 10µm by 10µm region of fibrin fiber derived network. A) Subset of the network with links shown in blue. Edge nodes (red) are held stationary while force is applied node in the middle (green). Two views of the same network is provided. B) Zoomed in view of the displacement of the network in response to 0.005 or C) 0.5 unit of force. The blue denotes the original network while the orange denotes the displayed network. Where the blue and orange networks overlap, only the blue is shown. D) Ellipsoid fit for displacement in response to 0.005 unit of force. 3 views of the sample plot are provided. E) force-displacement angular distance plot in response to 0.005 unit of force. 3 views of the sample plot are provided. F) Ellipsoid fit for displacement in response to 0.5 unit of force. 3 views of the sample plot are provided. G) force-displacement angular distance plot in response to 0.5 unit of force. 3 views of the sample plot are provided.

the ellipsoid fit. Note the change in scale of the force-displacement angular difference plot compared to figure 4.2-4.5. The difference between the force-displacement directions would be a very interesting hypothesis the explore using a modified AMR system [72]. Next, the simulations will be compared to some of the experimental observations made in chapter 2 and 3.

4.4 Displacements of nodes nearby the target node

When force is applied to a target node, the links pull on the surrounding nodes and ends up displacing them as well. This was experimentally observed in chapter 2, especially illustrated in figures 2.3 and 2.7 [41]. To compare this simulation to chapter 2, forces in different directions where applied in the x-y plane (Fig. 4.8A). Depending on which direction force is applied to the node in the center, nearby nodes will displace by differing amounts and in different directions. Pixel fluctuations was only a surrogate for displacement of the fibers due to the active oscillation of the trapped bead but the displacement of each node is known in simulation. First, it is important to note that even though the force applied to the target node here is in the x-y plane, the displacement of the nodes, especially the surrounding nodes is not limited to the x-y plane. For simplifying the visualization and interpretation, the visualization of the results will usually ignore the z axis. However, the displacement values reported in all the plots do include the z component of displacement. When the nodes are plotted with their positions relative to the node where force is applied, it is noticeable that beads closer to the center node generally have larger displacement (Fig. 4.8 C,D). Unlike the experimental data, it is not easily visually apparent that displacement of nodes along the direction of applied forces is higher (Fig. 4.8 C,D, 2.3). Even when we visualized that difference in node displacements in response to x and y forces a clear trend is not apparent (Fig. 4.8 E). From figure 2.7, we would expect that nodes on the right and left side to be

positive and nodes above and below the center to be more negative. The lack of this behavior may be due to a combination of how the z dimension plays a roll in this system and the fact that we have very few data points due to only have data at the nodes of the network rather than at every pixel along the fiber. The presence of variability and noise in the system is hiding the pattern that was observed experimentally when only one node is probed.

To not focus too much on a single node, the simulation size was increased to 20µm by 20µm by 12µm. All the nodes at least 5µm from the stationary nodes at the edges were probed in the x and y directions (Fig. 4.9 A). The pattern of nodes along the direction of the applied force displacing more can be seen in the accumulated data for all 25 nodes which were probed (Fig. 4.9 B). To mimic the optical sectioning of the confocal microscopy used to detect pixel fluctuations, only beads which are 1µm above or below the target node are plotted in figure 4.9B,C,D. In response to applied forces in the x direction, nodes orientated along the x direction, those to the right and left of the target node, show greater displacement than nodes orientated along the y direction, those to the top and bottom of the target node (Fig. 4.9 B). Comparing the differences between the response to applied forces in the x and y direction show a clear preferences for greater displacement in the nodes along the direction of the applied forces. This was also observed experimentally (Fig. 4.9 C, 2.7 A). The difference between these two displacement show a preference for x to the side and y above and below the node to which force is applied. Displacement of nodes which are parallel or perpendicular for nearby nodes are displayed in figure 4.9 D. This plot is comparable to figure 2.7 C, showing that parts of the network parallel to the applied forces respond to a greater degree than parts of the network perpendicular to the applied force and all respond falls off with distance from the target node. However, the model fails to capture the long range force transmission as mean displacements seems to plateau after only moving 3µm from the target node. There are still nodes which displace much higher than the average up to 6µm away even though the mean is much lower. This shows that the force transmits through specific pathways and only effect a very small number of the total nodes.

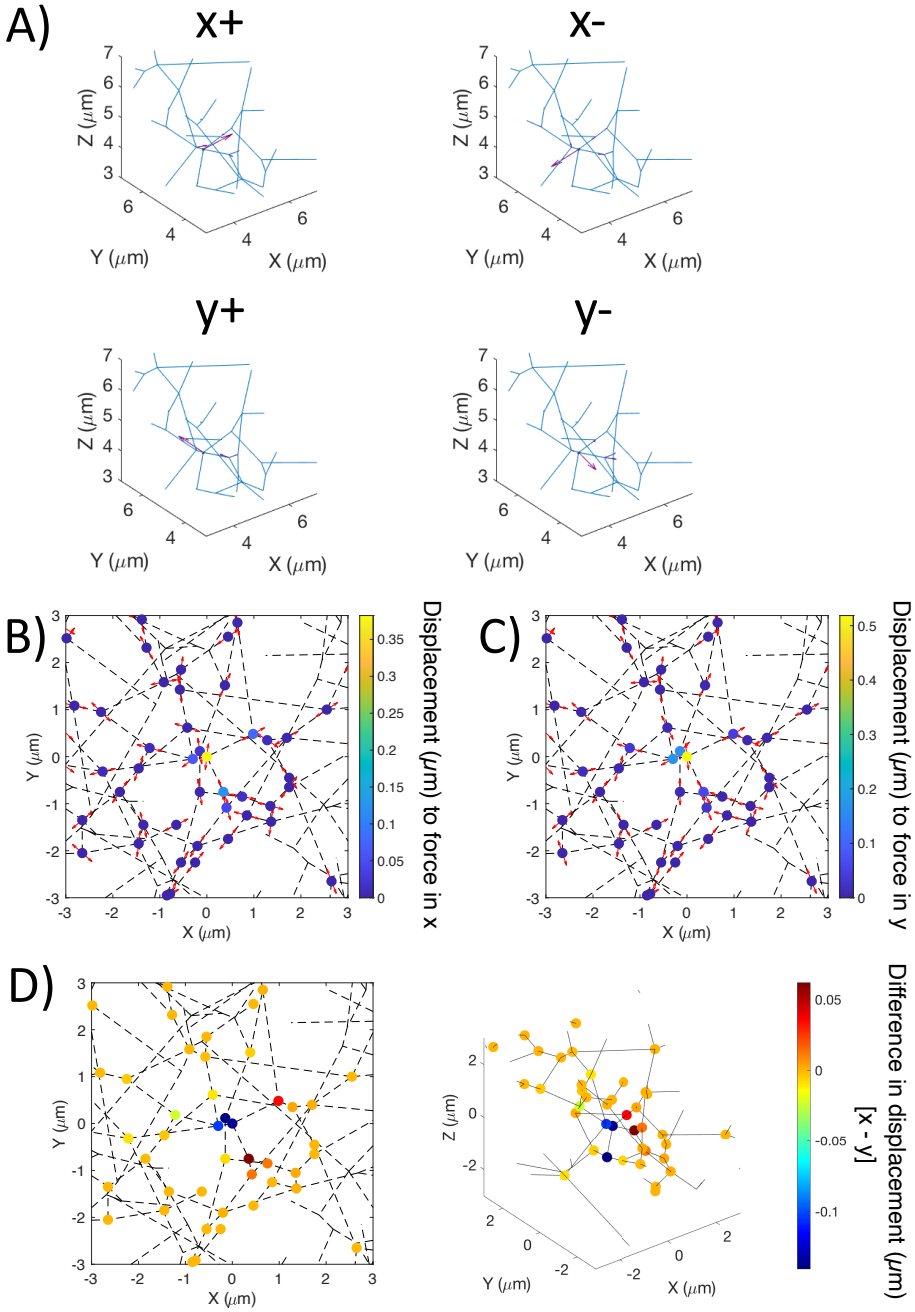

Figure 4.8: Displacement of nearby nodes in small fibrin model in response to applied force along the x and y axes. A) Zoomed in network shown in blue with scaled purple arrows showing node displacement after force applied in x+, x-, y+, and y- directions. B) Displacement of each node in the network in response to x+ and x- forces. Red arrows indicate the direction of node displacements. The fiber network is indicated by dotted black lines. C) Displacement of each node in the network in response to y+ and y- forces. D) The difference between the displacement of the nodes in response to x (B) and y (C) applied forces. The same plot is also shown in 3D. For plots (B), (C), (D) the target node where force is applied is at 0,0,0.

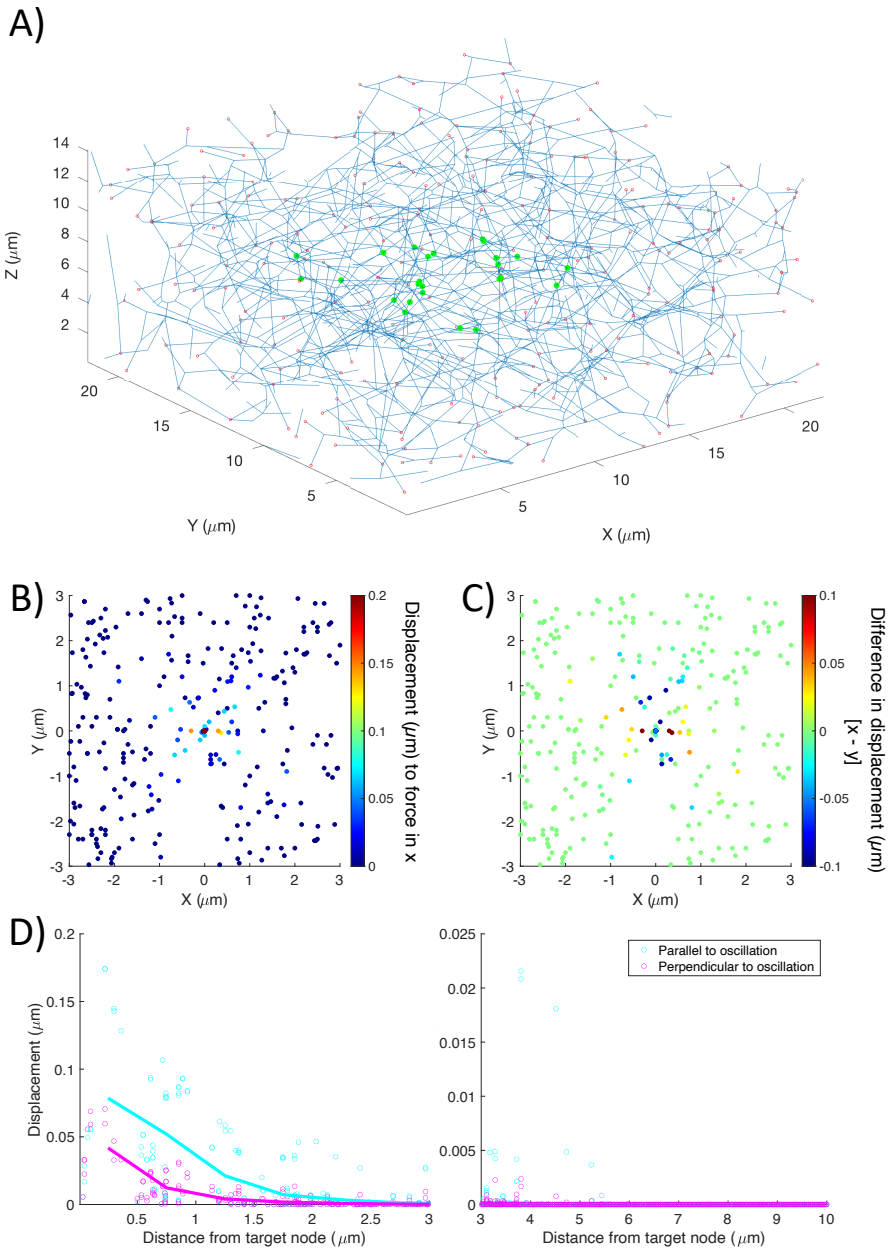

Figure 4.9: Displacement of nearby nodes in large fibrin model in response to applied forces along 6 directions in the x-y plane. A) 200µm by 200µm by 120µm z stack of fibrin hydrogel was used to reconstruct a larger network. 25 nodes in the center were probed in both directions along 0°, 30°, 60°, 90°, 120°, 150° in the x-y plane. B) All data of nearby nodes, centered on the node where force is applied showing the displacement in response to applied forces in the 0° direction. C) All data of nearby nodes, centered on the node where force is applied showing the difference in displacement in response to 0° (x) and 90° (y) applied forces. D) A comparable plot is made to figure 2.7C. displacement of parallel nodes in teal and perpendicular nodes in magenta. Refer to figure 2.7B for diagram explaining which regions are parallel or perpendicular. Left plot goes from 0 to 3 µm while right plot goes from 3 to 10 µm. Y-axis is scaled differently between the right and left plots.

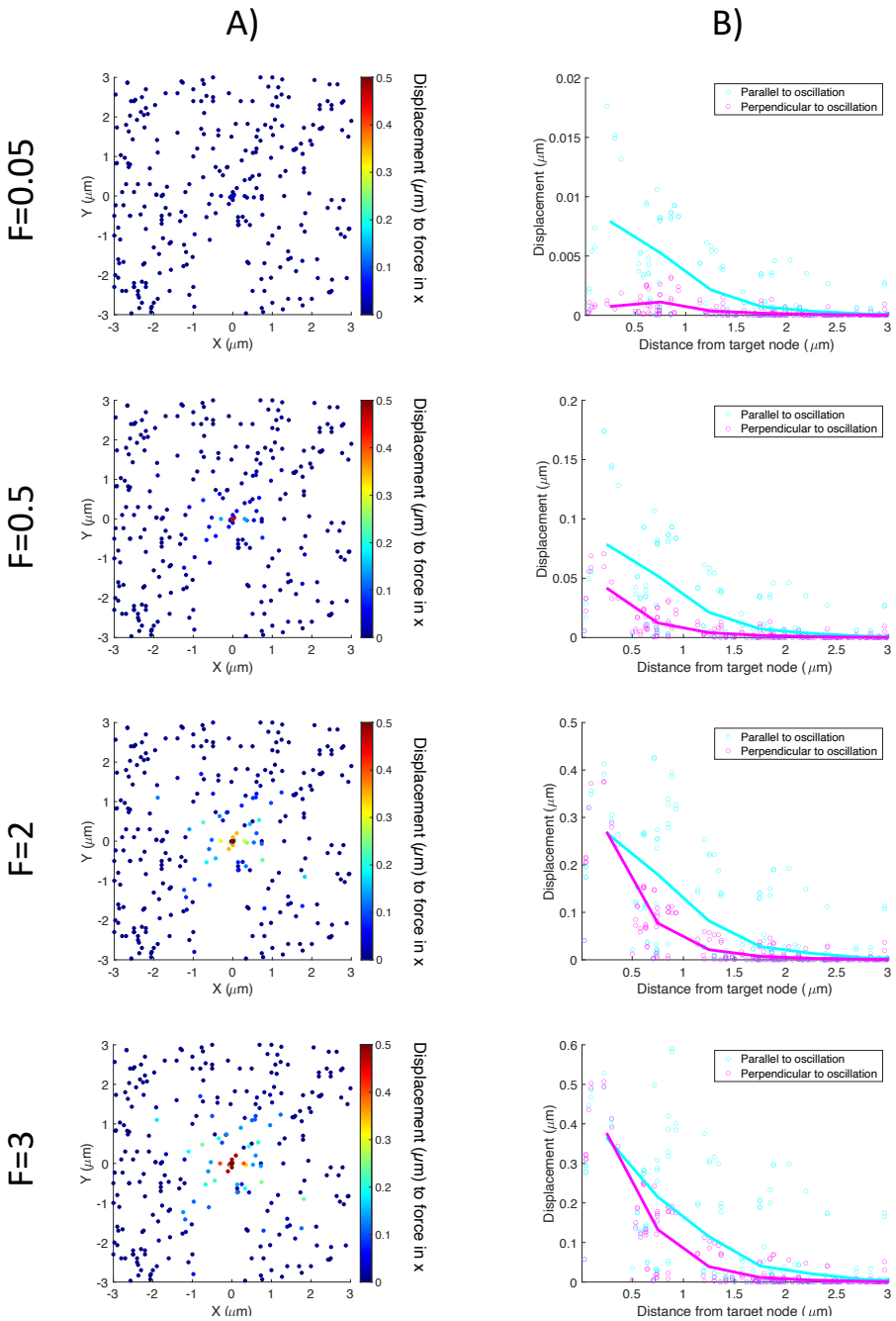

Figure 4.10: Displacement of nearby nodes in fibrin derived model in response to magnitude of applied force. A) Displacement of nodes within the network in response to forces applied in the x direction. These plots are comparable to figure 2.5. B) Average node displacement parallel or perpendicular to the axes of applied force binned by distance. Individual data points are also plotted. These plots are comparable to figure 2.7C.

Similar to experimental observations in figure 2.5, as the applied forces are increased the displacement of the nearby nodes are increased and displacements are observable further away from the target node (Fig. 4.10 A). Interesting, comparison of parallel to perpendicular nodes become more similar to figure 2.7C. The part of the network that is closest to the target node displace equally regardless of whether it is parallel or perpendicular to the applied force (Fig. 4.10 B). Interestingly, regardless of the magnitude of the applied force the mean displacement of nearby nodes goes to 0 by 3µm away.

4.5 Changes to compliance after stretching

To compare this simulation to chapter 3, the fiber networks derived from confocal image stacks are stretched. Starting with the smaller fibrin model first used in figure 4.7, the network is stretched along each of the primary axis. After stretching the network by 50%, the least compliant direction shifted towards to direction that was stretched (Fig. 4.7,4.11). The least compliance direction is visualized as the poles of the ellipsoid in the plots. Increasing stiffness along the stretched direction matches the experimental observations in fibrin after photocrosslinking. However, unlike the simple model in figure 4.3 the shape of the fitted ellipsoid is not drastically change, rather the change is more of a rotation of the ellipsoid. This is most obvious with the stretching along x as the least compliant direction for this node aligned closest to the x axis to begin with.

Looking at the larger 20µm by 20µm by 12µm model from figure 4.8 and limiting the direction of the applied forces to every 30° in the x-y plane we can generate similar plots as in chapter 3 (Fig. 3.8,3.7) [47]. First, a huge amount of variability is observed for node to node and for directions (Fig. 4.12 A). Each node shows variability in compliance depending on the direction of the applied force. The lowest compliance direction (which is the highest stiffness direction) seems to often occur along the direction of the underlying fibers that connect to the

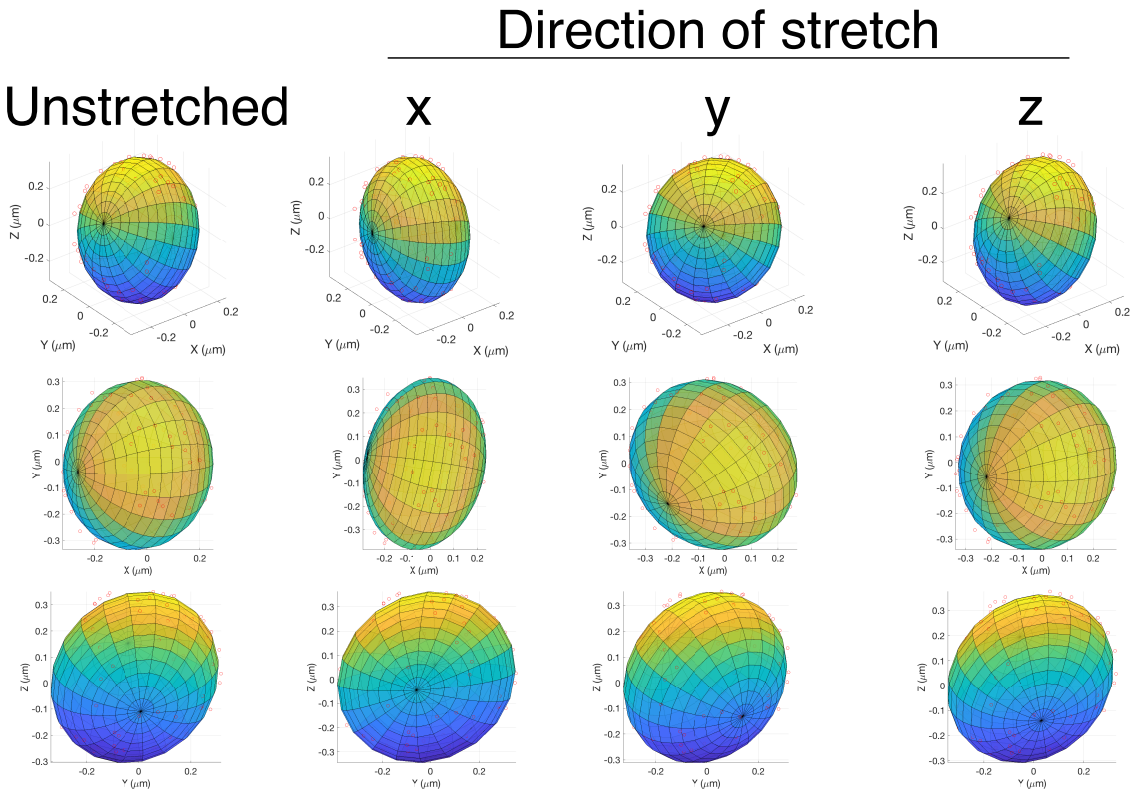

Figure 4.11: The same network and node probed in figure 4.7 is probed in forces (0.5 unit) in all direction after being stretched by 50% along the x , y, or z axis. Ellipsoid fit of displacement response are shown. Red circles indicate displacement data points being fitted to. Columns show the same plot from different angles.

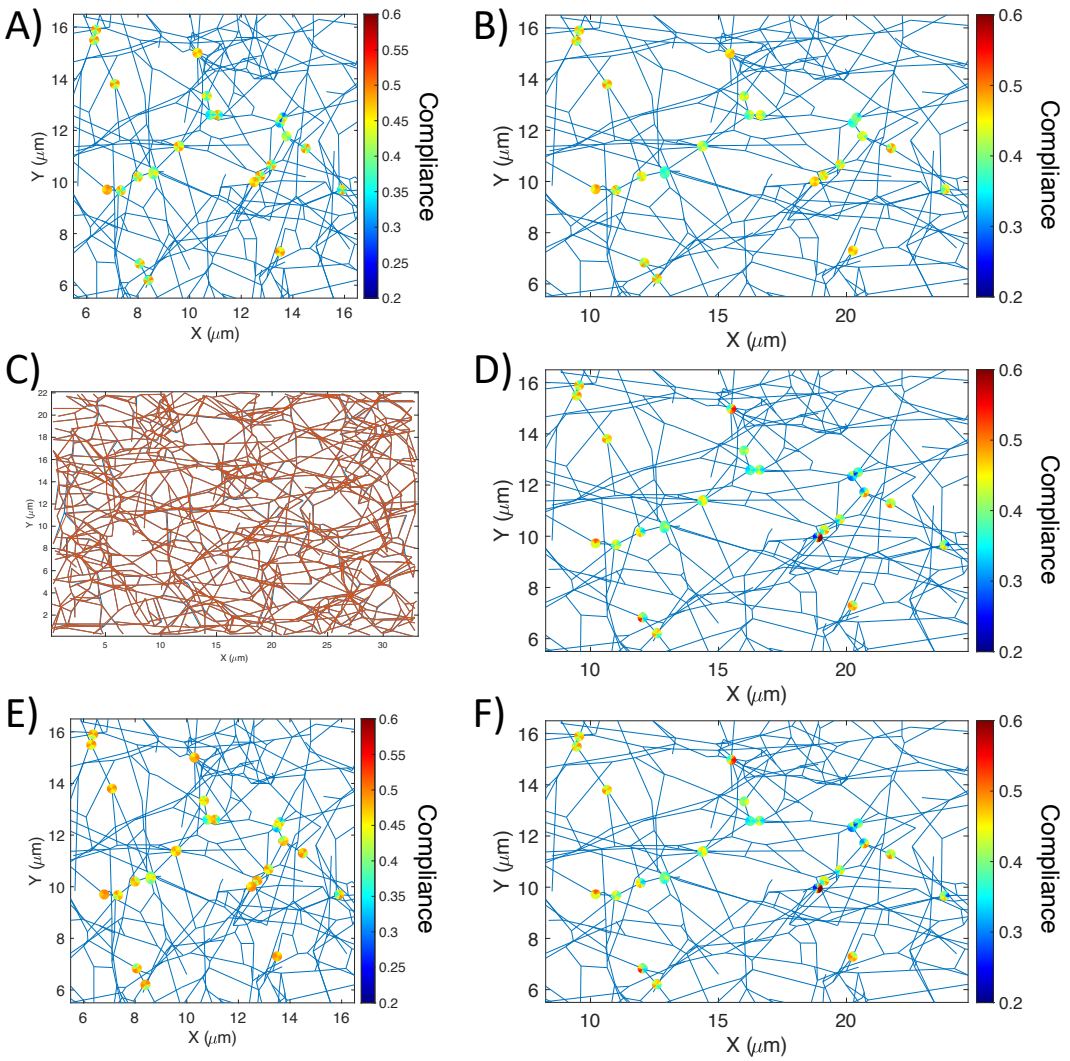

Figure 4.12: Compliance of nodes within large fibrin model in response to 0.5 unit of force in 0°, 30°, 60°, 90°, 120°, 150°, 180°, 210°, 240°, 270°, 300°, and 330° directions. The compliance is plotted for each node with corresponding slice representing the direction of applied force. A) The original large fibrin network. B) The network after 50% affine stretch in the x direction. C) Comparison of the force free state of the affine (blue) stretched and nonaffine (orange) stretched network. D) The network after 50% affine stretch in the x direction. E) The original large fibrin network with fibers that buckle under compression. F) The network after 50% affine stretch in the x direction with fibers that buckle under compression.

nodes. At the scale of each node, the fibers attached to the node are usually not uniformed distributed and creates local fiber alignment. There are also difference between the positive and negative directions when probing. However, there is no statistical difference for any of the simulations showing preference for the positive or negative direction. The node to node variability in compliance is also quite large. This means that differences between comparisons can sometimes only be picked up by paired t-tests rather than unpaired t-tests. The unpaired t-test is still reported here as the experimental observations from AMR in Keating *et al.* and Jagiełło *et al.* were unpaired given the difficultly to ensure paired measurements before and after crosslinking [54, 47].

The network was then stretched in x directions by 50% (Fig. 4.12B,4.13A). The x location of each node was shifted by a corresponding amount to result in affine deformation of the network. Some of the measured compliance increase and some decreased. When comparing each angle of applied force separately before and after stretching, there was no statistical differences by t-test. However, when compared pairwise before and after stretching, compliance decreases along the x (0°) direction and increases in perpendicular direction (90°) (Fig. 4.13B). This matches the observed stiffening that was observed in AMR measurements of fiber being stretched between crosslinked. Also minimum compliance direction does not change as dramatically as observed in figure 3.8. This is potentially due to node variability is higher than beads variability as beads. As observed in chapter 2, beads tend to have much more links attached than a typical fiber to fiber node (Fig. 2.6).

To increase the change in compliance, the network can be further stretched. At a stretch of 100%, the compliance at 90° become statistical difference when compared using unpaired t-test (Fig. 4.13 C). The pairwise differences are more apparently for 0° and 90° but the intermediate angles show inconsistent trends (Fig. 4.13 D). If the network is stretched along 90°, then the effect reverses trend. A increase in compliance is observed for 0° and a decrease for 90° (Fig. 4.13 F). Again, while compliance in the direction and perpendicular to the

stretch is clear, the trend for change in the intermediate angles are not clear.

Up to here the stretch of the fibrin derived networks has been uniformly. The stretch was ensured to be affine by shiften each node uniformly and then reinitializing the length of each fiber so each fiber is not under any strain. Alternatively, we can stretch a network by only manually shifting the stationary edge nodes and letting the free to move nodes equilibriate on their own. This produces a nonaffine deformation of the network as individual fibers will experience different strains (Fig. 4.12 C). For this network, the difference from an affine deformation is quite small but the effect on the compliance is that there is no longer a increase in compliance perpendicular to the stretched direction (Fig. 4.12 D, 4.13 G,H). This more closely represents the experimental observations as we only measured increases in stiffness along the direction of stretching but not a decrease in stiffness in the perpendicular direction (Fig. 3.8).

So far, the properties of the links have been kept linear. We can change the response of the links such that they behave more like ropes than springs. Each fiber now buckle and provide negligible force when under compression. I will refer to this behavior as 'buckling' and the original setup as 'linear'. Comparing linear vs buckling fibers show that compliance is increased in the unstretched state when fibers can buckle (Fig. 4.12 E,4.14 A,B). This makes sense as we are effectively removing some elements within the fiber as they buckle and no longer contribute any force during simulation. When this network is stretched (nonaffine), the compliance in all direction decrease (Fig. 4.12 F,4.14 C,D). This is quite different from the linear affine network or the linear nonaffine network. Interestingly, comparison of the unstretched linear network and stretched buckling network shows that the stretching merely returns the buckling network to a state comparable to the linear network. When a network which is initialized with each fiber element at the edge of buckling will tense most of the fibers when the overall network is stretched (Fig. 4.14 E,F). Moreover, a stretched buckling network, while being statistically different to a stretched linear network, the effect size is small (Fig.

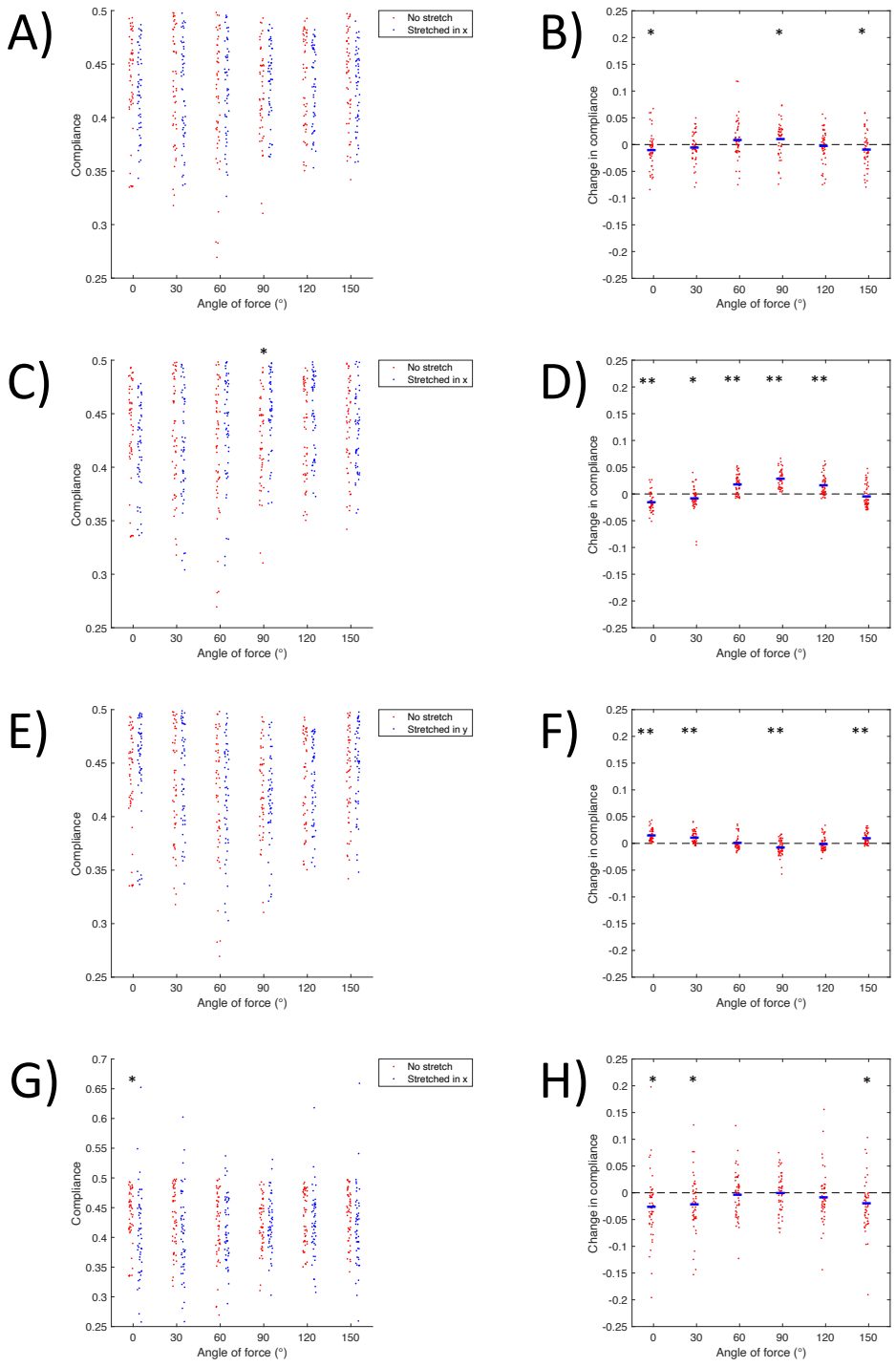

Figure 4.13: Change in compliance within large fibrin model when stretched. Data displayed as compliance before and after stretching or as pairwise difference before and after stretching. A,B) Comparison of compliance of the original network and network after 50% stretch along the x axis. C,D) Comparison of compliance of the original network and network after 100% stretch along the x axis. E,F) Comparison of compliance of the original network and network after 50% stretch along the y axis. G,H) Comparison of compliance of the original network and network after 50% nonaffine stretch along the x axis. Blue bars indicate mean. * indicates $p < 0.05$, ** indicates $p < 0.005$ for unpaired (A,C,E,G) and paired (B,D,F,H) t-test.

4.14 G,H). By changing the properties of the individual fibers to allow for buckling, change in the compliance of the network is observed. However, stretching the network reduced the effect of the buckling.

4.6 Conclusion

Here, I showed that a simple model of linear elastic elements arranged in a network derived from fluorescence image stacks capture some of the behaviours which were experimentally observed. By using the fiber network derived from confocal microscopy of fibrin hydrogels, there is no need to ensure that the arrangement of the generated network has the correct properties such as fiber length, fiber density, and connectivity. However, the trade off is that a region that matches the model size must be imaged. For regions larger than a single field of view of the microscope objective lens, tiling and stitching will be required which can be problematic. Another issue is the amount of time that is required to acquire these images, which is currently not an issue because there are no dynamic elements in these experiments. However, the addition of cells or any other time dependent factors into the system can make image acquisitions at the resolution used in this chapter with laser scanning confocal microscopy unfeasible. The advantage of taking a 3D stack instead of a 2D projected image is that the model generated allows for separation of nodes and fibers in the z direction. 3D networks have more room for fiber rotation and forces can be applied along the z direction.

Analysis of the nearby nodes shows that in this model, force generally travels further in the direction of the applied force compared to the perpendicular direction as observed in chapter 2. Discrete fiber models that allow for rearrangements was expected to capture at least some of the long range force transmission characteristics of biological fibrous ECMs [95, 118, 81]. The addition of strain stiffening fiber elements into this model does not increase this distance. This model has abstracted away the fibers in the network as springs and one or more of the

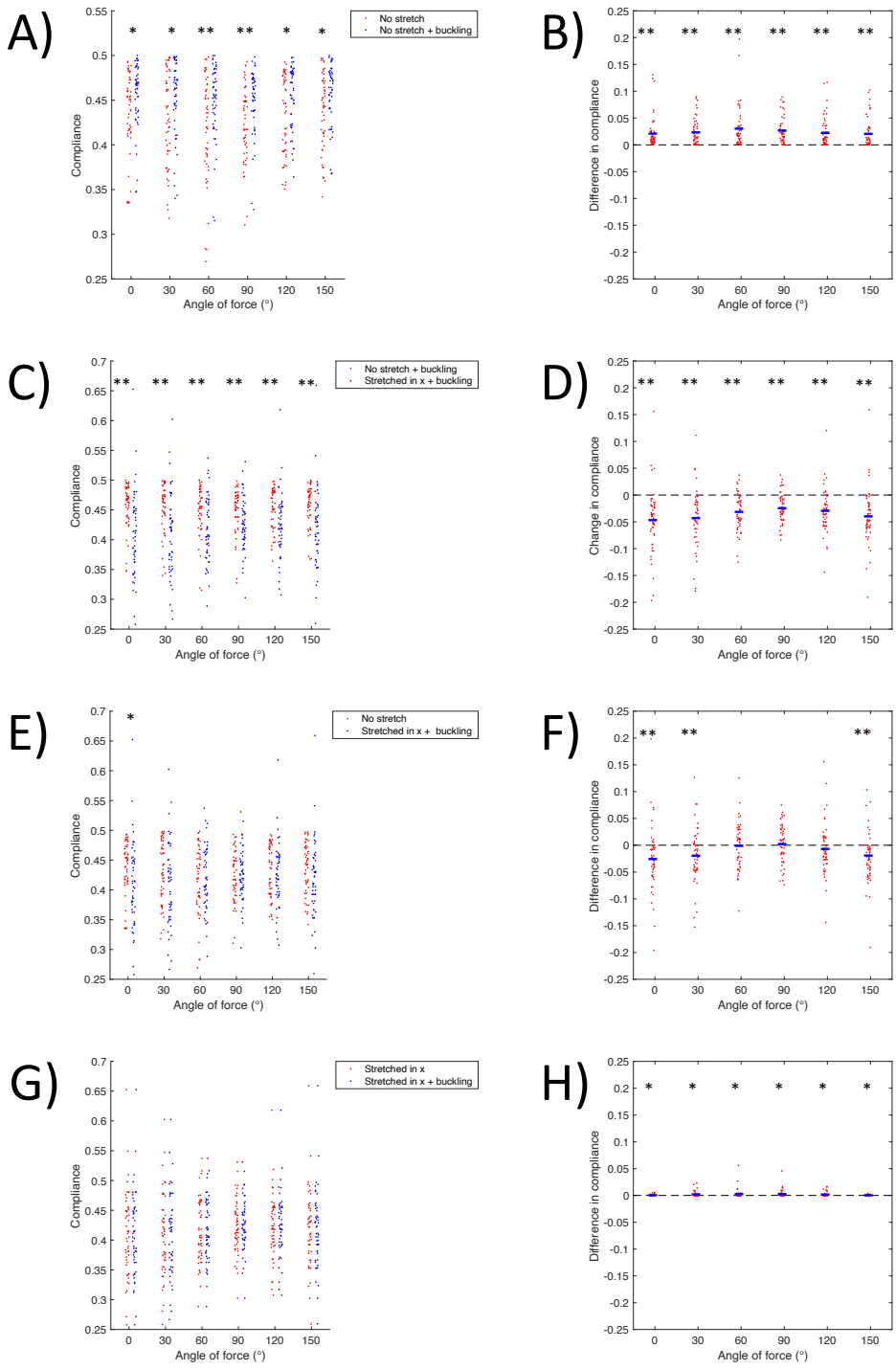

Figure 4.14: Difference in compliance within large fibrin model with fibers that buckle under compression. Data displayed as compliance before and after stretching or as pairwise difference before and after stretching. A,B) Comparison of original network with and without buckling fibers. C,D) Comparison of original with buckling fibers and network after 50% stretch along the x axis with buckling fibers. E,F) Comparison of original and network after 50% stretch along the x axis with buckling fibers. G,H)Comparison of network after 50% stretch along the x axis with and without buckling fibers. Blue bars indicate mean. * indicates $p < 0.05$, ** indicates $p < 0.005$ for unpaired (A,C,E,G) and paired (B,D,F,H) t-test.

factors which has been unaccounted for is responsible for the long range force transmission which is lacking here.

Analysis of the compliance of the nodes to applied forces before and after strain of the network only showed change in stiffness anisotropy was comparable to experimental results from chapter 3 when the network was stretching was nonaffine. However, the amount of strain that is required to produce the experimentally observe anisotropy does not match between model and experiments. Experimentally, the data obtain is not always paired as beads measured before and after deformation may not be the same beads. The change in stiffness measured at beads is greater than the change at the nodes in simulations.

This simple model of a network of springs captures some of the experimentally observed characteristics of fibrin fiber networks. The ability to add in complexity to the model as we choose allows for analyses where we can view the contribution of elements, such as buckling or nonaffine stretching, on the response of the system to applied forces. There is much more to be done both experimentally and computationally to explore the response of fiber networks to applied forces.

4.7 Materials and Methods

4.7.1 Fibrin hydrogel

1.5mg/mL effective concentration of fibrinogen (Sigma, F8630) was dissolved in PBS (Thermo, 14040117) at 37° Celsius for 30 minutes before being sterile filtered (GenClone, 25-244). Thrombin (Sigma,T4648) is added to the fibrinogen at a final concentration of 4U/mL inside MatTek glass bottom dishes (P35G-1.5-14-C). Gels were hydrated with PBS after 30 minutes at 37° Celsius.

4.7.2 Fluorescent microscopy

Fibrin hydrogels were labelled with NHS-ATTO488 dye (Sigma, 41698) at final concentration of 2 µg/mL in PBS and incubated at 37° Celcius for 30 minutes. After washing 3x with PBS, the fibrin was imaged on Olympus Fluoview 3000 laser scanning confocal system with 40x silicone oil objective NA 1.35. The fiber network is imaged using fluorescence confocal microscopy z stack at higher than double optical resolution. Image is then deconvolved using Olympus FV3000 deconvolution software.

4.7.3 Image processing and creating link node model

3D stacks of fluorescently labelled fibrin were used to generate graph and node representation of the fiber networks (Fig. 4.6). Deconvolved 3D stacks were skeletonized and turned into nodes and connection using the skeleton3D and Skel2graph3D tools on Mathworks [62]. Local image brightness was normalized using ImageJ to account for uneven brightness in the sample as well as through the z-stack. The normalized image stack is binarized and then whittled down [36]. Once the image has been skeletonized, nodes can be identified as voxels in the skeletonization which have more than 2 adjacent skeleton voxels. After grouping adjacent node voxels, all the nodes within the network are identified. Links between nodes are then identified by finding the shortest paths between each node. The location of the nodes are stored as well as the connectivity of the network.

4.7.4 Springs simulations

Nodes positions are kept in a list. Connectivity of the nodes are stored in a sparse matrix so that memory requirement for the connectivity matrix grows linear to the number of nodes in the model rather than exponentially. The initial distance between nodes which are connected

are recorded as the initial fiber lengths. After applied forces to a target node, the force each connection between nodes are calculated according to the current distance between. The force determined was a linear function of the difference between current length and initial length but this can be replaced with any arbitrary function. The forces on the nodes are summed and nodes are shifted slightly in the direction of the force applied. This process is iterated until the sum of all forces on each node is close to 0. Further optimization of this process is necessary.

For fiber derived networks, edge nodes are chosen by setting some distance away from the edge of the mode. Nodes within this range are set as stationary edge nodes. The network is trimmed by remove all edge nodes that are not connected to a non-edge nodes and all non-edge nodes which are only connected to one other non-edge nodes. Target nodes are selected as all non-edge nodes within a user selected region, usually the center of the model.

Affine stretching of the network is achieved by shifting each node proportionally along the desired direction. Then the initial lengths of the fibers are redefined as the post-stretched node to node distances. Nonaffine stretching of the network is achieved by shifting each node proportionally along the desired direction. Then nodes were shifted so that forces of the fibers on the nodes were balanced. Note that the initial fiber lengths are kept as the unstretched lengths. This results in a system that is shifted compared to the affine stretched network (Fig. 4.12 C).

Chapter 5

Conclusion

5.1 Summary

Force transmission through fibrous biological materials such as fibrin depend on the structure of the fiber network. Pixel fluctuation analysis shows that the Fourier magnitude and phase of the fluctuation can be used to identify fibers which are elastically coupled to bead being oscillated (Fig. 2.6). Noise in the system, optical, electrical, and mechanical in nature can be mitigated by spatially averaging the Fourier magnitude or taking the OOP of the Fourier phase in a region. Prediction of which apparently disconnected fiber in the confocal image will be elastically coupled is not obvious unless we look at the out-of-plane fibers (Fig. **??**). The direction and amplitude of the bead oscillation in conjunction with the fiber structure determined the oscillation maps that were measured. The fiber structure around individual beads varied greatly between beads and so did the oscillation maps. However, it was often the case that fiber transmitted forces more so in the direction of the fiber (Fig. 2.7). When the fiber and bead oscillation directions matched, fibers further away from the bead in that direction were measured to be oscillating with the bead. Simulation of fiber networks showed

qualitatively similar results with response to oscillation at nodes within the fiber network (Fig. 4.9). Nodes in the direction of the applied force in the simulation were displaced farther than nodes perpendicular to the applied force. In both the fibrin hydrogel and the computational simulations, the specific response of a fiber network at this scale cannot be predicted without knowing the specific fiber network structure being probed.

Modification of the structure of the fiber network using micropatterned photocrosslinking resulted in altered stiffness outside of the crosslinked region. When locally crosslinked, the crosslinked region contracts pulling the noncrosslinked regions nearby towards the crosslinked region. This strain on the nearby fiber network resulted in fiber alignment and stiffness anisotropy. For a circular crosslinked region, fiber displacement was radially inwards (Fig. 3.2 Aviii) and the increase in stiffness was greatest radially and minimally tangentially (Fig. 3.3). For double rectangular crosslinked regions, the fibers between the crosslinked regions are being pulled by both of the crosslinked regions. Stiffness as measured by AMR show increased stiffness and fiber alignment towards the crosslinked regions (Fig. 3.8). Within the crosslinked regions, contraction of the crosslinked region results in larger displacements along the long axis of the rectangular region and thus fiber alignment and stiffness anisotropy favoring the long axis direction. MDA-MB-231 cells showed cell orientation and migration patterns that preferred the direction of fiber alignment and higher stiffness anisotropy (Fig. 3.9). Computation simulation of a fiber network being stretched showed that when nonaffine stretching is applied to the network, compliance of nodes increased in the direction of the stretching (Fig 4.13).

5.2 Outlook

Significant improvements can be made for identifying movement of fibrin fibers within a hydrogel. Ideally displacement of the fibers can be measured directly but much measurements

are difficult when the displacements are small. To improve tracking and avoiding the issue of lack of detection of movement along the fiber, the addition of small fluorescence beads can be an option. For imaging of larger field of view and to avoid the synchronization issue with raster scanning, a camera based system may be preferred. However, some kind of optical sectioning is still required, such as selective plane illumination microscopy [32]. Alternatively, improvements can be made to the laser scanning approach such as customizing the laser scanning path to only along the fiber network or replacing the photodetector with a quadrant photodetector [76]. Such a system can theoretically measure oscillations are much higher frequencies as photodetectors can record measurements at several order of magnitude faster.

Several limitations of ruthenium based crosslinking as it is currently implemented are problematic. Significant exposure of cells to the crosslinker, which is currently necessary to crosslink large regions, temporarily change the morphology and behvior of cells. MDA-MB-231 cells lose their shape and become round when exposed to the crosslinker solutions for hours. These cells also show decreased mobility that doesn't return until 24-48 hours afterwards. Due to the laser scanning approach, the process is also currently very time consuming. To speed up the process, perhaps a photo-mask can be used to control the patterning of the light sacrificing the flexibility of the laser scanning system. If control of micropatterning in 3D is required, then laser scanning with short pulse laser cannot be avoided. With a faster crosslinking process, much larger regions can be crosslinked which would produce larger, and in the case of rectangles more uniform, strains.

Experimental data is required for more complex modelling, especially fiber displacement tracking. While tracking over all fiber region movements was reasonably straight forward, tracking individual fibers , especially in 3D is difficult. One fluorescent fiber looks very much like any another. Structures within the network can also change significantly when strained such that approaches like digital image correlation can produce undesirable results. There is a trade off between how many intermediary snap shots that are taken during the deformation

process and how long the experiment with take. This is especially true for ruthenium based photocrosslinker as the crosslinker must be washed out each time for imaging. In systems where photobleaching is not an issue, addition of sparse fluorescent beads might be the solution to this issue as well. Perhaps even multiple types of fluorescent beads within a single gel can help seed the displacement mapping, or at worst track displacement of the beads.

Transforming confocal image stacks into network models is complicated by non-fiber elements inside the hydrogel. The Skeleton3D and Skel2Graph currently does not account for beads, cells, and fibrin clumps within the hydrogel. Additionally, there is information during the skeletonization process regarding how curved fibers are. But tracing fibers accurately is a difficult task even when done manually [113]. It is difficult to do implement and validate a new process. The fiber structure near beads seem to be atypical as beads acts as nodes which have more than the typical connectivity. The importance of accounting for rotation at the nodes. adding in rotation, and other parameters to the model so the fiber fluctuation results match. Combining pixel fluctuations and crosslinking can be an interesting experiment. We can further validate the model and answer question regarding force transmission by looking at how fibers fluctuate in response to active bead oscillation before and after nearby crosslinking.

This work has offered some insights into the mechanical response of fibrin hydrogels to applied forces by developing novel techniques for observation of fiber network response and altering stiffness and stiffness anisotropy at the micron scale. These findings provides the basis for future improvements to continue the investigation of force response in fibrin hydrogels.

Bibliography

[1] A. Abhilash, B. M. Baker, B. Trappmann, C. S. Chen, and V. B. Shenoy. Remodeling of fibrous extracellular matrices by contractile cells: predictions from discrete fiber network simulations. *Biophysical Journal*, 107(8):1829–1840, 2014.

[2] F. Alisafaei, X. Chen, T. Leahy, P. A. Janmey, and V. B. Shenoy. Long-range mechanical signaling in biological systems. *Soft Matter*, 17(2):241–253, 2021.

[3] A. Ansardamavandi, M. Tafazzoli-Shadpour, and M. A. Shokrgozar. Behavioral remodeling of normal and cancerous epithelial cell lines with differing invasion potential induced by substrate elastic modulus. *Cell adhesion & migration*, 12(5):472–488, 2018.

[4] J. Arulmoli, M. M. Pathak, L. P. McDonnell, J. L. Nourse, F. Tombola, J. C. Earthman, and L. A. Flanagan. Static stretch affects neural stem cell differentiation in an extracellular matrix-dependent manner. *Scientific reports*, 5(1):1–8, 2015.

[5] R. D. Averett, B. Menn, E. H. Lee, C. C. Helms, T. Barker, and M. Guthold. A modular fibrinogen model that captures the stress-strain behavior of fibrin fibers. *Biophysical journal*, 103(7):1537–1544, 2012.

[6] B. L. Bangasser, G. A. Shamsan, C. E. Chan, K. N. Opoku, E. Tüzel, B. W. Schlichtmann, J. A. Kasim, B. J. Fuller, B. R. McCullough, S. S. Rosenfeld, et al. Shifting the optimal stiffness for cell migration. *Nature communications*, 8(1):1–10, 2017.

[7] S. S. Beauchemin and J. L. Barron. The computation of optical flow. *ACM Computing Surveys (CSUR)*, 27(3):433–466, 1995.

[8] H. Birkedal-Hansen. Proteolytic remodeling of extracellular matrix. *Current opinion in cell biology*, 7(5):728–735, 1995.

[9] J. W. Bjork, S. L. Johnson, and R. T. Tranquillo. Ruthenium-catalyzed photo cross-linking of fibrin-based engineered tissue. *Biomaterials*, 32(10):2479–2488, 2011.

[10] F. Bordeleau, B. N. Mason, E. M. Lollis, M. Mazzola, M. R. Zanotelli, S. Somasegar, J. P. Califano, C. Montague, D. J. LaValley, J. Huynh, et al. Matrix stiffening promotes a tumor vasculature phenotype. *Proceedings of the National Academy of Sciences*, 114(3):492–497, 2017.

[11] A. Bouchnita and V. Volpert. A multiscale model of platelet-fibrin thrombus growth in the flow. *Computers & Fluids*, 184:10–20, 2019.

[12] R. Brau, J. Ferrer, H. Lee, C. Castro, B. Tam, P. Tarsa, P. Matsudaira, M. Boyce, R. Kamm, and M. Lang. Passive and active microrheology with optical tweezers. *Journal of Optics A: Pure and Applied Optics*, 9(8):S103, 2007.

[13] B. Burkel, M. Proestaki, P. Grimmer, and J. Notbohm. Mechanical response of fibrous materials to local contractile loads. *Biophysical Journal*, 114(3):365a, 2018.

[14] A. Buxboim, K. Rajagopal, B. Andre'EX, and D. E. Discher. How deeply cells feel: methods for thin gels. *Journal of Physics: Condensed Matter*, 22(19):194116, 2010.

[15] S. R. Caliari and J. A. Burdick. A practical guide to hydrogels for cell culture. *Nature Methods*, 13(5):405–414, 2016.

[16] S. R. Caliari, S. L. Vega, M. Kwon, E. M. Soulas, and J. A. Burdick. Dimensionality and spreading influence msc yap/taz signaling in hydrogel environments. *Biomaterials*, 103:314–323, 2016.

[17] X. Cao. *Continuum Modeling of Cell-extracellular Environment Interaction*. PhD thesis, University of Pennsylvania, 2019.

[18] P. Chaikin and T. Lubensky. Principles of condensed matter physics cambridge univ. *Press, Cambridge*, 1995.

[19] C.-Y. Chang and C.-C. Lin. Hydrogel models with stiffness gradients for interrogating pancreatic cancer cell fate. *Bioengineering*, 8(3):37, 2021.

[20] V. Charulatha and A. Rajaram. Influence of different crosslinking treatments on the physical properties of collagen membranes. *Biomaterials*, 24(5):759–767, 2003.

[21] J. G. Chen, A. Davis, N. Wadhwa, F. Durand, W. T. Freeman, and O. Büyüköztürk. Video camera–based vibration measurement for civil infrastructure applications. *Journal of Infrastructure Systems*, 23(3):B4016013, 2017.

[22] R. A. Clark. Fibrin and wound healing. *Annals of the New York Academy of Sciences*, 936(1):355–367, 2001.

[23] J.-P. Collet, H. Shuman, R. E. Ledger, S. Lee, and J. W. Weisel. The elasticity of an individual fibrin fiber in a clot. *Proceedings of the National Academy of Sciences*, 102(26):9133–9137, 2005.

[24] R. B. Colvin and H. F. Dvorak. Fibrinogen/fibrin on the surface of macrophages: detection, distribution, binding requirements, and possible role in macrophage adherence phenomena. *The Journal of experimental medicine*, 142(6):1377–1390, 1975.

[25] K. G. Cornwell and G. D. Pins. Discrete crosslinked fibrin microthread scaffolds for tissue regeneration. *Journal of biomedical materials research Part A*, 82(1):104–112, 2007.

[26] P. de la Puente and D. Ludeña. Cell culture in autologous fibrin scaffolds for applications in tissue engineering. *Experimental Cell Research*, 322(1):1–11, 2014.

[27] B. J. DuChez, A. D. Doyle, E. K. Dimitriadis, and K. M. Yamada. Durotaxis by human cancer cells. *Biophysical journal*, 116(4):670–683, 2019.

[28] R. Edmondson, J. J. Broglie, A. F. Adcock, and L. Yang. Three-dimensional cell culture systems and their applications in drug discovery and cell-based biosensors. *Assay and drug development technologies*, 12(4):207–218, 2014.

[29] A. J. Engler, S. Sen, H. L. Sweeney, and D. E. Discher. Matrix elasticity directs stem cell lineage specification. *Cell*, 126(4):677–689, 2006.

[30] D. A. Fancy and T. Kodadek. Chemistry for the analysis of protein–protein interactions: rapid and efficient cross-linking triggered by long wavelength light. *Proceedings of the National Academy of Sciences*, 96(11):6020–6024, 1999.

[31] G. Farnebäck. Two-frame motion estimation based on polynomial expansion. In *Scandinavian conference on Image analysis*, pages 363–370. Springer, 2003.

[32] Y. Gong, Y. Tian, and C. Baker. A fully water coupled oblique light-sheet microscope. *Scientific Reports*, 12(1):1–11, 2022.

[33] E. C. González-Díaz and S. Varghese. Hydrogels as extracellular matrix analogs. *Gels*, 2(3):20, 2016.

[34] M. J. Grill, J. Kernes, V. M. Slepukhin, W. A. Wall, and A. J. Levine. Directed force propagation in semiflexible networks. *Soft Matter*, 17(45):10223–10241, 2021.

[35] A. Grosberg, P.-L. Kuo, C.-L. Guo, N. A. Geisse, M.-A. Bray, W. J. Adams, S. P. Sheehy, and K. K. Parker. Self-organization of muscle cell structure and function. *PLoS Computational Biology*, 7(2):e1001088, 2011.

[36] E.-Y. Guo, N. Chawla, T. Jing, S. Torquato, and Y. Jiao. Accurate modeling and reconstruction of three-dimensional percolating filamentary microstructures from two-dimensional micrographs via dilation-erosion method. *Materials Characterization*, 89:33–42, 2014.

[37] Y. L. Han, P. Ronceray, G. Xu, A. Malandrino, R. D. Kamm, M. Lenz, C. P. Broedersz, and M. Guo. Cell contraction induces long-ranged stress stiffening in the extracellular matrix. *Proceedings of the National Academy of Sciences*, 115(16):4075–4080, 2018.

[38] D. Hanahan. Hallmarks of cancer: New dimensions. *Cancer Discovery*, 12(1):31–46, 2022.

[39] D. Head, A. Levine, and F. MacKintosh. Mechanical response of semiflexible networks to localized perturbations. *Physical Review E*, 72(6):061914, 2005.

[40] B. K. Horn and B. G. Schunck. Determining optical flow. In *Techniques and Applications of Image Understanding*, volume 281, pages 319–331. International Society for Optics and Photonics, 1981.

[41] Q. Hu, T. A. Morris, A. Grosberg, A. J. Levine, and E. L. Botvinick. Actively driven fluctuations in a fibrin network. *Frontiers in Physics*, page 653, 2021.

[42] N. E. Hudson, J. R. Houser, E. T. O'Brien III, R. M. Taylor II, R. Superfine, S. T. Lord, and M. R. Falvo. Stiffening of individual fibrin fibers equitably distributes strain and strengthens networks. *Biophysical Journal*, 98(8):1632–1640, 2010.

[43] N. Huebsch, P. R. Arany, A. S. Mao, D. Shvartsman, O. A. Ali, S. A. Bencherif, J. Rivera-Feliciano, and D. J. Mooney. Harnessing traction-mediated manipulation of the cell/matrix interface to control stem-cell fate. *Nature materials*, 9(6):518–526, 2010.

[44] J. D. Humphrey, E. R. Dufresne, and M. A. Schwartz. Mechanotransduction and extracellular matrix homeostasis. *Nature reviews Molecular cell biology*, 15(12):802–812, 2014.

[45] A. Isomursu, K.-Y. Park, J. Hou, B. Cheng, G. Shamsan, B. Fuller, J. Kasim, M. M. Mahmoodi, T. J. Lu, G. M. Genin, et al. Negative durotaxis: cell movement toward softer environments. *BioRxiv*, 2020.

[46] A. Jagiełło, U. Castillo, and E. Botvinick. Stiffness-matched extracellular matrices comprising collagen or fibrin differentially affect cell-mediated remodeling and pericellular stiffness. *Under review*, 2022.

[47] A. Jagiełło, Q. Hu, U. Castillo, and E. Botvinick. Patterned photocrosslinking to establish stiffness anisotropies in fibrous 3d hydrogels. *Acta biomaterialia*, 141:39–47, 2022.

[48] A. Jagiełło, M. Lim, and E. Botvinick. Dermal fibroblasts and triple-negative mammary epithelial cancer cells differentially stiffen their local matrix. *APL bioengineering*, 4(4):046105, 2020.

[49] P. A. Janmey, D. Fletcher, and C. A. Reinhart-King. Stiffness sensing in cells and tissues. *Physiological reviews*, 2019.

[50] P. A. Janmey, J. P. Winer, M. E. Murray, and Q. Wen. The hard life of soft cells. *Cell Motility and the Cytoskeleton*, 66(8):597–605, 2009.

[51] K. A. Jansen, R. G. Bacabac, I. K. Piechocka, and G. H. Koenderink. Cells actively stiffen fibrin networks by generating contractile stress. *Biophysical journal*, 105(10):2240–2251, 2013.

[52] B. A. Juliar, M. T. Keating, Y. P. Kong, E. L. Botvinick, and A. J. Putnam. Sprouting angiogenesis induces significant mechanical heterogeneities and ecm stiffening across length scales in fibrin hydrogels. *Biomaterials*, 162:99–108, 2018.

[53] M. Keating, A. Kurup, M. Alvarez-Elizondo, A. Levine, and E. Botvinick. Spatial distributions of pericellular stiffness in natural extracellular matrices are dependent on cell-mediated proteolysis and contractility. *Acta Biomaterialia*, 57:304–312, 2017.

[54] M. Keating, M. Lim, Q. Hu, and E. Botvinick. Selective stiffening of fibrin hydrogels with micron resolution via photocrosslinking. *Acta Biomaterialia*, 87:88–96, 2019.

[55] J. Kim, Y. Cao, C. Eddy, Y. Deng, H. Levine, W.-J. Rappel, and B. Sun. The mechanics and dynamics of cancer cells sensing noisy 3d contact guidance. *Proceedings of the National Academy of Sciences*, 118(10), 2021.

[56] J. Kim, J. Feng, C. A. Jones, X. Mao, L. M. Sander, H. Levine, and B. Sun. Stress-induced plasticity of dynamic collagen networks. *Nature Communications*, 8(1):1–7, 2017.

[57] O. V. Kim, R. I. Litvinov, J. W. Weisel, and M. S. Alber. Structural basis for the nonlinear mechanics of fibrin networks under compression. *Biomaterials*, 35(25):6739–6749, 2014.

[58] E. Kniazeva and A. J. Putnam. Endothelial cell traction and ecm density influence both capillary morphogenesis and maintenance in 3-d. *American Journal of Physiology-Cell Physiology*, 297(1):C179–C187, 2009.

[59] D. E. Knuth. *Art of computer programming, volume 2: Seminumerical algorithms, 3rd ed.* Addison-Wesley Professional, 2014.

[60] T. M. Koch, S. Münster, N. Bonakdar, J. P. Butler, and B. Fabry. 3d traction forces in cancer cell invasion. *PloS one*, 7(3):e33476, 2012.

[61] K. Kolehmainen and S. M. Willerth. Preparation of 3d fibrin scaffolds for stem cell culture applications. *JoVE (Journal of Visualized Experiments)*, (61):e3641, 2012.

[62] P. Kollmannsberger, M. Kerschnitzki, F. Repp, W. Wagermaier, R. Weinkamer, and P. Fratzl. The small world of osteocytes: connectomics of the lacuno-canalicular network in bone. *New Journal of Physics*, 19(7):073019, 2017.

[63] T. Korff and H. G. Augustin. Tensional forces in fibrillar extracellular matrices control directional capillary sprouting. *Journal of Cell Science*, 112(19):3249–3258, 1999.

[64] M. A. Kotlarchyk, S. G. Shreim, M. B. Alvarez-Elizondo, L. C. Estrada, R. Singh, L. Valdevit, E. Kniazeva, E. Gratton, A. J. Putnam, and E. L. Botvinick. Concentration independent modulation of local micromechanics in a fibrin gel. *PloS One*, 6(5), 2011.

[65] S. Kumar and V. M. Weaver. Mechanics, malignancy, and metastasis: the force journey of a tumor cell. *Cancer and Metastasis Reviews*, 28(1):113–127, 2009.

[66] N. Kurniawan, J. Grimbergen, J. Koopman, and G. Koenderink. Factor xiii stiffens fibrin clots by causing fiber compaction. *Journal of Thrombosis and Haemostasis*, 12(10):1687–1696, 2014.

[67] A. Kurup, S. Ravindranath, T. Tran, M. Keating, P. Gascard, L. Valdevit, T. D. Tlsty, and E. L. Botvinick. Novel insights from 3d models: the pivotal role of physical symmetry in epithelial organization. *Scientific Reports*, 5:15153, 2015.

[68] M. Larsen, V. V. Artym, J. A. Green, and K. M. Yamada. The matrix reorganized: extracellular matrix remodeling and integrin signaling. *Current opinion in cell biology*, 18(5):463–471, 2006.

[69] A. Lesman, J. Notbohm, D. A. Tirrell, and G. Ravichandran. Contractile forces regulate cell division in three-dimensional environments. *Journal of Cell Biology*, 205(2):155–162, 2014.

[70] N. Y. Leung and C. Montell. Unconventional roles of opsins. *Annual review of cell and developmental biology*, 33:241–264, 2017.

[71] A. J. Levine and T. Lubensky. One-and two-particle microrheology. *Physical Review Letters*, 85(8):1774, 2000.

[72] L. Liang, C. Jones, S. Chen, B. Sun, and Y. Jiao. Heterogeneous force network in 3d cellularized collagen networks. *Physical Biology*, 13(6):066001, 2016.

[73] S.-M. Lien, L.-Y. Ko, and T.-J. Huang. Effect of pore size on ecm secretion and cell growth in gelatin scaffold for articular cartilage tissue engineering. *Acta biomaterialia*, 5(2):670–679, 2009.

[74] B. B. Lim, E. H. Lee, M. Sotomayor, and K. Schulten. Molecular basis of fibrin clot elasticity. *Structure*, 16(3):449–459, 2008.

[75] C.-G. Lim, J. Jang, and C. Kim. Cellular machinery for sensing mechanical force. *BMB reports*, 51(12):623, 2018.

[76] E. N. Lissek, T. F. Bartsch, and E.-L. Florin. Resolving filament level mechanics in collagen networks using activity microscopy. *bioRxiv*, page 382903, 2018.

[77] R. I. Litvinov and J. W. Weisel. Fibrin mechanical properties and their structural origins. *Matrix Biology*, 60:110–123, 2017.

[78] J. Liu, Y. Tan, H. Zhang, Y. Zhang, P. Xu, J. Chen, Y.-C. Poh, K. Tang, N. Wang, and B. Huang. Soft fibrin gels promote selection and growth of tumorigenic cells. *Nature Materials*, 11(8):734–741, 2012.

[79] W. Liu, C. Carlisle, E. Sparks, and M. Guthold. The mechanical properties of single fibrin fibers. *Journal of Thrombosis and Haemostasis*, 8(5):1030–1036, 2010.

[80] P. Lu, K. Takai, V. M. Weaver, and Z. Werb. Extracellular matrix degradation and remodeling in development and disease. *Cold Spring Harbor perspectives in biology*, 3(12):a005058, 2011.

[81] X. Ma, M. E. Schickel, M. D. Stevenson, A. L. Sarang-Sieminski, K. J. Gooch, S. N. Ghadiali, and R. T. Hart. Fibers in the extracellular matrix enable long-range stress transmission between cells. *Biophysical Journal*, 104(7):1410–1418, 2013.

[82] A. Mann, R. S. Sopher, S. Goren, O. Shelah, O. Tchaicheeyan, and A. Lesman. Force chains in cell–cell mechanical communication. *Journal of the Royal Society Interface*, 16(159):20190348, 2019.

[83] X. Mao. Mechanics of disordered fiber networks. In *Gels and Other Soft Amorphous Solids*, pages 199–210. ACS Publications, 2018.

[84] T. Matsumoto, J.-I. Sasaki, E. Alsberg, H. Egusa, H. Yatani, and T. Sohmura. Three-dimensional cell and tissue patterning in a strained fibrin gel system. *PloS one*, 2(11):e1211, 2007.

[85] G. Meier and A. Saupe. Dielectric relaxation in nematic liquid crystals. *Molecular Crystals and Liquid Crystals*, 1(4):515–525, 1966.

[86] M. Mesbah. Gradient-based optical flow: a critical review. In *ISSPA'99. Proceedings of the Fifth International Symposium on Signal Processing and its Applications (IEEE Cat. No. 99EX359)*, volume 1, pages 467–470. IEEE, 1999.

[87] D. Mizuno, C. Tardin, C. F. Schmidt, and F. C. MacKintosh. Nonequilibrium mechanics of active cytoskeletal networks. *Science*, 315(5810):370–373, 2007.

[88] O. Moreno-Arotzena, J. G. Meier, C. Del Amo, and J. M. García-Aznar. Characterization of fibrin and collagen gels for engineering wound healing models. *Materials*, 8(4):1636–1651, 2015.

[89] K. T. Morin and R. T. Tranquillo. In vitro models of angiogenesis and vasculogenesis in fibrin gel. *Experimental Cell Research*, 319(16):2409–2417, 2013.

[90] T. A. Morris, J. Naik, K. S. Fibben, X. Kong, T. Kiyono, K. Yokomori, and A. Grosberg. Striated myocyte structural integrity: Automated analysis of sarcomeric z-discs. *PLoS Computational Biology*, 16(3):e1007676, 2020.

[91] P. M. Morse and H. Feshbach. *Methods of Theoretical Physics, Part 1.* McGraw-Hill Book Campany, Inc, 1954.

[92] M. N. Nakatsu, J. Davis, and C. C. Hughes. Optimized fibrin gel bead assay for the study of angiogenesis. *JoVE (Journal of Visualized Experiments)*, (3):e186, 2007.

[93] S. Natan, Y. Koren, O. Shelah, S. Goren, and A. Lesman. Long-range mechanical coupling of cells in 3d fibrin gels. *Molecular Biology of the Cell*, pages 1474–1485, 2020.

[94] G. Nicodemus, S. Skaalure, and S. Bryant. Gel structure has an impact on pericellular and extracellular matrix deposition, which subsequently alters metabolic activities in chondrocyte-laden peg hydrogels. *Acta biomaterialia*, 7(2):492–504, 2011.

[95] J. Notbohm, A. Lesman, P. Rosakis, D. A. Tirrell, and G. Ravichandran. Microbuckling of fibrin provides a mechanism for cell mechanosensing. *Journal of The Royal Society Interface*, 12(108):20150320, 2015.

[96] J. A. Nuhn, A. M. Perez, and I. C. Schneider. Contact guidance diversity in rotationally aligned collagen matrices. *Acta biomaterialia*, 66:248–257, 2018.

[97] B. Pan, K. Qian, H. Xie, and A. Asundi. Two-dimensional digital image correlation for in-plane displacement and strain measurement: a review. *Measurement science and technology*, 20(6):062001, 2009.

[98] M. J. Paszek, N. Zahir, K. R. Johnson, J. N. Lakins, G. I. Rozenberg, A. Gefen, C. A. Reinhart-King, S. S. Margulies, M. Dembo, D. Boettiger, et al. Tensional homeostasis and the malignant phenotype. *Cancer Cell*, 8(3):241–254, 2005.

[99] J. A. Pedersen and M. A. Swartz. Mechanobiology in the third dimension. *Annals of Biomedical Engineering*, 33(11):1469–1490, 2005.

[100] N. E. Persson, M. A. McBride, M. A. Grover, and E. Reichmanis. Automated analysis of orientational order in images of fibrillar materials. *Chemistry of Materials*, 29(1):3–14, 2017.

[101] Y. Petrov. (2022). ellipsoid fit (https://www.mathworks.com/matlabcentral/fileexchange/24693-ellipsoid-fit), matlab central file exchange. retrieved march 29, 2022.

[102] C. R. Picu. Constitutive models for random fiber network materials: A review of current status and challenges. *Mechanics Research Communications*, 114:103605, 2021.

[103] V. S. Ramachandran and J. J. Beaudoin. *Handbook of analytical techniques in concrete science and technology: principles, techniques and applications*. Elsevier, 2000.

[104] S. Rammensee, M. S. Kang, K. Georgiou, S. Kumar, and D. V. Schaffer. Dynamics of mechanosensitive neural stem cell differentiation. *Stem cells*, 35(2):497–506, 2017.

[105] K. M. Riching, B. L. Cox, M. R. Salick, C. Pehlke, A. S. Riching, S. M. Ponik, B. R. Bass, W. C. Crone, Y. Jiang, A. M. Weaver, et al. 3d collagen alignment limits protrusions to enhance breast cancer cell persistence. *Biophysical journal*, 107(11):2546–2558, 2014.

[106] P. Ronceray, C. P. Broedersz, and M. Lenz. Fiber networks amplify active stress. *Proceedings of the National Academy of Sciences*, 113(11):2827–2832, 2016.

[107] M. S. Rudnicki, H. A. Cirka, M. Aghvami, E. A. Sander, Q. Wen, and K. L. Billiar. Nonlinear strain stiffening is not sufficient to explain how far cells can feel on fibrous protein gels. *Biophysical Journal*, 105(1):11–20, 2013.

[108] J. Schindelin, I. Arganda-Carreras, E. Frise, V. Kaynig, M. Longair, T. Pietzsch, S. Preibisch, C. Rueden, S. Saalfeld, B. Schmid, et al. Fiji: an open-source platform for biological-image analysis. *Nature Methods*, 9(7):676–682, 2012.

[109] B. R. Seo, X. Chen, L. Ling, Y. H. Song, A. A. Shimpi, S. Choi, J. Gonzalez, J. Sapudom, K. Wang, R. C. A. Eguiluz, et al. Collagen microarchitecture mechanically controls myofibroblast differentiation. *Proceedings of the National Academy of Sciences*, 117(21):11387–11398, 2020.

[110] J. W. Shaevitz. A practical guide to optical trapping. *University of Washington*, 138, 2006.

[111] J. V. Shah and P. A. Janmey. Strain hardening of fibrin gels and plasma clots. *Rheologica Acta*, 36(3):262–268, 1997.

[112] Q. Shi, R. P. Ghosh, H. Engelke, C. H. Rycroft, L. Cassereau, J. A. Sethian, V. M. Weaver, and J. T. Liphardt. Rapid disorganization of mechanically interacting systems of mammary acini. *Proceedings of the National Academy of Sciences*, 111(2):658–663, 2014.

[113] V. M. Slepukhin, M. J. Grill, Q. Hu, E. L. Botvinick, W. A. Wall, and A. J. Levine. Topological defects produce kinks in biopolymer filament bundles. *Proceedings of the National Academy of Sciences*, 118(15), 2021.

[114] H. J. Solinski and M. A. Hoon. Cells and circuits for thermosensation in mammals. *Neuroscience letters*, 690:167–170, 2019.

[115] E. Sproul, S. Nandi, and A. Brown. Fibrin biomaterials for tissue regeneration and repair. In *Peptides and proteins as biomaterials for tissue regeneration and repair*, pages 151–173. Elsevier, 2018.

[116] J. Steinwachs, C. Metzner, K. Skodzek, N. Lang, I. Thievessen, C. Mark, S. Münster, K. E. Aifantis, and B. Fabry. Three-dimensional force microscopy of cells in biopolymer networks. *Nature Methods*, 13(2):171–176, 2016.

[117] L. Stephens, L. Milne, and P. Hawkins. Moving towards a better understanding of chemotaxis. *Current Biology*, 18(11):R485–R494, 2008.

[118] C. Storm, J. J. Pastore, F. C. MacKintosh, T. C. Lubensky, and P. A. Janmey. Nonlinear elasticity in biological gels. *Nature*, 435(7039):191–194, 2005.

[119] A. Stracuzzi, B. R. Britt, E. Mazza, and A. E. Ehret. Risky interpretations across the length scales: continuum vs. discrete models for soft tissue mechanobiology. *Biomechanics and Modeling in Mechanobiology*, pages 1–22, 2022.

[120] M. Sun, G. Chi, P. Li, S. Lv, J. Xu, Z. Xu, Y. Xia, Y. Tan, J. Xu, L. Li, et al. Effects of matrix stiffness on the morphology, adhesion, proliferation and osteogenic differentiation of mesenchymal stem cells. *International journal of medical sciences*, 15(3):257, 2018.

[121] Z. H. Syedain, J. Bjork, L. Sando, and R. T. Tranquillo. Controlled compaction with ruthenium-catalyzed photochemical cross-linking of fibrin-based engineered connective tissue. *Biomaterials*, 30(35):6695–6701, 2009.

[122] G. Thrivikraman, A. Jagiełło, V. K. Lai, S. L. Johnson, M. Keating, A. Nelson, B. Schultz, C. M. Wang, A. J. Levine, E. L. Botvinick, et al. Cell contact guidance via sensing anisotropy of network mechanical resistance. *Proceedings of the National Academy of Sciences*, 118(29), 2021.

[123] B. Trappmann, B. M. Baker, W. J. Polacheck, C. K. Choi, J. A. Burdick, and C. S. Chen. Matrix degradability controls multicellularity of 3d cell migration. *Nature communications*, 8(1):1–8, 2017.

[124] A. Umeno, H. Kotani, M. Iwasaka, and S. Ueno. Quantification of adherent cell orientation and morphology under strong magnetic fields. *IEEE Transactions on Magnetics*, 37(4):2909–2911, July 2001.

[125] D. Vader, A. Kabla, D. Weitz, and L. Mahadevan. Strain-induced alignment in collagen gels. *PloS One*, 4(6):e5902, 2009.

[126] H. Wang, A. Abhilash, C. S. Chen, R. G. Wells, and V. B. Shenoy. Long-range force transmission in fibrous matrices enabled by tension-driven alignment of fibers. *Biophysical Journal*, 107(11):2592–2603, 2014.

[127] J. H.-C. Wang and B. P. Thampatty. An introductory review of cell mechanobiology. *Biomechanics and modeling in mechanobiology*, 5(1):1–16, 2006.

[128] J. W. Weisel and R. I. Litvinov. Mechanisms of fibrin polymerization and clinical implications. *Blood, The Journal of the American Society of Hematology*, 121(10):1712–1719, 2013.

[129] J. W. Weisel and R. I. Litvinov. Fibrin formation, structure and properties. In *Fibrous proteins: structures and mechanisms*, pages 405–456. Springer, 2017.

[130] R. G. Wells. The role of matrix stiffness in regulating cell behavior. *Hepatology*, 47(4):1394–1400, 2008.

[131] J. P. Winer, S. Oake, and P. A. Janmey. Non-linear elasticity of extracellular matrices enables contractile cells to communicate local position and orientation. *PloS one*, 4(7):e6382, 2009.

[132] J. Yang and K. Bhattacharya. Augmented lagrangian digital image correlation. *Experimental Mechanics*, 59(2):187–205, 2019.

[133] S. Yesudasan and R. D. Averett. Multiscale network modeling of fibrin fibers and fibrin clots with protofibril binding mechanics. *Polymers*, 12(6):1223, 2020.